Stony Brook University

Translational Symmetry Breaking in Materials: First-principles Wannier Function Study

A Dissertation Presented

by

Chia-Hui Lin

to

The Graduate School

in Partial Fulfillment of the Requirements

for the Degree of

Doctor of Philosophy

in

Physics

Stony Brook University

December 2013

Stony Brook University

The Graduate School

Chia-Hui Lin

We, the dissertation committee for the above candidate for the Doctor of Philosophy degree, hereby recommend acceptance of this dissertation.

Wei Ku - Advisor
Physicist, CMPMSD, Brookhaven National Laboratory

Philip B. Allen - Committee Chair
Professor, Department of Physics and Astronomy

Dominik Schneble
Associate Professor, Department of Physics and Astronomy

Mark S. Hybertsen
Group Leader, CFN, Brookhaven National Laboratory

This dissertation is accepted by the Graduate School

Charles Taber
Dean of the Graduate School

Abstract of the Dissertation

Translational Symmetry Breaking in Materials: First-principles Wannier Function Study

by

Chia-Hui Lin

Doctor of Philosophy

in

Physics

Stony Brook University

2013

The spatial periodicity of the crystal structure dictates the electronic band structure theory as the fundamental paradigm in solid state physics. The original translation in materials is commonly broken with an enlarged unit cell required by spontaneously developed long-range order or multiple competing periodicities. The former happens in the systems undergoing the phase transition to antiferromagnetism, charge/spin density waves or lattice distortion. The latter originates from the intrinsic arrangement of the multiple atom system or the externally introduced impurities. The emergence of the broken symmetry can significantly modify the electronic structure, shift the chemical potential, and change the electric, magnetic or optical response in the experimental measurement.

In this thesis, the impact of the translational symmetry breaking on various materials is investigated by utilizing the first-principles

Wannier functions. We represent the electronic structure by calculating the one-particle spectral function in the reference momentum basis corresponding to a shorter periodicity. In the first case, the lattice distortion in Li metal at high pressures is found to cause the Fermi surface topological change, termed Lifshitz transition. This transition triggers an anomalous enhancement of superconductivity. In the second case, we formulate a theoretical approach to create massless Dirac particles in one-band two-dimensional lattice from the inspiration of understanding Dirac cone formation in graphene. In the last case, we discuss that staggered tetrahedral structures in Fe-based superconductors can imply the orbital-parity selective physics in the quasi-particles and superconducting pairing structures.

To my family.

Contents

List of Figures **ix**

List of Tables **xi**

1 Introduction: Materials Science, Energy Band and Symmetry Breaking **1**

1.1 Materials Science 1
1.2 Crystallinity and Energy Band 4
1.3 Symmetry Breaking and Ordering 6
1.4 Charge Density Wave 8
1.5 Overview of Thesis 10

2 Density Functional Theory and Electronic Structure in Matter **11**

2.1 Density Functional Theory 11
2.1.1 Hohenberg-Kohn Theorems 13
2.1.2 Kohn-Sham Equation 16
2.1.3 Local Density Approximation 19
2.2 Wavefunction in Matter 20
2.2.1 Bloch wavefunction 20
2.2.2 Linearized Augmented Plane Wave Basis 22
2.2.3 Wannier Functions in Solid State Physics 26
2.3 One-particle Spectral Function, Photoemission Spectral Weight and Band Structure Unfolding 29
2.3.1 Many-body Green's Function and Spectral Representation 30
2.3.2 Angle Resolved Photoemission Spectroscopy 33
2.3.3 Band Structure Unfolding with One-particle Spectral Functions 36

3 Case 1: Lifshitz Transition and Superconductivity Enhancement in High Pressure *cI*16 Li 43
3.1 Introduction . . . 44
3.2 Method . . . 46
3.3 Unfolded Fermi Surfaces . . . 49
3.4 Lifshitz Transition and Superconductivity . . . 50
3.5 Conclusion . . . 52

4 Case 2: Dirac Cones in Two-Dimensional Dispersion via Periodic Modulation of On-site Energy 54
4.1 Introduction . . . 54
4.2 Dirac Cone in Graphene . . . 55
4.3 Dirac Cones in Two-dimensional Lattice with Enlarged Unit Cells 60
4.4 Conclusion . . . 61

5 Case 3: One-Fe versus Two-Fe Brillouin Zone of Fe-Based Superconductors 65
5.1 Introduction . . . 65
5.2 Method . . . 67
5.3 Unfolded Band Structure and Fermi Surfaces . . . 68
5.4 Discussion . . . 70
5.5 Vacancies Ordered $K_{0.8}Fe_{1.6}Se_2$ . . . 73
5.6 Conclusion . . . 74

6 Case 4: Orbital-Parity Selective Superconducting Pairing Structures of Fe-based Superconductors under Glide Symmetry 75
6.1 Introduction . . . 75
6.2 Hamiltonian with Glide Symmetry . . . 77
6.3 Local Gauge and Physical Momentum Spaces . . . 78
6.4 Orbital-Parity Selective Quasiparticles . . . 79
6.5 Orbital-Parity Selective Superconducting Pairings . . . 80
6.6 Finite-Momentum Pairing . . . 84
6.7 Conclusion . . . 85

7 Conclusion 86

Bibliography **88**

A Mathematical Formalism of Dirac Cone Generation **98**

B Comparison between Theoretical and Experimental ARPES Spectral Functions **103**

B.1 $Ba(Fe_{0.92}Co_{0.02})_2As_2$ 104

B.2 $Fe_{1.03}Te_{0.74}Se_{0.26}$ 105

C Virtual Crystal Approximation **107**

D List of Acronyms **109**

List of Figures

1.1 Crystal structures of graphite and diamond. 4
1.2 Gas, liquid and solid phases of matter. 6
1.3 Magnetic ordering in the magnet. 7
1.4 Schematic diagrams of charge density wave formation. 8

2.1 Interacting electronic and non-interacting Kohn-Sham systems. 16
2.2 Flow chart of solving Kohn-Sham orbitals in the LAPW basis. 25
2.3 GaAs Band structures from DFT and Wannier functions. . . . 29
2.4 Carbon nanotube band structures from DFT and Wannier functions. 30
2.5 Standard ARPES setup 34
2.6 Band folding in one-dimensional toy model. 37
2.7 Unfolded band structure in one-dimensional charge density wave toy model. 40

3.1 Schematic diagrams of the Lifshitz transition. 44
3.2 Schematic diagrams of the anomalous part in density of states from the Lifshitz transition. 45
3.3 Phase diagram and crystal structures of Li. 46
3.4 Illustration of Fermi surface folding issue. 47
3.5 Fermi surfaces of $cI16$ Li. 48
3.6 Density of states and $\Delta T_c/T_c^{ref}$ versus pressure for $cI16$ Li. . . 51

4.1 Graphene Dirac cones in the eigenstate and unfolded representations. 57
4.2 Band structures and energy isosurfaces of the reference charge density wave system to the graphene. 58
4.3 Dirac cones on a square lattice with $\frac{1}{3}$ affected atoms 62

4.4 Dirac cones on a square lattice with $\frac{1}{4}$ affected atoms. 63

5.1 Illustration of one-Fe and two-Fe unit cells and the corresponding Brillouin zones. 66
5.2 Unfolded band structures and Fermi surfaces of various Fe-based superconductor compounds. 69
5.3 Demonstration the importance of the broken symmetry potential to generate the electron pockets in Fe-based superconductors. 71

6.1 Spectral function in the crystal and pseudo-momentum basis in the one-Fe Brillouin zone. 78
6.2 Schematic diagrams of orbital-parity selective pairing structures in the intra-orbital Cooper pairs. 81
6.3 Orbital-parity selectivity from ARPES and STS data. 83
6.4 Weight of anomalous Green's function on the electron pockets 85

B.1 $Ba(Fe_{0.92}Co_{0.02})_2As_2$ ARPES [1] versus first-principles $BaFe_2As_2$ spectral function 104
B.2 $Fe_{1.03}Te_{0.74}As_{0.26}$ ARPES [2] versus first-principles FeTe spectral function 106
B.3 $Fe_{1.03}Te_{0.74}As_{0.26}$ ARPES [2] versus first-principles FeTe spectral function on the M pockets at different energies 106

List of Tables

2.1 Notation for normal and super cells. 38

5.1 Lattice information of first-principles calculation in Fe-based superconductors. 67

5.2 Hoppings in the Fe 3d Wannier function basis. 72

Chapter 1

Introduction: Materials Science, Energy Band and Symmetry Breaking

This chapter is aimed to give a general review about the basic concepts in materials science from the practical aspect of condensed matter physics. In addition, I will briefly discuss the two main ideas covered in my studies, energy band theory and symmetry breaking associated with ordering in solids. In the end, the overview of this thesis will be given.

1.1 Materials Science

In human history, studies of materials have been a fast-growing topic and are tightly related to the evolution of our civilization. Along with the usage of stone, bronze, and iron, human beings empirically realized the importance of macroscopic physical quantities, like hardness, tensile strength, and density. By naked eye and the traditional optical magnifying glass, people also started to categorize the materials and minerals by their external color, surface reflectivity, and any information from the appearance. In addition, after numerous trials and errors in metallurgy, the ancient professional blacksmiths already learnt to improve the metal properties by techniques like casting, forging, thermal treatment and so on. Before the birth of modern science, human beings had naturally developed the skills to perform materials characterization

and engineering for improving their lives.

In the 19th century, as different subjects of classical physics emerged, materials research became an active branch of science. Physicists and chemists were eager to know what is inside the black box. The direct way is to systematically quantify the interesting responses of the external probes, like heating/cooling, electric current, magnetic field, and so on. Numerous efforts had led to a long list of empirical laws in physics. However, the real breakthrough in materials science was brought about by the birth of quantum mechanics in the twentieth century. After that, scientists became able to understand the materials from the bottom-up philosophy. The mysteries beneath the black box became much clearer than ever. With fast accumulated knowledge, a new era of fabricating and designing new materials began and has been bringing unprecedented success in our history.

One of the most exciting pages in materials science is the triumph of semiconductors. It has been translated to the most influential manufacturing industry and dramatically changed our lives in the past five decades. Scientists magically turned worthless sand (silicon) into chips that are full of integrated circuits and worth thousands of dollars. All these efforts have boosted the so-called *second industrial revolution*. Various high-performance devices, which used to occupy an entire space of a room, are now minimized to fit your pockets. Its wide and far-reaching applications are everywhere from your computer or cell phone in your daily work, automobile electronic system or the navigator in you regular commuting, the liquid crystal display or game consoles in your recreation, etc. The impact from materials science is already beyond our imagination.

In addition to the information technology development, the discoveries of various novel materials are also revolutionizing our world silently. One example is from our ancient wisdom: the magnet used in the compass. It plays an essential role in transformer devices for power transmission, which brings the electricity from the distant power plant to every appliance in your home. Its quality and working efficiency would decisively determine the energy loss in the large-scale facilities. As the energy crisis becomes the most important global issue, the search for quality magnets is still very active. Another example is the superconductor [3], in which the electric current can flow without

loss of energy below certain transition temperature. One practical application is to generate high current flow in the magnetic resonance imaging for medical purpose. There, the generated magnetic field is strong enough to provide high-resolution scans across different human body tissues and detect internal injuries. Hence, quality superconductors are highly demanded to help the correctness and precision of medical diagnoses. Indeed, the innovation in various novel materials is changing our world progressively.

To gain more insight and reveal the mechanisms behind different functionalities, it is also important to test material behavior under various extreme conditions. With the fast development of experimental techniques, people can now put samples in contact of a diamond tip (diamond anvil cell) with applied pressures up to 350 GPa, which is roughly the pressure at the center of the earth [4]. This magnitude is enough to turn charcoal into diamond. Besides, in low-temperature physics, one can cool down samples to temperatures close to absolute zero. In this case, one piece of material can undergo a transition to another phase and exhibit dramatically different characteristics. For example, titanium nitride is a piece of ceramic that is usually applied as a coating on metallic machine tools to prevent corrosion. It does not posses the electric conductivity as good as the regular metal. However, if we cool it down to $\sim$ -267 °C, it becomes a zero-resistivity superconductor, which is superior to most metals in electric conduction. Therefore, exploring the materials properties under different external conditions facilitate the design in new functionalities.

The development of materials science has always been a close combination of practical purpose and pure scientific curiosity. Although there are only few basic building blocks consisting of electronic charges, electronic spins, and the lattice, the interplay between them leads to a tremendous amount of intriguing phenomena. It has become the largest discipline in science and also brought the inter-disciplinary innovation to chemistry, medicine, bio-engineering, electric engineering to name a few. To resolve the emergent energy problem and innovate the architectures in the next-generation technology, comprehensive studies and novel design of the materials are still an unfinished quest.

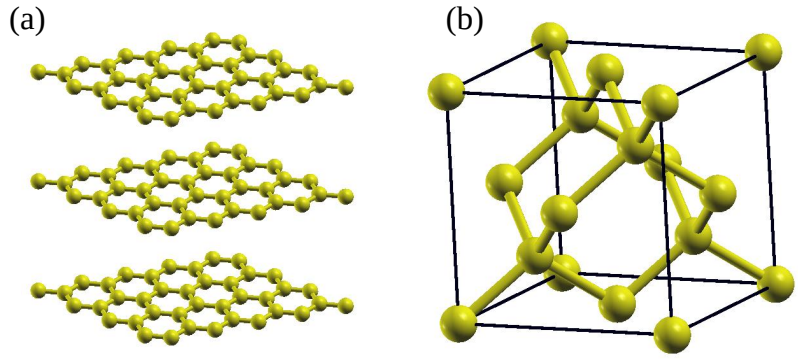

Figure 1.1: Crystal structures of (a) graphite and (b) diamond.

1.2 Crystallinity and Energy Band

Crystallinity is the most fundamental and essential property of solid state materials. In contrast to the freedom of moving around in gaseous and liquid states, atoms are periodically arranged in the solid. Moreover, the types of arrangement in materials have a direct influence on hardness, density, transparency, and so on. For example, the graphite from the tip of your pencil is composed of carbon atoms with hexagonal structure as shown in Fig. 1.1(a). It is known for its opacity, brittleness, and moderate electric conductivity. On the other hand, the precious diamond is also purely composed of carbon atoms (except for a small amount of impurities), but its atoms are arranged differently in a cubic lattice as shown in Fig. 1.1(b). Very different from the graphite, diamond features superior hardness and high refractive index leading to its sparkle scintillation. Also, its transparency and electrically insulating properties are totally opposite to graphite. Even with the same chemical composition, the crystalline structure can still play the defining role for physical and chemical characteristics.

Band structure theory of electrons, a central feature in solid state physics, is dictated by the periodicity of the crystal combined with the quantum nature of the electrons. Different from the classical particles in our daily experience, the electrons in materials are only allowed to occupy the levels in certain energy ranges, which are called energy bands and consists of many electronic states [5, 6]. Also owing to the Paul exclusion principle, one electronic state

cannot accommodate more than one electron. Then, the energy bands can only be fully occupied, partially occupied, and empty. One important implication is that the materials can be categorized into a conductor with partially occupied bands or an insulator with only fully occupied and empty bands. In the conductor, any infinitesimal voltage can produce electric current because only negligible energy is needed to promote the electrons to the mobile states. In the insulator, no available mobile states exist in the the fully occupied energy bands so that the infinitesimal voltage can not generate electronic flow. This is why its electric resistance is enormously large. Only when the applied voltage is high enough to overcome a threshold energy called band gap, the energy difference between the highest occupied band and the lowest empty band, the insulator can become conducting under high voltage. In some cases, if the energy gap roughly is $2 \sim 3$ eV or below, we usually call the material as semiconductor. This is because thermal energy of the room temperature is already enough to overcome the band gap. Then its electric resistivity becomes controllable between conducting and insulating behavior by design.

The band structure is like a detailed user manual about how to utilize this material. Under certain reasonable assumptions, it is possible to know any useful and measurable material properties accurately. For example, optical properties are basically determined by the band structure in the materials used in the light emitting diode (LED). By applying the electric voltage, the GaAsP and InGaN semiconductor devices can emit red and blue light respectively. The colors of the emitted light of different semiconductors are mainly determined by the band gap size. In addition, how fast the electron can move in the materials is also guided by the effective mass and velocity in the band structure. The wide range of applications and success of the band structure picture makes it the most important concept in materials science. It subsequently lays the foundation of the whole semiconductor industry and stimulates numerous studies in sub-disciplines, including mesoscopic physics and nano-technology.

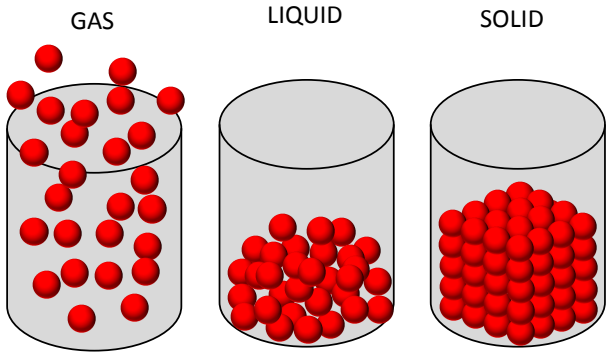

Figure 1.2: Gas, liquid and solid phases of matter.

1.3 Symmetry Breaking and Ordering

Symmetry is of prime importance for any discipline of physics. From constructing the fundamental model, various conservation laws and the selection rules in physical processes, symmetry always dictates the most robust consequences independent of the details of the system. In reality, it is very often that the symmetries in the Hamiltonian are broken in the ground or the stable state at a given temperature. This is the famous symmetry breaking phenomenon shared by all disciplines in physics. In condensed matter, one example concerns the three typical phases in matter: gas, liquid, and solid as illustrated in Fig. 1.2. At extremely high temperature, it is intuitive to think that all atoms in materials would be vaporized and becomes gaseous state. Thus, upon averaging over all the random motions of atoms, the continuous translational and rotational symmetries are preserved in the gaseous status. When temperature is cooled down sufficiently to pass the liquid phase, the atoms in the solid start to be arranged according to certain crystal structure with most stable energy. Then, only discrete lattice translational and discrete rotational symmetries can remain. This exemplifies the process of symmetry breaking from the continuous translation (rotation) to discrete translation (rotation). We usually call this process as ordering.

The other example is the magnet in your compass, and all magnetic materials. If you heat up a piece of magnet on the stove, you will find that the magnetism disappears and it will not be aligned to the poles of the earth.

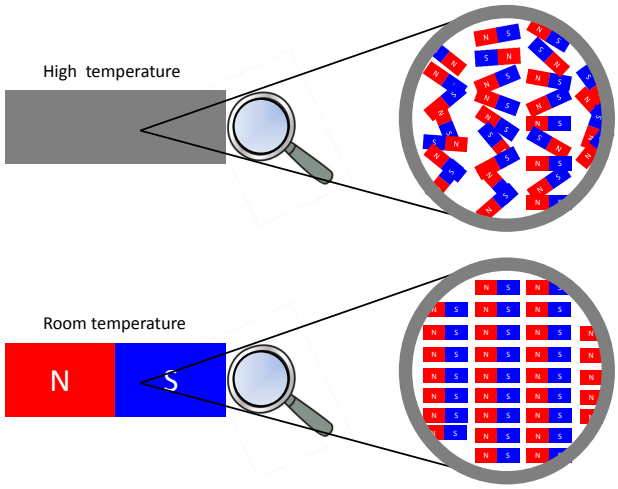

Figure 1.3: Macro- and micro-structures of the magnets at room and high temperatures.

However, if you keep it cooled down for a while, we can find the ferromagnetism is resumed. The microscopic origin is that each atom acts like a tiny magnet inside that piece of magnet as in Fig. 1.3. The high temperature environment would randomize the orientation of each tiny magnet and fulfill the rotational symmetry as in the upper panel of Fig. 1.3. Once the temperature is lowered, the interaction between tiny magnets would prefer the alignment in parallel to reduce the total energy at room temperature as in the lower panel of Fig. 1.3. Therefore, macroscopic magnetism is spontaneously formed at low temperature and breaks rotational symmetry that the magnet used to have at high temperature. In addition, the space inversion symmetry is commonly broken in ferroelectric and antiferroelectric materials. Similarly, global gauge symmetry is broken in superconductivity and superfluidity. From a practical perspective, an ordered phase usually corresponds to the appearance of an intriguing material property. For example, magnetism, superconductivity, and ferroelectricity have been widely used in various applications beyond purely scientific interest. [7] Thus, in order to control and improve functionality, it is desired to understand how the ordering is induced and how it is coupled to the underlying electronic structure.

The main goal of this thesis is to investigate the specific symmetry break-

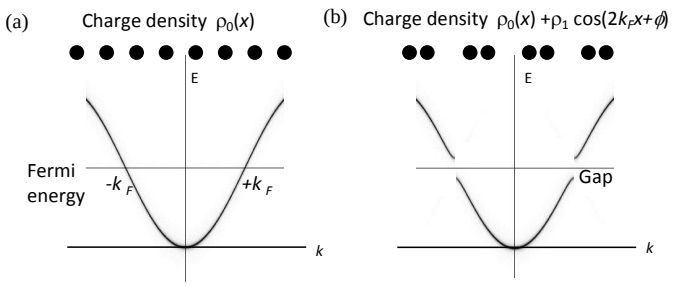

Figure 1.4: Schematic diagrams of charge density wave formation. The one-dimensional metal in (a) reduces its electronic total energy by forming a CDW in (b).

ing in the lattice translational invariance. In general, most of the emergent orderings in materials are associated with this broken translational symmetry, such as antiferromagnetism, charge/spin density waves, and lattice distortion. Based on the two cornerstones, band theory and symmetry breaking, of solid state physics, I will address the physical consequences in several several realistic materials.

1.4 Charge Density Wave

One symbolic long range order is the charge density wave (CDW) phase, which is a periodic modulation of the electronic charge density in general [8]. Peierls initiated the pioneering work to predict an instability in a one-dimensional metal [8]. Because one-dimensional normal metal has a conduction band filled with electrons up to a Fermi wave vector k_F as in Fig. 1.4(a), the gap opening at Fermi energy leads to an energy gain in electronic structure and a new insulating phase as in Fig. 1.4(b). This also introduces the new Brillouin zone boundaries at $\pm k_F$ and a new potential in real space with an periodicity of $\frac{2\pi}{2k_F}$. This spontaneous transition results in atomic distortions and is usually called Peierls transition. In a simple case of a half filled band, $k_F = \pi/2a$, where a is the lattice constant. The developed new period is $2a$. This is a typical case of a commensurate CDW, in which the new periodicity is a rational fraction or multiple of the lattice constant. Otherwise, the charge modulation is called incommensurate.

Another way to reveal the vulnerability of a system is to discuss its charge

response function, namely the bare charge susceptibility:

$$\chi^0(q) \propto \sum_k \frac{f_{k+q} - f_k}{\epsilon_{k+q} - \epsilon_k}, \tag{1.1}$$

where ϵ_k is the eigenenergy at k. Then, f_k is the Fermi-Dirac function at energy ϵ_k. It is clear that the divergence of $\chi^0(q)$ is mainly contributed by the case that $k = -k_F$ and $q = 2k_F$ because k_F and $-k_F$ are degenerate states. In the case of one dimension, the Fermi surface is composed of two k points. Therefore, the divergence plays a defining role in CDW instability. In two dimensions, the importance of Fermi wave vectors is diluted. Only when a dispersion has specific nesting vectors, a two-dimensional system can possibly have tendency toward CDW instability. In three dimensions, the divergence is much less important so a spontaneous development of charge density waves is less likely to happen.

Since CDW is more prominent in low-dimensional physics, early research was mostly about the quasi-one-dimensional organic materials, such as TTF-TCNQ [9]. Due to gap opening on the Fermi energy, this class of materials was experimentally confirmed to undergo a metal-insulator Peierls transitions at low temperature. This was recognized as the first realization of Peierls' prediction. There are more researches about transition metal dichalcogenides [10], which are layered materials and usually contain several nesting vectors on Fermi surfaces. These materials also undergo Peierls transitions and form a qausi-two-dimensional CDW.

In this thesis, we borrow the concept of *charge modulation* from CDW to investigate electronic structure. For example, when a material contains two kinds atoms with different periodicities, the presence of one kind of atoms can be regarded as an external charge modulation of a different periodicity to another. In another case, a material can have intrinsic atomic displacements in its crystal structure. Although this does not directly involve spontaneous symmetry breaking, the CDW concept is perfect to be applicable.

1.5 Overview of Thesis

In addition to the general introduction presented in Chapter 1, the technical background will be reviewed in Chapter 2. We start with density functional theory and the Kohn-Sham equation. The wavefunctions in the materials can be represented as either the Kohn-Sham orbitals in the form of the Bloch wave or its real-space counterpart Wannier functions with richer local physics information. Then, I will recap the electronic structure represented by the Green's function formalism and extend it to the first-principles unfolding method, which is applicable to study the physical effects from the broken translational symmetry.

In the second part, I will present the four main studies on the influence of the translational symmetry breaking in the novel materials. For the first case in Chapter 3, one Fermi surface topological change, termed Lifshitz transition, is identified in the high-pressure phase of Lithium metal and so is its impact on superconductivity enhancement. In this study, we also build the first visualization of the three-dimensional unfolded Fermi surface. In Chapter 4, we provide an alternative viewpoint to understand Dirac cone formation in graphene. This understanding is extended to a simple scenario to theoretically build Dirac cones in a general one-band 2D lattice. In Chapter 5, we calculate the unfolded band structure in Fe-based superconductors, reveal its implications to the magnetic and superconducting correlations, and provide a direct comparison to results from photoemission spectroscopy. In Chapter 6, we show the glide translation (remaining symmetry after the translation is broken) in Fe-based superconductors leads to an exotic orbital-parity selectivity in the quasiparticles and superconducting pairing structures.

Chapter 2

Density Functional Theory and Electronic Structure in Matter

In this chapter, I will start with reviewing the background knowledge of the density functional theory (DFT) [11], which is one of the most successful methods to deal with a quantum mechanical system. Since the many-body problem can be mapped into a non-interacting electron problem by the Kohn-Sham equation, its solution, Kohn-Sham orbitals, can be solved as the Bloch wave of the solids under an effective periodic potential. I would also introduce two useful bases for the electronic wavefunction: the linear augmented plane wave (LAPW) and the Wannier function. The former is numerically reliable and provides excellent computational performance in first-principles packages, for example the implementation in WIEN2k [12]. The latter is the real space counterpart to the Bloch wave and useful in characterizing the chemical bonding with the local physics picture. Moreover, Wannier functions can help compress the numerical information in DFT (involving $\sim 10^3$ LAPW basis) into the low energy Hilbert space composed of ~ 10 local orbitals. Thus, it is made easy to represent the electron structure by one-particle Green's function and readily extended to the first-principles band structure unfolding method.

2.1 Density Functional Theory

We know that the quantum mechanical system is governed by the Schrödinger equation and particle statistics. The standard model of solid state physics is

composed of electrons, nuclei, and the Coulomb interaction between them. It is also common to use the Born-Oppenheimer approximation, which puts the attention on the electronic dynamics rather than the heavier nuclei. Thus, the non-relativistic Schrödinger equation [11] is

$$\big(-\frac{\hbar^2}{2m}\sum_i \nabla_i^2 - \sum_{i,n}\frac{Z_n e^2}{|r_i - R_n|} + \frac{1}{2}\sum_{i\neq j}\frac{e^2}{|r_i - r_j|}\big)\Psi = E\Psi, \qquad (2.1)$$

where r_i and R_n specify the positions of the electron and the nuclei respectively. Z_n, m (e), and $\hbar$ are the atomic number, electron mass (charge), and the Planck's constant. We usually assume the total electron number is N so the many-body wavefunction is represented as $\Psi = \Psi(r_1, r_2, \ldots r_N)$ subject to a minus sign when two fermionic electrons are permuted on both the space coordinate and spin. In principle, if the details of the inter-particle interaction is known, like the Coulomb interaction in Eq. 2.1, to solve its solution is seemingly a straightforward route to understand everything in solid state physics. However, a solvable wavefunction in many-body problems is very rare. The mind set to simply solve the many-body problem, which usually involves a particle number of $\sim 10^{23}$, is not practical. This difficulty of solving Eq. 2.1 had puzzled physicists for decades since only few accurate solutions are available in small systems, like H_2 molecule and He atom. Even with the most advanced computing resource to date, the exponentially growing Hilbert space still makes the quest to estimate Ψ a untractable task.

To seek an alternative route avoiding solving the full many-body Schrödinger equation, physicists started to be curious about whether there exists a basic quantity of prime importance to represent the whole quantum mechanical system. The answer had not been clear until the ground-breaking work by Hohenberg and Kohn in 1964 [13]. Now, the answer, ground state density $n(r)$, has been known and widely studied. The idea to utilize $n(r)$ was initiated by the Thomas-Fermi theory in 1920's [14, 15]. In the non-interacting and homogeneous Fermi gas, the relation between the uniform ground state density n_0 and the Fermi momentum p_F is $n_0 = \frac{8\pi}{3h^3}p_F^3$. As a very crude approximation, the formula is generalized to an inhomogeneous ground state density in the presence of slowly-varying potential as $n(r) = \frac{8\pi}{3h^3}p_F^3(r)$. In Thomas-Fermi

theory, the kinetic energy functional can be approximated as

$$T[n(r)] = \frac{3h^2}{10m}\left(\frac{3}{8\pi}\right)^{\frac{2}{3}} \int dr n^{5/3}(r), \tag{2.2}$$

and the potential term is the static Coulomb interaction between electronic densities

$$V[n(r)] = \frac{e^2}{2} \int \int \frac{n(r)n(r')}{|r-r'|} dr dr' + V^{ext}, \tag{2.3}$$

where V^{ext} denotes the external potential from the periodic potential from of the ions. Thus, the total energy, $T[n(r)] + V[n(r)]$, can be obtained merely by knowing the behavior of $n(r)$ instead of the full knowledge of the many-body wavefunction.

Despite the correct and qualitative trend in total energy estimation, Thomas-Fermi theory still lacks the consideration of chemical bonding and a rigorous connection to the many-body solution. The true electronic correlation is also poorly addressed. Later in 1964, the drawbacks were overcome by Hohenberg and Kohn's pioneering work, which formally established the uniqueness and usefulness of the ground state density [13]. Therefore, a new door to conquer the many-body system was opened then.

2.1.1 Hohenberg-Kohn Theorems

To review the density functional theory, I will start with the two basic Hohenberg-Kohn (HK) theorems, which lay the foundation for modern electronic structure calculations.

Theorem 1 *The ground state density $n(r)$ of a non-degenerate bound-state interacting electronic system uniquely determines the external potential $v^{ext}(r)$ apart from a trivial constant.*

Proof: *We start with an $n(r)$, which is the ground state density of a non-degenerate ground state wavefunction Ψ_1 with energy E_1 under the external potential $v_1^{ext}(r)$. We denote the corresponding Hamiltonian H_1 consisting of the kinetic energy operator T and electron-electron interaction U. Thus, the energy can be evaluated as*

$$E_1 = \langle \Psi_1 | H_1 | \Psi_1 \rangle = \langle \Psi_1 | T + U | \Psi_1 \rangle + \int v_1^{ext}(r) n(r) dr \tag{2.4}$$

Then, we suppose that there exists the second external potential $v_2^{ext}(r) \neq v_1^{ext}(r) + constant$*, which gives a distinct ground state wavefunction* $\Psi_2 \neq \Psi_1$ *but still shares the same density* $n(r)$ *with* $v_1^{ext}(r)$*. The new ground state energy can also be evaluated as*

$$E_2 = \langle \Psi_2 | H_2 | \Psi_2 \rangle = \langle \Psi_2 | T + U | \Psi_2 \rangle + \int v_2^{ext}(r) n(r) dr. \tag{2.5}$$

Because of the Rayleigh-Ritz variational principle, we have two inequalities:

$$\begin{aligned} E_1 &< \langle \Psi_2 | H_1 | \Psi_2 \rangle = \langle \Psi_2 | T + U | \Psi_2 \rangle + \int v_1^{ext}(r) n(r) dr \\ &= E_2 + \int [v_1^{ext}(r) - v_2^{ext}(r)] n(r) dr, \qquad (2.6) \\ E_2 &< E_1 + \int [v_2^{ext}(r) - v_1^{ext}(r)] n(r) dr. \qquad (2.7) \end{aligned}$$

Since the ground state is non-degenerate, the addition of the above two inequalities would lead to

$$E_1 + E_2 < E_1 + E_2, \tag{2.8}$$

which is obviously contradictory. Therefore, by reductio ad absurdum, the assumption that $v_2^{ext}(r) \neq v_1^{ext}(r) + constant$ *can still produce the same ground state density is false. The ground state density* $n(r)$ *must uniquely determine* $v^{ext}(r)$*, and Theorem 1 is proven.*

Because the ground state density uniquely determines both $v^{ext}(r)$ and N, the full Hamiltonian is also determined. In principle, all quantities are implicitly determined by $n(r)$, including the ground, excited wavefunction, and any Green's functions. Since $n(r)$ plays such a critical role in the quantum system, the next theorem will elaborate on the general principle to evaluate $n(r)$. [11, 16]

Theorem 2 *The total energy of the ground state can be obtained by variation with respect to the trivial density* $\tilde{n}(r)$ *instead of the trail wavefunction* $\tilde{\Psi}$*.*

Proof: *The original Rayleigh-Ritz variational principle is* $E = \min_{\tilde{\Psi}} \langle \tilde{\Psi} | H | \tilde{\Psi} \rangle$*. Since* $v^{ext}(r)$ *and* N *are uniquely determined by* $n(r)$*, so are* H *and the ground state wavefunction* Ψ_{GS}*. Thus,* $\Psi_{GS} = \Psi_{GS}[n(r)]$ *so the minimization of the*

ground state energy can be achieved by the variation of $n(r)$*. Therefore, Theorem 2 is also proven.*

The other informative perspective to discuss the ground state energy search was proposed by Levy [16]. We can finalize the search for the ground state energy by the following two steps. First, fixing $\tilde{n}(r)$, we assume that there is a set of trial wavefunctions $\tilde{\Psi}_\alpha$ corresponding to the same $\tilde{n}(r)$. With the constraint of fixed $\tilde{n}(r)$, the energy can be minimized by varying the $\tilde{\Psi}_\alpha$:

$$E_v[\tilde{n}(r)] = \min_\alpha \langle \tilde{\Psi}_\alpha | H | \tilde{\Psi}_\alpha \rangle = \int v^{ext}(r)\tilde{n}(r)dr + F[\tilde{n}(r)], \tag{2.9}$$

where $F[\tilde{n}(r)] \equiv \min_\alpha \langle \tilde{\Psi}_\alpha | T + U | \tilde{\Psi}_\alpha \rangle$ is a universal functional of $\tilde{n}(r)$ and has no explicit dependence on $v^{ext}(r)$. It means that $F[\tilde{n}(r)]$ characterizes the interaction between electrons only and does not depend on the details of the system. The second step is to utilize the fact that the ground state has the lowest possible total energy so E can be obtained by varying $\tilde{n}(r)$.

$$E = \min_{\tilde{n}(r)} \int v^{ext}(r)\tilde{n}(r)dr + F[\tilde{n}(r)]. \tag{2.10}$$

Therefore, the minimizing $\tilde{n}(r)$ would be the ground state density $n(r)$.

Assuming $F[\tilde{n}(r)]$ is known, the goal to obtain the total energy by varying Ψ is simplified to controlling a three-dimensional quantity $\tilde{n}(r)$ only. However, the *a priori* accurate knowledge of $F[\tilde{n}(r)]$ is not available and its needs further approximation to implement the formalism into practice. In order to show the rough idea about $F[\tilde{n}(r)]$, we recall the Thomas-Fermi theory and borrow their crude approximation on the global functional:

$$F^{TF}[n(r)] = T + U = \frac{3h^2}{10m}\left(\frac{3}{8\pi}\right)^{\frac{2}{3}} \int dr n^{5/3}(r). + \frac{e^2}{2}\int \frac{n(r)n(r')}{|r-r'|}drdr'. \tag{2.11}$$

The format of the kinetic functional indicates that the concept is still related to the uniform electron gas. Also, the electron-electron interaction is in the mean-field level without the consideration of rigorous exchange and correlation effects. Unfortunately, the full knowledge of rigorous $F[n(r)]$ requires the solution of the many-body system and is only approximated with various assumption schemes.

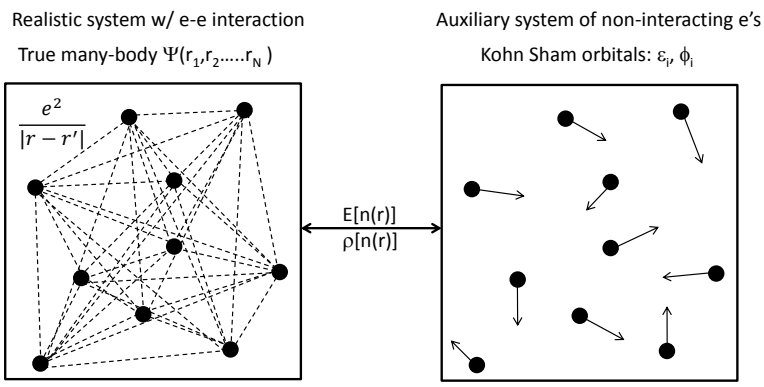

Figure 2.1: Interacting electronic and non-interacting Kohn-Sham systems.

2.1.2 Kohn-Sham Equation

Although the Hohenberg-Kohn theorems are extremely powerful and general, the practical computation of the ground state energy is not explicitly provided. One year after the Kohn and Sham's publication, Kohn and Sham designed a practical approach to implement the density functional theory. [17]

Since a modification of $v^{ext}(r)$ would only change the ground state density, there is freedom to map the interacting $F[n(r)]$ as in the left panel Fig. 2.1 to an auxiliary non-interacting system as in the right panel Fig. 2.1, which still share the same $n(r)$ with the original interacting system. This treatment simplifies the wavefunction of the auxiliary system as a single determinant consisting of various occupied orbitals.

$$\Psi_{KS} = \frac{1}{\sqrt{N}}\det[\phi_1(r_1)\phi_2(r_2)\cdots\phi_N(r_N)] \tag{2.12}$$

Keeping the trivial density-density Hartree interaction terms, Kohn and Sham separated the $F[n(r)]$ into three parts:

$$F[n(r)] = T_s[n(r)] + \frac{e^2}{2}\int\frac{n(r)n(r')}{|r-r'|}drdr' + E_{xc}[n(r)], \tag{2.13}$$

where $T_s[n(r)]$ and $E_{xc}[n(r)]$ are the kinetic energy functional for the non-interacting system and the exchange-correlation energy functional respectively. It is noted that Eq. 2.13 attempts to capture the spirit of the one-particle Hartree equations [6] with wavefunction in the form of Ψ_{KS} and is also the

definition of $E_{xc}[n(r)]$. If we apply the second HK theorem,

$$E = \min_{n(r)} \big(\int v^{ext}(r) n(r) dr + T_s[n(r)] + \frac{e^2}{2} \int \frac{n(r)n(r')}{|r-r'|} dr dr' + E_{xc}[n(r)] \big). \tag{2.14}$$

With the fixed total electron number ($N = \int n(r)dr$) as the constraint ($\int \delta n(r) = 0$), the Euler-Lagrange equation is

$$\int \delta n(r) \big(\frac{\delta T_s[n(r)]}{\delta n(r)} + v^{ext}(r) + e^2 \int \frac{n(r')}{|r-r'|} dr' + \frac{\delta E_{xc}[\delta n(r)]}{\delta n(r)} - \mu \big) dr = 0, \tag{2.15}$$

where μ is the Lagrange multiplier. It becomes clearer if we refine the following quantities:

$$\begin{aligned} v_{eff}(r) &\equiv v^{ext}(r) + e^2 \int \frac{n(r')}{|r-r'|} dr' + v_{xc}(r). \\ v_{xc}(r) &\equiv \frac{\delta}{\delta n(r)} E_{xc}[n(r)]. \end{aligned} \tag{2.16}$$

Thus, the variational equation is simplified to

$$\delta T_s + v_{eff} \delta n(r) = \mu \delta n(r) \tag{2.17}$$

We consider the auxiliary non-interacting system with a set of N one-particle orbitals $\phi_i(r)$ to reproduce the same electron density as the true interacting electron system. Thus,

$$n(r) = \sum_i^N |\phi_i(r)|^2. \tag{2.18}$$

$$\delta n(r) = \sum_i^N [\delta \phi_i^*(r)] \phi_i(r) + \phi_i^*(r) \delta \phi_i(r)]. \tag{2.19}$$

The non-interacting kinetic energy functional is

$$T_s[n(r)] = -\frac{\hbar^2}{2m}\sum_i^N \int \phi_i^*(r)\nabla^2\phi_i(r)dr \tag{2.20}$$

$$\delta T_s[n(r)] = -\frac{\hbar^2}{2m}\sum_i^N \int \left[\delta\phi_i^*(r)\nabla^2\phi_i(r) + \nabla^2\phi_i^*(r)\delta\phi_i(r)\right]dr \tag{2.21}$$

Another Lagrangian multiplier ε_i is needed to satisfy the normalization constraint $\int \phi_i^*(r)\phi_i(r)dr = 1$.

Collect all terms with $\delta\phi^*(r)$ in Eq. 2.17, the Lagrange equation becomes

$$\left[-\frac{\hbar^2}{2m}\nabla^2 + v_{eff}(r)\right]\phi_i(r) = \varepsilon_i\phi_i(r). \tag{2.22}$$

The original many-body problem is transformed into a one-particle equation solved by the self-consistent loop. Eq. 2.22 is usually called the Kohn-Sham (KS) equation. Once the eigenfunction $\phi_i(r)$ and eigenvalue ε_i are found, we can reconstruct the ground state density by Eq. 2.18. While the eigenenergy does not have a direct physical meaning, it can be used to reconstruct the total energy. From the Kohn-Sham functional in Eq. 2.13,

$$\sum_i^N \varepsilon_i = T_s + \int v^{ext}(r)n(r)dr + e^2\int \frac{n(r)n(r')}{|r-r'|}drdr' + \int v_{xc}(r)n(r)dr. \tag{2.23}$$

Then, the total energy can be represented as

$$E = \sum_i^N \varepsilon_i - \frac{e^2}{2}\int \frac{n(r)n(r')}{|r-r'|}drdr' + E_{xc}[n(r)] - \int v_{xc}(r)n(r)dr. \tag{2.24}$$

It is noted that if $E_{xc}[n(r)]$ and $v_{xc}[n(r)]$ are made zero, the Eq. 2.22 is reduced to the Hartree equation. It means that the many-body correlation is encapsulated in the $E_{xc}[n(r)]$ functional, so the question of how to approximate it within a reasonable computational time scale determines the practical applicability of the Kohn-Sham equation.

One should be cautious that ε_i and $\phi_i(r)$ only serve an auxiliary purpose and do not possess a true physical meaning. [11] Only the $n(r)$ is a physical observable. In practice, ε_i and $\phi_i(r)$ in weakly correlated systems are not very

different from the solution calculated by the Hartree equation. Therefore, they are often interpreted as the eigenstate and dispersion in the band structure theory.

2.1.3 Local Density Approximation

Density functional theory with Kohn-Sham equation has a built-in rigorous mathematical formalism for solving electronic structure. Still required is a good scheme to approximate the functional $E_{xc}[n(r)]$ and complete the equation. In the viewpoint of the Kohn-Sham framework, $E_{xc}[n] = (T[n] - T_s[n]) + (V_{e-e} - V_H)$, but the exact functional dependence on $n(r)$ is unknown. Depending on the purpose or accuracy, many kinds of approximation have been proposed in either molecular or solid state systems, but the full discussion is beyond the scope of this thesis. I will focus on the local density approximation (LDA), which is the most basic one and is widely used in solid state materials.

As the simplest approximation, LDA takes a slowly-varying density into consideration. One can imagine that the most straightforward way is to represent the functional form in the following local format [18]

$$E_{xc}^{LDA}[n(r)] = \int e_{xc}(n(r))n(r)dr, \tag{2.25}$$

where e_{xc} is the exchange-correlation energy per electron. Because e_{xc} only senses the local value of n at position r, the dependence is reduced to a simplified function relation instead of the original functional one. Further approximation can be taken from the well-known relation between e_{xc} and n in the uniform Fermi gas, where $e_{xc}(n) = e_x(n) + e_c(n)$. From Ref. [18], one can know the exchange part as

$$e_x(n) = -\frac{3}{4\pi}(3\pi^2 n)^{1/3}. \tag{2.26}$$

However, the correlation energy has no general closed forms. In the high electron density limit, it can be approximated as [18]

$$e_c(n) = c_0 \ln r_s - c_1 + c_2 r_s \ln r_s - c_3 r_s + \ldots (r_s \to 0), \tag{2.27}$$

where r_s is the Wigner-Seitz radius $r_s \equiv (3/4\pi n)^{1/3}$. The constants c_i can be determined by many-body perturbation theory. To obtain a more accurate

value for $e_c(n)$ of arbitrary electron density, one usually consults the numerical result from the quantum Monte Carlo simulation. [19] Thus, $e_{xc}(n)$ can be readily plugged into Eq. 2.22 and completes the KS equation. The solution of KS equation with LDA (and its variants) has proved an astonishing accuracy with experimental values in ionization energy of atoms, the bond length for molecules and the cohesive energy in realistic materials. [20]

2.2 Wavefunction in Matter

In this section, I will start with the Bloch theorem to discuss the general formalism of the wavefunction in a periodic potential, to which the effective KS potential belongs. To obtain the first-principles band structure by combining the Bloch theorem and density functional theory, a linearized augmented plane wave basis can significantly reduce the computational expense. In the end, I will proceed to introduce the concept of Wannier orbitals, which is the real-space counterpart of the Bloch wave.

2.2.1 Bloch wavefunction

The Bloch wave is the wavefunction for a single particle moving in the periodic potential and has the eigen-energies corresponding to the band structure of the electron in the crystal. In a fictitious case of periodic potential magnitude turned to zero, it is reduced to the free particle problem with the straightforward plane wave solution e^{ikr} to the Schrödinger's equation. The k represents the physical momentum of the electron. Once the periodic potential is present, Felix Bloch showed the wavefunction becomes.

$$\psi_{kj}(r) = e^{ikr} u_{kj}(r), \tag{2.28}$$

where $u_{kj}(r)$ is a periodic wavefunction with $u_{kj}(r) = u_{kj}(r + R)$ and R is a lattice vector of crystal [6]. The quantum number j is the band index and distinguishes different eigenenergy ε_{kj} for the same momentum k. Because the continuous translational symmetry has been broken by the periodic potential term, k labels the so-called crystal momentum instead of the true linear momentum in the free electrons. Its meaning will be clear in the following

discussion.

Theorem 3 *If the potential $V(r)$ is periodic with the periodicity of the lattice, namely $V(r) = V(r+R)$, then the eigenfunctions of the Schrödinger's equation*

$$H\psi_k(r) = \big[-\frac{\nabla^2}{2m} + V(r)\big]\psi_k(r) = E\psi_k(r) \tag{2.29}$$

have the form $\psi_k(r) = e^{ikr}u(r+R)$, where $u(r) = u(r+R)$.

The rigorous proof can be found in most solid state textbooks [5, 6]. Now, we consider a more elegant perspective based on a group theory treatment [5]. Let us start with a one-dimensional case, the lattice translation operator in its defining representation is

$$\mathbf{T}r = r + a, \tag{2.30}$$

where a the primitive vector of the one-dimensional lattice. Since $\big[\mathbf{T}, H\big] = 0$, we want to construct the wavefunction $\psi(x)$ to be the simultaneous eigenstate of Hamiltonian and translational operator. Namely,

$$H\psi(r) = E\psi(r). \tag{2.31}$$

$$\mathbf{T}\psi(r) = t\psi(r). \tag{2.32}$$

Also, we assume the periodic boundary condition with N unit cells, namely $\psi(x + Na) = \psi(x)$. By exploring the boundary condition,

$$\mathbf{T}^N\psi(x) = t\mathbf{T}^{(N-1)}\psi(x+a) = \ldots = t^N\psi(x+Na) = t^N\psi(x). \tag{2.33}$$

Due to the normalization of the wavefunction, we know that the eigenvalue t must satisfy $|t| = 1$ and $t^N = 1$. Thus, we can choose $t = e^{i2\pi m/N}$, where $m =$ 1, 2, ... N. One conventional choice is to define $-\frac{\pi}{a} \leq k < \frac{\pi}{a}$ so that

$$t = e^{ika}, \tag{2.34}$$

where $k = -\frac{\pi}{a}, -\frac{\pi}{a} + \frac{2\pi}{Na}, -\frac{\pi}{a} + \frac{4\pi}{Na}, \cdots, \frac{\pi}{a} - \frac{2\pi}{Na}$. Because of the 2π periodicity of the phase, $k + \frac{2\pi}{a} \times (\textit{any integer})$ is physically equivalent to k. Hence, k, named crystal momentum, does not only denote a single momentum but represents

all equivalent ones. Therefore, it is natural to label the wavefunction by k and require $\psi_k(x) = e^{ikx}u_k(x)$ with $u_k(x) = u_k(x + la)|_{l=integer}$ to satisfy Eq. 2.32. This is the Bloch theorem in the one-dimensional case.

To generalize the statement to three-dimensional space with a_1, a_2 and a_3 the primitive vectors of the lattice, we define a reciprocal space lattice by the following reciprocal primitive vectors:

$$b_1 \equiv 2\pi\Big[\frac{a_2 \times a_3}{a_1 \cdot (a_2 \times a_3)}\Big]. \tag{2.35}$$

$$b_2 \equiv 2\pi\Big[\frac{a_3 \times a_1}{a_1 \cdot (a_2 \times a_3)}\Big]. \tag{2.36}$$

$$b_3 \equiv 2\pi\Big[\frac{a_1 \times a_2}{a_1 \cdot (a_2 \times a_3)}\Big]. \tag{2.37}$$

It is easy to check

$$a_i \cdot b_j = 2\pi\delta_{ij}, \tag{2.38}$$

Since Eqs. 2.32 and 2.33 can be generalized to the case with three primitive vectors, the complete Bloch theorem becomes $\psi_k(r)$ as $e^{ikr}u_k(r)$ with $u_k(r) = u_k(r + R)$.

By applying the Bloch theorem, the self-consistent Kohn-Sham equation can be iteratively solved by looking for the Bloch wave of individual k under the Kohn-Sham effective potential. The electronic density can be reconstructed as $n(r) = \sum_{kj,\varepsilon_{kj}<E_F} |\psi_{kj}(r)|^2$.

2.2.2 Linearized Augmented Plane Wave Basis

In this subsection, I will briefly introduce the linearized augmented plane wave (LAPW) basis, in which solving the Kohn-Sham equation with the full-electron calculation will be reasonably efficient. Among all possible basis sets, the most natural choice will be either plane waves or local atomic orbitals. Both are complete and orthogonal sets of basis. They are also easy implemented in programming and numerical computation. However, the former is incapable of describing the core and semi-core electrons. It is because when describing the nodal structure of the radial wavefunction very close to the nuclei, one should include very large wave vectors and this makes the numerical Hamiltonian size unmanageably high. The latter is also inadequate to capture the itinerancy

of the valence electrons very well. This reason is that very high orders of spherical harmonics are needed to simulate the wavefunction behavior close to a plane wave.

To complement the disadvantages of the two bases mentioned above, one feasible way is a new set of basis utilizing their advantages in the suitable places. This basis is called augmented plane wave [21]. For each individual atom α, we assign a muffin-tin region S^α enclosed by a specified radius R^α, and represent the wavefunction in S^α by the local atomic orbitals. The interstitial, the space not covered by any muffin tins, has the wavefunction expanded by the plane wave basis. Thus, the general wavefunction can be represented as [21]

$$\phi_K^k(r,E) = \begin{cases} \frac{1}{\sqrt{V}} e^{i(k+K)r}, & \text{if } r \in \text{Interstitial} \\ \sum_{lm} A_{lm}^{\alpha,k+K} u_l^\alpha(\underline{r},E) Y_m^l(\hat{\underline{r}}), & \text{if } r \in S^\alpha \end{cases} \tag{2.39}$$

where $\underline{r}$ and $\hat{\underline{r}}$ denote $r - r^\alpha$ and its solid angle respectively. For each independent quantum number k, the wavefunction $\psi_{kj}(r)$ consists the component $\phi_K^k(r,E)$ weighted by $c_{k+K,j}$ of all possible reciprocal lattice vectors K. V is the unit cell volume as the normalization constant. Inside each muffin tin, $u_l^\alpha(\underline{r},E)Y_m^l(\hat{\underline{r}})$ is the solution of the free-atom Schrödinger equation with boundary condition of having a vanishing value on the muffin tin radius. Thus, the energy E is not quantized as the Hydrogen atom problem but becomes a continuous spectrum calculated numerically. It is part of the basis function and does not carry a physical meaning.

If we expand the plane wave into the superposition of Bessel functions and spherical harmonics, we can match the wavefunction to obtain the coefficients in closed form:

$$A_{lm}^{\alpha,k+K} = \frac{4\pi i^l e^{(k+K)R_\alpha}}{\sqrt{V} u_l^\alpha(R_\alpha,E)} j_l(|k+K|R_\alpha) Y_m^l(\widehat{k+K}). \tag{2.40}$$

This augmented plane wave basis is seemingly efficient in describing the characteristics of the Bloch wave in different regions. We only need to make a reasonable truncation on the maximum values of the angular momentum quantum number l_{max} and the maximum reciprocal lattice vector K_{max}. The remaining ambiguity is the undetermined variable E. In principle, E should

be matched with the energy eigenvalues ε_{kj}, for which we need to solve the Kohn-Sham equation. Unfortunately, it turns out that we need to start with a set of guessed E's and introduce an extra self-consistent loop to reach the convergence in E.

To prevent the extra numerical work in searching for E, we have to implement a smarter way to estimate $u_l^\alpha(\underline{r}, \varepsilon_{kj})$ without extra computational cost. One way is to use LAPW [21]. We assume that an assigned E_0 is not too far from ε_{kj} so $u_l^\alpha(\underline{r}, \varepsilon_{kj})$ can be evaluated as

$$u_l^\alpha(\underline{r}, \varepsilon_{kj}) = u_l^\alpha(\underline{r}, E_0) + (E_0 - \varepsilon_{kj})\frac{\partial u_l^\alpha(\underline{r}, E)}{\partial E}|_{E=E_0} + O\big[(E_0 - \varepsilon_{kj})^2\big]. \quad (2.41)$$

A suitable E_0 should be chosen as close to ε_{kj} as possible for all k's. In practice, one band complex is dominated by a few orbitals l's of the atom α. The better strategy is to assign E_0 to be located at the band center. This minimizes the error term $O((E_0-\varepsilon_{kj})^2)$ and saves the numerical efforts. Usually, the relevant density is the valence electron density, which is dominated by low l, such as s, p, d, or at most f. Therefore, we specifically estimate those relevant l's and leave the other large l orbitals to share a single E_0. The formalism of LAPW would be as follows:

$$\phi_K^k(r, E) = \begin{cases} \frac{1}{\sqrt{V}} e^{i(k+K)r}, & \text{if } r \in \text{Interstitial.} \\ \sum_{lm} \big(A_{lm}^{\alpha,k+K} u_l^\alpha(\underline{r}, E_l^\alpha) + B_{lm}^{\alpha,k+K} \dot{u}_l^\alpha(\underline{r}, E_l^\alpha)\big) Y_m^l(\hat{\underline{r}}), & \text{if } r \in S^\alpha, \end{cases} \quad (2.42)$$

where $\dot{u}_l^\alpha$ denotes the energy derivative of u_l^α. The coefficients $A_{lm}^{\alpha,k+K}$ and $B_{lm}^{\alpha,k+K}$ can be evaluated by simultaneously matching the wavefunction value and its radial derivative on the muffin tin radius. The usage of LAPW and its variants are well implemented in WIEN2k, which I heavily used to study the first-principles electron structure. Combining the DFT, Bloch theorem, and LAPW, the Kohn-Sham equation can be readily solved by the simplified flow chart in Fig. 2.2. The three key ingredients, Kohn-Sham potential, Kohn-Sham orbitals, and ground state density would be updated in each iteration until their values are convergent.

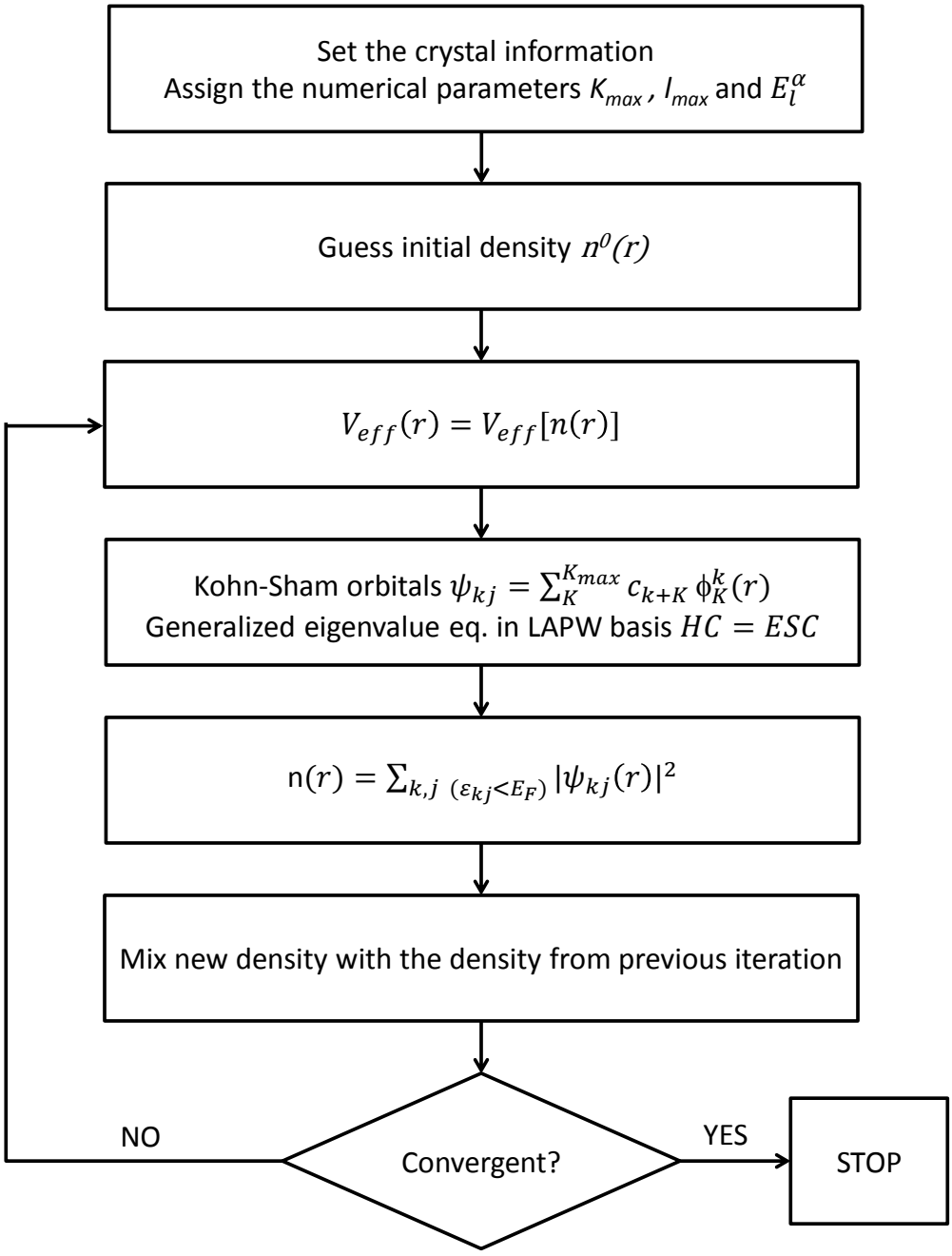

Figure 2.2: Flow chart of solving Kohn-Sham orbitals in the LAPW basis.

2.2.3 Wannier Functions in Solid State Physics

Wannier functions, introduced by Gregory Wannier [22], are a complete set of orthogonal wavefunctions, which are localized in real space. In principle, the Wannier basis is constructed from the Fourier transform of the Bloch wave and no longer corresponds to a specific eigenenergy. Complementary to the energy band and spatially extended features of the Bloch waves, Wannier functions provide the real-space perspective to the electronic structure. First, the hybridization between two Wannier orbitals reveals the nature of chemical bonding. Second, the on-site energy of a single Wannier orbital indicates how its energy scale is impacted by the surrounding chemical environment. Third, Wannier orbitals provide a compact format of the real-space Hamiltonian, which can facilitate the applications modeling true many-body effects.

In the early development, the Wannier functions were only used to help derivations in fundamental theorems but were rarely calculated for their own application. After the framework of solving Kohn-Sham equation for the band structure became the standard procedure in first-principles method, its actual demonstration drew physicists' attention again in the late 90s and was quickly applied to research in various disciplines.

We can start with considering a simplified single-band model [5] with a known Bloch state $\psi_k(r) = e^{ikr}u_k(r)$. Thus, the Wannier functions centered at each lattice point R are

$$w_R(r) = w(r-R) = \frac{1}{\sqrt{N}} \sum_{k \in BZ} e^{-ikR}\psi_k(r), \tag{2.43}$$

where the R is the lattice vector and N is the number of unit cells. It is noted that $w_R(r)$ only depends on $r - R$ and its orthogonality is shown as

$$\begin{aligned} \int w(r-R)w(r-R')dr &= \frac{1}{N}\sum_{k,k'} \int e^{ikR}\psi_k^*(r)e^{-ik'R'}\psi_{k'}(r)dr \\ &= \frac{1}{N}\sum_{k,k'} e^{ikR}e^{-ik'R'}\delta_{k,k'} = \delta_{R,R'}, \end{aligned} \tag{2.44}$$

Although multi-orbital systems can be described in the same spirit, the

Bloch wave, as we know, is subject to a non-physical arbitrary phase

$$|\tilde{\psi}_k\rangle = e^{i\varphi(k)}|\psi_k\rangle, \tag{2.45}$$

where $\varphi(k)$ will not change any physical observables. For sure, different phase choices will lead to different cancellation in the Fourier transform so that the resulting Wannier functions will change the shape and the extent of spreading accordingly. On the other hand, the absence of a well-defined connection between the Bloch band index j and the Wannier orbital n brings another ambiguity to such a transformation. Generally speaking, these two effects are included in the k-dependent gauge denoted by a unitary matrix U_{ij}^k, and all gauge-equivalent states $|\tilde{\psi}_{ki}\rangle$ can be represented as

$$|\tilde{\psi}_{ki}\rangle = \sum_j U_{ij}^k |\psi_{kj}\rangle. \tag{2.46}$$

Only when U_{ij}^k is well-chosen, the corresponding Wannier functions are

$$w_{Rn}(r) = \frac{1}{\sqrt{N}} \sum_{k \in BZ} e^{-ikR} \sum_j U_{nj}^k \psi_{kj}(r), \tag{2.47}$$

where n represents the Wannier orbital indices, including both atomic and orbital types.

From the first-principles aspect, there exist two conventional ways to fix the U_{ij}^k gauge to define either maximally-projected or maximally-localized Wannier functions [23]. Starting from a trial local orbital $g_n(r)$ roughly in the shape of the atomic basis, the $g_n(r)$ should carry the conventional symmetries, like s, p_x, p_y, p_z and so on. For example, the atomic wavefunction in the muffin tin of the LAPW basis is a suitable choice. We would try to the construct a sub-space by projecting Kohn-Sham orbitals into $g_n(r)$ as

$$|\phi_{kn}\rangle = \sum_j |\psi_{kj}\rangle\langle\psi_{kj}|g_n\rangle, \tag{2.48}$$

When $|\phi_{kn}\rangle$ is chosen as the initial guess, it does not guarantee to form a orthonormal basis. By using the Lowdin orthogonalization [23], we can minimally adjust the basis to achieve orthonormality. The resulting complete basis

at each k is

$$|w_{kn}\rangle = \sum_j |\phi_{km}\rangle (S_k)^{-1/2}_{mn}, \tag{2.49}$$

where $(S_k)_{mn} \equiv \langle \phi_{km} | \phi_{kn} \rangle$ and $S^{-1/2}$ can be computed by using an eigenvalue decomposition. The gauge has been fixed by the time $g_n(r)$ is chosen. The Wannier functions from this construction are called the maximally-projected Wannier functions, which will strictly follow the orbital symmetry of $g_n(r)$.

Maximally localized Wannier functions, formulated by Marzari and Vanderbilt [23], are constructed by the criteria to maximize the localization of the orbitals. Through the process to minimize the Wannier orbital spreading in space, the gauge will be also fixed. In practice, a localization functional is defined as

$$\Omega = \sum_n [\langle 0n|r^2|0n\rangle - |\langle 0n|r|0n\rangle|^2] \tag{2.50}$$

to measure the spreading sum of all Wannier functions within the unit cell. The task can be done by re-writing Ω in terms of the Kohn-Sham orbitals and U^k_{ij} so one can reduce Ω iteratively and achieve the minimum spreading.

One most important advantage to use a first-principles Wannier function basis is the so-called band structure down-folding, which extracts the effective low-energy Hamiltonian containing the minimal orbitals of interest. The complex DFT information will be compressed into a tight-binding Hamiltonian in the form of $\langle Rn|H|R'n'\rangle$, where R' can be taken as zero due to translational invariance.

Here, we show two examples from the practical implementation of the maximally-projected Wannier functions constructed from the DFT results of the WIEN2k package. As in the GaAs case in Fig. 2.3, we present the s and p's Wannier orbitals of Ga and As within energy window [-14:12] eV and plot its dispersion the red as the curves. They match the DFT dispersion in the black dots very well. The reduction of the basis number from LAPW to the Wannier orbitals has a factor of twenty ($\sim 168/8$). This means that the computational efficiency for either band structure or other observables is dramatically improved. This is why we can easily plot the dispersion in the continuous fashion by Wannier interpolation. This computational difference is more prominent in the system with the large unit cell. For example, to simulate the electronic structure in the carbon nanotube of (5,5) chirality

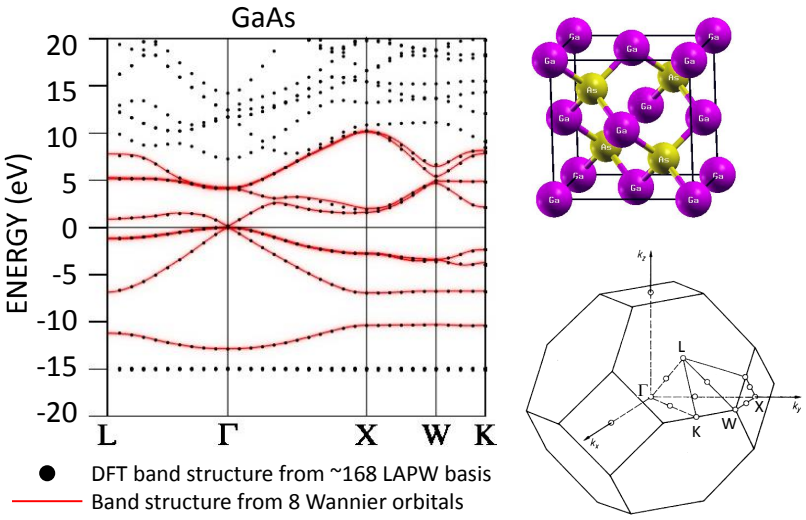

Figure 2.3: (Left) GaAs Band structures from DFT and maximally-projected Wannier functions. The Wannier functions include Ga orbitals (s, p_x, p_y, and p_z) and As orbitals (s, p_x, p_y, and p_z). (Right,upper) Crystal structure and (Right, lower) Brillouin zone.

(see right panel of Fig. 2.4), ∼7284 LAPW's in DFT are needed to represent the 20 carbon atoms and the large inserted vacuum. The ratio bursts into $7284/80 \approx 100$. The resulting DFT band structure in the black dots in Fig. 2.4 becomes the atomic/molecular-like spectrum with discrete energies. After it is converted to maximally-projected Wannier functions of carbon s and p's orbitals, the Hilbert space is largely reduced to the size of 80 orbitals and enables us to draw the continuous/meaningful dispersion in a short time as in the left panel of Fig. 2.4.

2.3 One-particle Spectral Function, Photoemission Spectral Weight and Band Structure Unfolding

In this section, I will review the representation of the electronic structure by the one-particle spectral function and the spectroscopic experiments to probe it. Then, in the presence of translational symmetry breaking, the band structure unfolding method provides a more meaningful representation in terms of

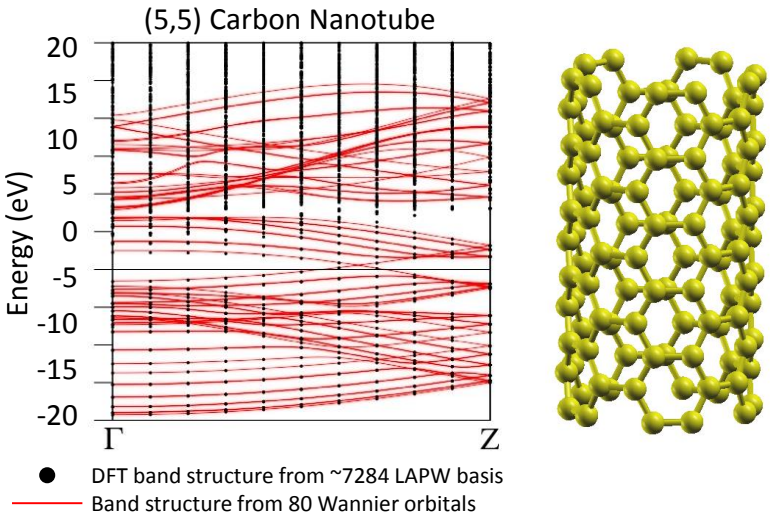

Figure 2.4: (Left) Carbon nanotube with chirality (5,5) band structures from DFT and maximally-projected Wannier functions. The Wannier functions include s, p_x, p_y, and p_z from the 20 carbon atoms in the minimal unit cell. (Right) Crystal structure.

physical implications.

2.3.1 Many-body Green's Function and Spectral Representation

To discuss the one-particle spectral function in the many-electron system, we need to introduce the fermionic field operators [24], $\hat{\psi}(x,t)$ and $\hat{\psi}^\dagger(x,t)$, to describe the electrons' behavior. They satisfy the anticommutation relation $\hat{\psi}(x)\hat{\psi}^\dagger(x') + \hat{\psi}^\dagger(x')\hat{\psi}(x) = \delta(x-x')$ due to the Pauli exclusion principle. In the Heisenberg picture, the time evolution is represented as $\hat{\psi}(x,t) = e^{iHt}\hat{\psi}(x)e^{-iHt}$, where $\hbar$ is taken as one here and the following. The time-ordered one-particle Green's function is defined as

$$iG(x,t,x',t') = \theta(t-t')\langle 0|\hat{\psi}(x,t)\hat{\psi}^\dagger(x',t')|0\rangle - \theta(t'-t)\langle 0|\hat{\psi}^\dagger(x',t')\hat{\psi}(x,t)|0\rangle, \tag{2.51}$$

where $\theta(t)$ and $|0\rangle$ are the step function and many-body ground state with fixed particle number N. We consider that H has no explicit time dependence so we can take t' as zero for simplicity. If we insert the completeness relation

$\sum_m |m\rangle\langle m|$, where $|m\rangle$ refers to all possible eigenstates of H,

$$\begin{aligned} iG(x,t,x',0) &= \sum_m \big[\theta(t)e^{-i(E_m^{N+1}-E_0^N)t}\langle 0|\hat{\psi}(x)|n\rangle\langle n|\hat{\psi}^\dagger(x')|0\rangle \\ &- \theta(-t)e^{+i(E_m^{N-1}-E_0^N)t}\langle 0|\hat{\psi}^\dagger(x')|n\rangle\langle n|\hat{\psi}(x)|0\rangle\big], \end{aligned} \tag{2.52}$$

where $E_m^{N\pm1}$ is the eigenenergy of $|m\rangle$ in $N\pm1$ particle number sector. With the identity

$$\theta(\pm t) = \mp\int \frac{d\omega}{2\pi i}\frac{e^{-i\omega t}}{\omega \pm i\eta}, \tag{2.53}$$

where η means an infinitesimal positive number. Then, we can transform G to the frequency domain as

$$\begin{aligned} G(x,x',\omega) &= \sum_m \big[\frac{\langle 0|\hat{\psi}(x)|m\rangle\langle m|\hat{\psi}^\dagger(x')|0\rangle}{\omega-(E_m^{N+1}-E_0^N)+i\eta} \\ &+ \frac{\langle 0|\hat{\psi}^\dagger(x')|m\rangle\langle m|\hat{\psi}(x)|0\rangle}{\omega+(E_m^{N-1}-E_0^N)-i\eta}\big]. \end{aligned} \tag{2.54}$$

From this representation, the poles of G clearly correspond to the quasiparticle and quasihole excitation energies in the first and second terms respectively. If H is translational invariant in space, its eigenstates have the specific momentum p as the quantum number. With the spatial Fourier transform and $\hat{\psi}(r) = e^{-ipr}\hat{\psi}(0)e^{+ipr}$, the spectral representation of G is

$$G(p,\omega) = \int_0^\infty dE \frac{A(p,E)}{\omega-E+i\eta} + \frac{B(p,E)}{\omega+E-i\eta}, \tag{2.55}$$

where $A(p,E) = \sum_m \delta\big(E-(E_m^{N+1}-E_0^N)\big)|\langle m,p|\hat{\psi}^\dagger(p)|0\rangle|^2$ and $B(p,E) = \sum_m \delta\big(E-(E_m^{N-1}-E_0^N)\big)|\langle m,-p|\hat{\psi}(p)|0\rangle|^2$. The Fourier transform of the field operator is $\hat{\psi}(p) \equiv \int e^{-ipr}\hat{\psi}(r)dr$. Besides, $|m,\pm p\rangle$ denotes the excited state with total momentum $\pm p$ in the $(N\pm1)$ particle number sector. Also, A and B are called the spectral weight to denote the available weight on the specific quasiparticle and quasihole frequencies.

The above consideration is for the continuous system. In the solid with the periodic potential, a convenient formalism starts with expanding the field operator in the local Wannier function basis $\hat{\psi}(x) = \sum_{r_i n} c_{in} w_{r_i n}(x)$, where c_{in} is the annihilation operator on the Wannier orbital n in the unit cell at r_i.

Then we can work on the discrete system and obtain

$$iG_{in,i'n'}(t) = \theta(t)\langle 0|c_{in}(t)c^{\dagger}_{i'n'}(0)|0\rangle - \theta(-t)\langle 0|c^{\dagger}_{i'n'}(0)c_{in}(t)|0\rangle. \tag{2.56}$$

If H has translational invariance in space, its eigenstate has a crystal momentum k. With the spatial Fourier transform with respect to $(r_i - r_{i'})$ and $c_i = e^{-ikr}c_0e^{+ikr}$, the corresponding spectral representation in the crystal momentum basis is

$$G_{nn'}(k,\omega) = \int_0^{\infty} dE \frac{A_{nn'}(k,E)}{\omega - E + i\eta} + \frac{B_{nn'}(k,E)}{\omega + E - i\eta}, \tag{2.57}$$

where $A_{nn'}(k,E) = \sum_m \delta\big(E - (E^{N+1}_m - E^N_0)\big)\langle 0|c_{kn}|m,k\rangle\langle m,k|c^{\dagger}_{kn'}|0\rangle$ and $B_{nn'}(k,E) = \sum_m \delta\big(E-(E^{N-1}_m-E^N_0)\big)\langle 0|c^{\dagger}_{kn'}|m,-k\rangle\langle m,-k|c_{kn'}|0\rangle$ Also, $c_{kn} \equiv \sum_{r_i} e^{-ikr_i}c_{in}$. Besides, $|m,\pm k\rangle$ denotes the excited state with total momentum $\pm k$ in the $(N \pm 1)$ particle number sector.

It is noted that the above formalism is correct for the general interacting system and also leads to a useful insight in the non-interacting system, such as the band structure based on the KS orbitals. In the eigenstate basis of the non-interacting system, we have

$$G_{jj'}(k,\omega) = \frac{\delta_{jj'}}{\omega - \varepsilon_{kj} + i\eta\mathrm{sign}(\varepsilon_{kj})}, \tag{2.58}$$

where the Fermi energy is chosen at zero energy, and sign(x) $\equiv x/|x|$. Then ε_{kj} refers to the eigenenergy with respect to the Fermi energy. For convenience and avoiding the extra sign changing, we replace the time-ordered Green's function $G_{jj'}(k,\omega)$ by the retarded Green's function

$$G^R_{jj'}(k,\omega) = \frac{\delta_{jj'}}{\omega - \varepsilon_{kj} + i\eta}. \tag{2.59}$$

Thus, we can trace the momentum and energy dependent band dispersion by plotting $-\frac{1}{\pi}\mathrm{Im}G^R_{j,j}(k,\omega)$ with a series of Lorentzian peaks of infinitesimal width. Thus, we define the one-particle spectral function in the band basis as

$$A_j(k,\omega) \equiv -\frac{1}{\pi}\mathrm{Im}G^R_{j,j}(k,\omega). \tag{2.60}$$

In the orbital basis, $-\frac{1}{\pi}\mathrm{Im}G^R_{n,n}(k,\omega)$ still follows the dispersion and carries the weight as $|\langle kj|kn\rangle|^2$, which describes the orbital weight on each eigenstate. Instead of keeping track of the dispersion like the black dots in Fig. 2.3, the better way to represent the band structure is plotting the $-\frac{1}{\pi}\mathrm{Im}G^R_{n,n}(k,\omega)$. Thus, we define the (orbital-resolved) one-particle spectral function as

$$A_n(k,\omega) \equiv -\frac{1}{\pi}\mathrm{Im}G^R_{n,n}(k,\omega). \tag{2.61}$$

This can be readily calculated from the effective Hamiltonian of the Wannier basis as

$$A_n(k,\omega) = \sum_j |\langle kj|kn\rangle|^2 A_j(k,\omega). \tag{2.62}$$

This not only facilitates plotting the electronic structure but also generalizes the band dispersion concept to a generic Green's function formalism.

2.3.2 Angle Resolved Photoemission Spectroscopy

One of the powerful techniques to measure the electronic structure is angle resolved photoemission spectroscopy (ARPES) [25]. The standard ARPES experimental setup is shown in Fig. 2.5. By changing the incident photon, experimentalists can use the measured kinetic energy (E_{kin}) and escape angle (θ,ϕ) of the emitted electron to infer the energy and in-plane momentum of the underlying electronic state. By tracking the angular distribution of the measured intensity, the momentum dependent density of states can be reconstructed, too.

We will briefly review the simplest model in ARPES and discuss its connection to theoretical spectral functions. From the 3-step model [25], the whole emission process is assumed to take place in three steps: (1) The bulk electron is excited from an initial state to a higher-energy final state. (2) The excited electron travels from the bulk interior to its surface. (3) The electron tunnels through the surface barrier and escapes toward the detector. Step (2) basically induces the inelastic scattering and certain surface sensitivity leading to a continuous background signal. Step (3) describes the energy barrier to tunnel and can be empirically approximated by the material work function ϕ_{work}. In this simplified 3-step model, the electron dynamics and many-body effect

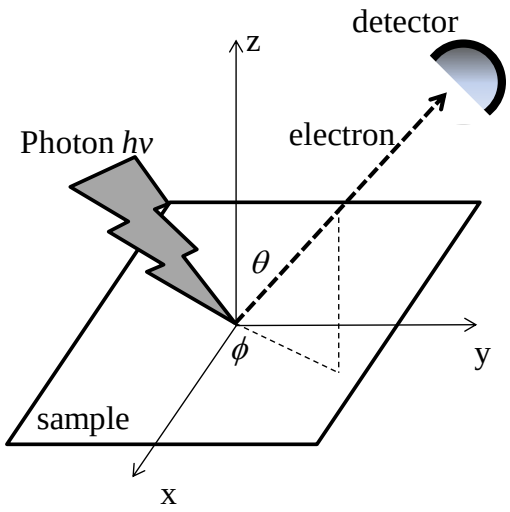

Figure 2.5: Standard ARPES setup

are mostly included in the Step (1), which we would focus on in the following discussion.

From the kinematic consideration, the detected electron has the binding energy $|E_B^k|$ for its original electronic state in the materials, which can be inferred from

$$|E_B^k| = E_{kin} - (h\nu - \phi_{work}), \tag{2.63}$$

where ν and E_{kin} are the controllable incident photon frequency and the kinetic energy measured at the detector respectively. Also, ϕ_{work} is the material-dependent work function and is determined before the ARPES measurement. In addition, the momentum component parallel to the sample surface is conserved and the photon momentum $h\nu/c \ll 1$ (c is the speed of light) can be ignored in a usual ARPES setup ($h\nu < 100$ eV). Then the in-plane electron momentum can be represented as

$$(k_x, k_y) = (\frac{1}{\hbar}\sqrt{2mE_{kin}}\sin\theta\cos\phi, \frac{1}{\hbar}\sqrt{2mE_{kin}}\sin\theta\sin\phi). \tag{2.64}$$

Hence, the ARPES data would be collected as $I(k_x, k_y, |E_B^k|)$ to represent the momentum- and energy-dependence of the electronic states in the solids.

From the dynamic consideration, the scattering between photon and emitted electron can be approximated by the Fermi Golden rule by perturbation.

The probability of the events is

$$w_{fi} = \frac{2\pi}{\hbar}|\langle\Psi_f^N|H_{int}|\Psi_i^N\rangle|^2\delta(E_f^N - E_i^N - h\nu), \tag{2.65}$$

where E_i^N (E_f^N) and Ψ_i^N (Ψ_f^N) are the initial (final) many-body energy and wavefunction of the N-electron system respectively. Thus, the measured ARPES intensity will be proportional to the summation of w_{fi} over all possible initial and final states with the thermodynamic weight $e^{-(E_i^N-\mu N)/k_BT}$ at temperature T.

$$I(k_x, k_y) \propto \sum_{if} e^{-(E_i^N-\mu N)/k_BT}|\langle\Psi_f^N|H_{int}|\Psi_i^N\rangle|^2\delta(E_f^N - E_i^N - h\nu). \tag{2.66}$$

Next, we consider the H_{int} from the interaction between the vector potential A and the electron:

$$H_{int} = \frac{e}{2mc}(A \cdot p + p \cdot A), \tag{2.67}$$

where the much smaller A^2 term has been neglected. If we further assume that the vector potential is slowly varying within the atomic scale so $\nabla \cdot A = 0$, which is so-called *dipole approximation* in the classical electrodynamics, then,

$$H_{int} \approx \frac{e}{mc}(A \cdot p). \tag{2.68}$$

To evaluate $\langle\Psi_f^N|H_{int}|\Psi_i^N\rangle$, we need to make the *sudden approximation*, which has been extensively used in the computing various photoemission spectra. We assume that the photon impacts on the electron in very short time. The influenced electron is quickly excited to final state and then moves toward the detector. The ejected electron does not have chance to scatter with the remaining $(N-1)$-electron many-body complex. This is justified by the fact that the energy transfer from the incident photon is usually very high ($h\nu \sim 10$ eV). Hence the final state can be treated as $|\Psi_f^N\rangle = |\phi_f^k\rangle \otimes |\Psi_m^{N-1}\rangle$, where $|\Psi_m^{N-1}\rangle$ denotes any eigenfunctions in the $(N-1)$ sector with energy E_m^{N-1}. For the initial state, we also approximate $|\Psi_i^N\rangle = |\phi_i^k\rangle \otimes |\Psi_{m'}^{N-1}\rangle$, where

$|\Psi_{m'}^{N-1}\rangle$ also refers to the excited states.

$$\langle\Psi_f^N|H_{int}|\Psi_i^N\rangle \simeq \langle\phi_f^k|H_{int}|\phi_i^k\rangle\langle\Psi_m^{N-1}|\Psi_{m'}^{N-1}\rangle. \tag{2.69}$$

The two states $|\phi_i^k\rangle$ and $|\Psi_{m'}^{N-1}\rangle$ should be interpreted as $c_{kj}^\dagger|vacuum\rangle$ and $c_{kj}|\Psi_i^N\rangle$, where c_{kj} represents the $|kj\rangle$ state in the electronic band. The photoemission intensity along specific momentum direction k is proportional to

$$\sum_j |M_{f,j}(k)|^2\big[\sum_{im} e^{-(E_i^N-\mu N)/k_BT)}|\langle\Psi_m^{N-1}|c_{kj}|\Psi_i^N\rangle|^2\delta(E_f^N - E_i^N - h\nu)\big], \tag{2.70}$$

where $M_{f,j}(k) \equiv \frac{e}{mc}\langle\phi_f^k|A\cdot p|kj\rangle = \frac{-i\hbar e}{mc}\int dr\phi_f^*(x)A\cdot\nabla_r\psi_{kj}(r)$. It is noted that $E_f^N = E_m^{N-1} + E_{kin}$. The summation over i and m of Eq. 2.70 can be proportional to the $f(E_{kin}-h\nu)A_j(k, E_{kin}-h\nu)$ describing the occupied states below the Fermi energy, where $f(\omega) = \frac{1}{e^{(\hbar\omega-\mu)/k_BT}+1}$ is the Fermi Dirac distribution. Hence, the ARPES intensity can be written as

$$I(k,\omega) \propto \sum_j |M_{f,j}(k)|^2 f(\omega)A_j(k,\omega), \tag{2.71}$$

By the probed intensity associated with $A_j(k,\omega)$, ARPES is capable of detecting the momentum-resolved density of states and the many-body self-energy of the renormalized Green's function. In single-orbital systems, such as cuprates, the dipole matrix $M_{f,j}(k)$ depends on the photon energy, sample orientation, and photon polarization setup. In the multi-atomic and multi-orbital system, the information in the dipole matrix becomes richer and includes the structure factor depending on the specific the atomic arrangement.

2.3.3 Band Structure Unfolding with One-particle Spectral Functions

We have seen the power of the Bloch theorem to help formulate the eigenstates of electrons in periodic system. However, the strategy to represent the electronic structure in terms of energy eigenvalues may lead to some ambiguity and problems. The first issue is that the choice of unit is seemingly arbitrary. Besides the minimal periodicity, one can always enlarge the unit cell to obtain the dispersion in the reduced BZ. An one-dimensional simple tight-binding toy

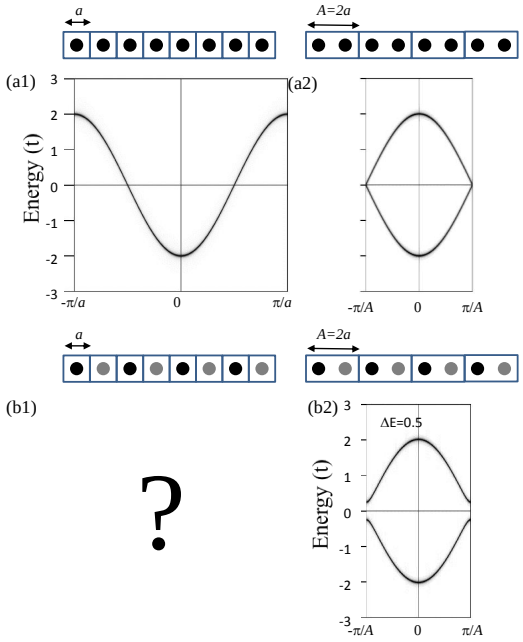

Figure 2.6: One-dimensional toy model with nearest neighbor hopping t. The band structures with (a1) one-atom unit cell and (a2) two-atom unit cell. (b1) Unknown representation of the electronic structure in one-atom per unit cell basis with CDW. (b2) Band structure in two-atom unit cell basis with CDW.

model is provided in Fig. 2.6(a1) with its regular dispersion below. There is freedom to deliberately double the unit cell to be (a2). Then, the resulting dispersion is influenced by non-physical band folding and may give the impression of the existence of some artificial states. For example, the higher state at the Γ point in (a2) is definitely absent in (a1). This arbitrary band folding can become more problematic if we keep increasing the unit cell size. Eventually, only one Γ point is left in a extremely tiny BZ and has atomic-like energy levels without any meaningful *dispersion*. In this artificial case, we learn that the dispersion becomes less and less informative with an increasing unit cell size because the essential information has been hidden in the eigenfunction of the enlarged unit cell.

One may think that the above example is totaly arbitrary but the situation of physically enlarged unit cell is very common in materials. When the system is subject to some emergent ordering and forced to accept the enlarged unit cell. For example, this frequently happens when an antiferromagnetic Neel state or a charge/spin density wave is present. We give an example when the

	normal cell	supercell
primitive vector	a_1, a_2, a_3	A_1, A_2, A_3
lattice vector	r	R
reciprocal primitive vectors	b_1, b_2, b_3	B_1, B_2, B_3
number of unit cells	l	L
crystal momentum	k	K
Wannier orbital index	n	N
Wannier orbital	$\|rn\rangle$	$\|RN\rangle$
Fourier transform of Wannier orbital	$\|kn\rangle$	$\|KN\rangle$
band index	j	J
Hamiltonian eigenenergy	ε_{kj}	ε_{KJ}
Bloch state	$\|kj\rangle$	$\|KJ\rangle$

Table 2.1: Notation for normal and super cells.

charge is spontaneously re-distributed as in lower two panels in Fig. 2.6 because the black atoms have lowered on-site energy and more charges than the grey ones. The on-site energy difference is assumed to be ΔE. Thus, we can no longer pursue the band dispersion in the one-atom per unit cell basis as in Fig. 2.6(b1). The conventional wisdom is to double the unit cell and calculate the band structure in the small Brillouin zones as in Fig. 2.6(b2). Nonetheless, the comparison between CDW-free Fig. 2.6(a1) and CDW Fig. 2.6(b2) is not very intuitive. On the other hand, as the on-site energy difference $\Delta E \longrightarrow 0$, the dispersion should smoothly recover Fig. 2.6(a1). However, the linkage seems to be missing in the current framework due to the choice of unit cell. Therefore, the representation of the electronic structure in the original BZ as in Fig. 2.6(b1) is highly desired to clarify issues.

Instead of using eigen momentums and energies to represent a band structure, it is more general to describe an electronic structure by one-particle spectral functions. [1] In an eigenbasis, a retarded Green's function, which is equivalent to Eq. 2.59, can be written as

$$G^R_{JJ'}(K, K', \omega) = \langle KJ|\frac{1}{\omega - H + i\eta}|K'J'\rangle = \frac{\langle KJ|K'J'\rangle}{\omega - \varepsilon_{KJ} + i\eta} = \frac{\delta_{K,K'}\delta_{J,J'}}{\omega - \varepsilon_{KJ} + i\eta}. \tag{2.72}$$

Thus, the one-particle spectral function is defined as the imaginary part of the

[1] For the notation in the unfolding method, we reserve all capital and little letters for the normal (original) cell and super (enlarged) cell respectively. They are summarized in Table 2.1.

diagonal matrix element of the Green's function with $-\frac{1}{\pi}$ as the conventional factor:

$$A_J(K,\omega) \equiv -\frac{1}{\pi}\mathrm{Im}G^R_{JJ}(K,K,\omega) = \frac{1}{\pi}\frac{\eta}{(\omega-\varepsilon_{KJ})^2+\eta^2} \tag{2.73}$$

It is also customarily to represent the spectral function in the orbital-resolved manner of the Wannier basis as

$$A_N(K,\omega) = -\frac{1}{\pi}\mathrm{Im}G^R_{NN'}(K,K,\omega) = \sum_J \frac{|\langle KJ|KN\rangle|^2\eta}{(\omega-\varepsilon_{KJ})^2+\eta^2}. \tag{2.74}$$

By using the Wannier basis, it is made easy to represent the spectral function in the unfolded BZ basis [26]. We can define the Fourier transform of the momentum in the original BZ as $|kn\rangle = \frac{1}{\sqrt{l}}\sum_r e^{ikr}|rn\rangle$. To look for the electronic structure in Fig. 2.6(b1), we only keep the diagonal term of the Green's function:

$$\begin{aligned} G^R_{nn}(k,k,\omega) &= \langle kn|\frac{1}{\omega-H+i\eta}|k'n'\rangle \\ &= \sum_{KK'JJ'}\langle kn|KJ\rangle\langle KJ|\frac{1}{\omega-H+i\eta}|K'J'\rangle\langle K'J'|k'n'\rangle \\ &= \sum_{KJ}|\langle kn|KJ\rangle|^2\frac{1}{\omega-\varepsilon_{KJ}+i\eta} \end{aligned} \tag{2.75}$$

Therefore, the spectral function becomes

$$A_n(k,\omega) = -\frac{1}{\pi}\mathrm{Im}G^R_{nn}(k,k,\omega) = \sum_{KJ}|\langle kn|KJ\rangle|^2 A_J(K,\omega). \tag{2.76}$$

It means that we can obtain the unfolded band structure $A_n(k,\omega)$ by combining the KS orbital information in $A_J(K,\omega)$ and the extra matrix element $\langle kn|KJ\rangle$.

The evaluation of $\langle kn|KJ\rangle$ requires the expansion to the real space Wannier function and the orthogonality between $|KN\rangle$ and $|kn\rangle$. First,

$$\begin{aligned} |KJ\rangle &= \sum_{RN}|RN\rangle\langle RN|KN\rangle\langle KN|KJ\rangle \\ &= \frac{1}{\sqrt{L}}\sum_{RN}e^{-iKR}|RN\rangle\langle KN|KJ\rangle \end{aligned} \tag{2.77}$$

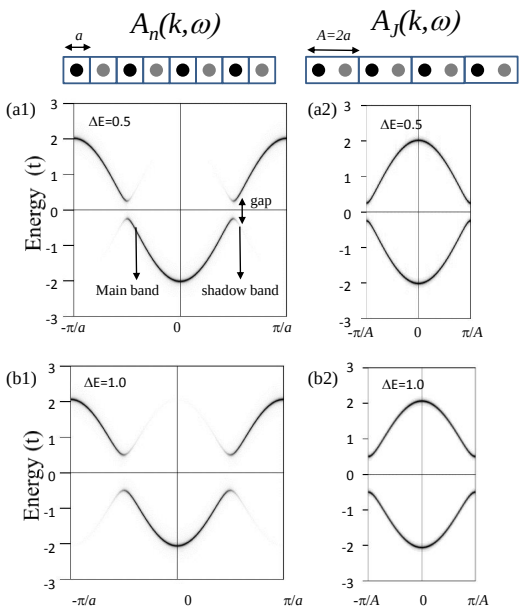

Figure 2.7: (a1) Unfolded and (a2) Folded spectral function with $\Delta E = 0.5$. (b1) Unfolded and (b2) Folded spectral function with $\Delta E = 1.0$

Then, we insert $\sum_{rn} |rn\rangle\langle rn| = 1$ and replace $|KJ\rangle$ by Eq. 2.77 to obtain

$$\begin{aligned} \langle kn|KJ\rangle &= \frac{1}{\sqrt{L}} \sum_{RNr} e^{-iKR} \langle kn|rn\rangle\langle rn|RN\rangle\langle KN|KJ\rangle \\ &= \frac{1}{\sqrt{Ll}} \sum_{RNr} e^{-iKR+ikr} \langle rn|RN\rangle\langle KN|KJ\rangle \end{aligned} \tag{2.78}$$

The matrix element $\langle rn|RN\rangle$ is non-zero only when N and n label the same orbital. It also requires that $r = R+\tau$, where τ refers to the location of orbital N inside the larger super cell. Then,

$$\langle kn|KJ\rangle = \sqrt{\frac{l}{L}} \sum_{\tau} e^{ik\tau} \delta_{k,K+G} \delta_{nN} \langle KN|KJ\rangle \tag{2.79}$$

It is noted that k and K are related to each other by a reciprocal lattice vector G of the super cell. Besides, the phase $e^{ik\tau}$ gives rise to certain cancelation in $A_n(k,\omega)$ so the total weight on the quasiparticle poles is not strictly unity. This is the greatest contrast to the representation of $A_J(K,\omega)$.

Follow the formulae 2.76 and 2.79, it is easy to convert the band structure

in the super cell BZ to its normal cell representation. Let us apply this unfolding method to the one-dimensional CDW toy model in Fig. 2.7 with different ΔE. As ΔE increases from 0.5 in the upper row to 1.0 in the lower row, two features of translational symmetry breaking become prominent. The CDW gap size increases, and the shadow bands becomes more evident. Both are characteristic of the coupling between the CDW order parameter and the electronic structure. In addition, it is now natural to think that from Fig. 2.7(a1) one can smoothly recover Fig. 2.6(a1) as ΔE approaches zero. Therefore, the band structure unfolding method largely facilitates the investigation of electronic structure under translational symmetry breaking.

This unfolding method can also be applied to decode the ARPES measurement. In the standard procedure, the ARPES intensity is compared with the first-principles band structure, which is always performed with the crystal unit cell of the materials. In the presence of broken translation induced by ordering, $A_J(K,\omega)$ becomes less informative and subject to a rather complex dipole matrix element $\langle\phi_f^k|p|KJ\rangle$ where the structure form factor is hidden. Following the thinking of the band structure unfolding, we can re-write the ARPES intensity as

$$\begin{aligned} I(k=K,\omega) &\propto \sum_J |A\cdot\langle\phi_f^k|p|KJ\rangle|^2 f(\omega)A_J(K,\omega) \\ &\approx \sum_{Jkn} |A\cdot\langle\phi_f^k|p|kn\rangle|^2|\langle kn|KJ\rangle|^2 f(\omega)A_J(K,\omega) \\ &= \sum_n |A\cdot\langle\phi_f^k|p|kn\rangle|^2 f(\omega)A_n(k,\omega), \end{aligned} \tag{2.80}$$

The second line is approximated by ignoring those non-square terms, which we assume their complex values would lead to destructive cancelation in the summation. In the unfolded one-particle spectral function, the corresponding dipole matrix $\langle\phi_f^k|p|kn\rangle$ becomes smooth in the reciprocal space because the $|kn\rangle$ contains no inter-atomic interference. Therefore, $A_n(k,\omega)$ provides a better and more physical interpretation for the physical observable measurements than the $A_J(K,\omega)$ from standard DFT calculation.

From both theoretical and experimental considerations, we find that the first-principles band structure formalism can provide a suitable tool to study the influence on the electronic structure from the translational symmetry

breaking. In the following parts of this thesis, I will apply it extensively to different realistic materials and reveal the unusual phenomena induced by such a broken symmetry.

Chapter 3

Case 1: Lifshitz Transition and Superconductivity Enhancement in High Pressure *cI*16 Li

The work presented in this chapter has been submitted for publication and is available as a preprint [27].

The Lifshitz transition refers to a change on Fermi surface topology. Its occurrence usually results from pressure variation or doping charge to materials. Both effects not only shift chemical potential but also alter electron structure to some extent. By changing external parameters, Fermi surfaces may smoothly change from a open shape to closed surfaces, for example the neck disruption in Fig. 3.1(a). This means that a critical energy E_c with a singular energy isosurface of a conical shape (see middle panel of Fig. 3.1(a)) is close to the Fermi energy. Shifting chemical potential may change Fermi surface from the left to the right in Fig. 3.1(a) or *vice versa*. The other type of the Lifshitz transition corresponds to the disappearance or appearance of a pockets as shown in Fig. 3.1(b). Thus, E_c is defined by an energy value at which a Fermi pocket shrinks into a single point as shown in the middle panel in Fig. 3.1(a). In Ref. [28], it was shown that an anomalous part of density of states $\delta g(E)$ results from the occurrence of the Lifshitz transition. We summarize the four situations related to the Lifshitz transition and the square root behavior, which $\delta g(E)$ is proportional to, in Fig. 3.2. Because of this $\delta g(E)$, all thermodynamic properties will be also affected in a peculiar manner [28].

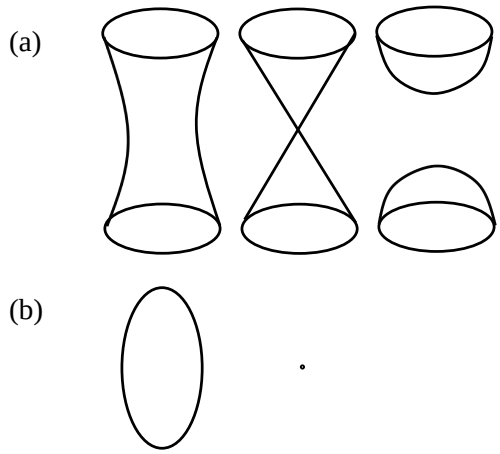

Figure 3.1: Schematic diagrams of the Lifshitz transition. (a) Occurrence of neck disruption and (b) disappearance of the pocket. Lifshitz transition also includes the transition happening in the reverse way, namely neck reconstruction and appearance of the pocket.

In this study, we will discuss its implications to superconductivity in Li at high pressures from the first-principles method.

3.1 Introduction

In 2007, almost one century after Onnes' first discovery of superconductivity [29], Li eventually joined ambient-pressure superconductors with a critical temperature (T_c) down to 0.4 mK [30]. Its high-pressure T_c up to 16 K surprisingly tops all elements at similar pressures. Being an elemental conventional superconductor with a rich phase diagram (c.f. Ref. [31] and Fig. 1), Li is a natural touchstone for first-principles methods of determining T_c. Certain breakthroughs have been established in the frameworks of Eliashberg theory [32–39] and superconducting density functional theory [40, 41] to satisfactory agreement with the experimental trend in the correct order of magnitude. Such phonon-mediated superconductivity can be strongly tied with lattice instabilities. For both ends of the collected data in Fig. 3.3, the disappearance of superconductivity at 20 and 62 GPa can undoubtedly be attributed to the occurrence of structural transitions. At the unusual T_c maximum around 30 GPa a substantial phonon softening maximizes the electron-phonon coupling [38] and causes a transition to the $cI16$ structure. Nonetheless, it remains

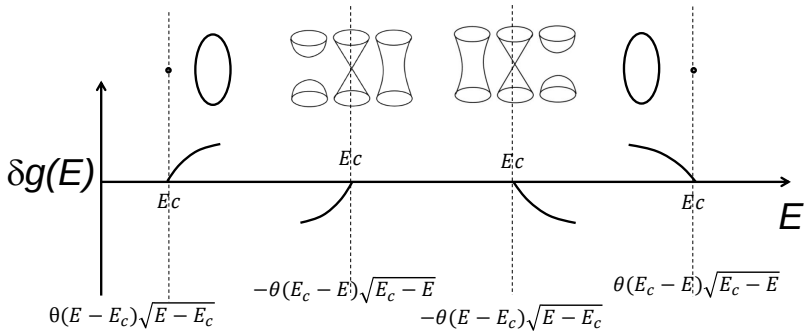

Figure 3.2: Schematic diagrams of the anomalous part in density of states from the Lifshitz transition. The term $\delta g(E)$ has a square root dependence on energy. The value of E_c refers to the energy the singular energy isosurface appears as the middle panel of (a) or (b).

puzzling that the T_c subsequently plunges into a minimum between 44 and 47 GPa in the absence of structural and electronic transitions or singular phonon behavior [37].

A peculiar change in the electronic structure is believed to account for this anomalous pressure, below which the superconductivity is dominantly controlled by the fermiology [1]. Between 20 and 30 GPa the superconductivity is enhanced by accumulating FS nesting in the fcc side [35, 38], reaching a 16 K maximum. In the subsequent $cI16$ phase, T_c decreases due to a monotonic FS depletion [37]. The depletion mainly comes form the nature of the $cI16$ charge density wave (CDW), which consists of a distortion along the cube diagonal within its unit cell composed of $2 \times 2 \times 2$ regular body-centered cubic cells (see right panels in Fig. 3.3). Above the anomalous pressure the FS depletion persists [37] opposite to the T_c growth in the experiment. Consequently the major influence on superconductivity is taken over by another effect that is insensitive to the fermiology. Its impact on the T_c (tentatively assumed to be smooth) is depicted by the red curve in Fig. 3.3. The anomaly can be regarded as an onset pressure, below which the fermiology resumes dominance and promptly increases T_c. Therefore, the elaboration on the FS evolution around the pressure anomaly is highly demanded for resolving the missing puzzle piece in the phase diagram.

[1] Fermiology in this context refers to the configuration, such as the shape and the size, of a Fermi surface.

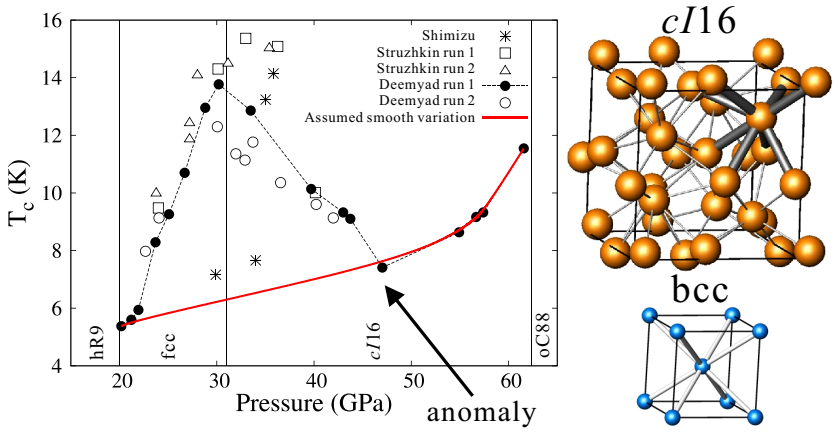

Figure 3.3: (Left) Experimental phase diagram of Li with the vertical structural transition lines from Refs. [31, 42–45]. The superconducting T_c values are from Shimzu [42], Struhkin run 1&2 [43], and Deemyad run 1&2 [44]. The assumed smooth variation (solid red curve) is simulated by the basis spline method on the lowest two and highest five pressure data points. (Right) Conventional $cI16$ (top) and bcc (bottom) unit cells.

In this study, we identify the occurrence of a Lifshitz transition (LT) in high-pressure $cI16$ Li from first-principles. Our unfolded Fermi surface shows that when the pressure is lowered across the anomalous point at ∼43 GPa, there appears new FS pockets. This gives rise to a non-analytic superconductivity enhancement, which we verify numerically and find to be in quantitative agreement with experimental observations. Our results also visually decode the effects of three-dimensional charge density waves on the Fermi surface. We find the $cI16$ nesting vectors $[200]\frac{2\pi}{a_{cI16}}$ and $[110]\frac{2\pi}{a_{cI16}}$ to be as relevant as the previously reported $[211]\frac{2\pi}{a_{cI16}}$ [46]. These intriguing and direct observations demonstrate the general value of Fermi surface unfolding in the study of topological features associated with symmetry breaking phase transitions in materials.

3.2 Method

A commonly encountered difficulty in the study of Fermiology of large unit cell systems is the hindrance from severe band folding. For example we illustrate with a two-dimensional toy model the complexity of FS folding that arises from

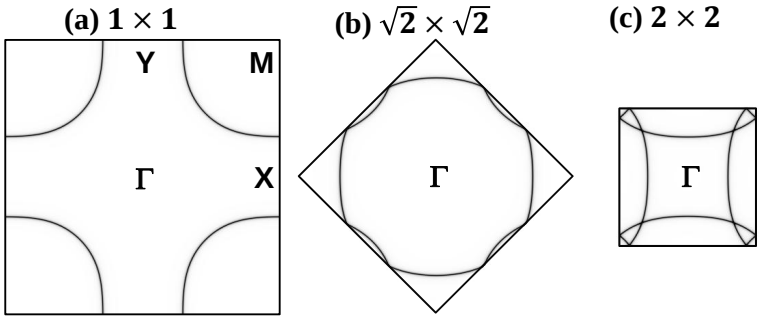

Figure 3.4: Illustration of Fermi surface folding issue. (a) Fermi surface of half-filling two-dimensional one-band tight-binding model with hopping integrals $t'/t = -0.25$ and $t''/t = 0.125$. (b) the same model solved with a $\sqrt{2} \times \sqrt{2}$ supercells. (c) the same model solved with a 2×2 supercells. Recovery from (b)&(c) to (a) can be achieved by FS unfolding.

the arbitrary choice of lattice periodicity even in the absence of any physical broken symmetry. This reflects the fact that Bloch wavefunctions take more information out of the folded FS as the supercell size grows. This difficulty can be overcome by the recently developed unfolding method [47], which is aimed to restore the informative Green's function in a normal cell basis. Thus the one-particle spectral function in the eigenstates basis, $A_{KJ,KJ}(\omega)$, can be converted into a reference basis $A(k,\omega) = \sum_{KJn} |\langle kn|KJ\rangle|^2 A_{KJ,KJ}(\omega)$. Here, K/k is the crystal momentum of the original/reference system, J the eigenstate band index, and n the Wannier orbital index. With the use of Wannier functions the spectral weight magnitude $|\langle kn|KJ\rangle|^2$ reduces to a simple structure factor that is readily evaluated. [47]

Specifically in $cI16$ Li, the unfolding method allows to reveal detailed information of the Fermi surface topology. Density functional theory calculations are performed with the WIEN2K [12] implementation of the full potential linearized augmented plane wave method in the local density approximation. Then, the symmetry-respecting Wannier functions [48] of Li s and p orbitals are constructed within Hilbert space between -5 to 30 eV. The lattice constant a_{cI16} and atomic displacement x (≈ 0.05 and increasing with pressure) away from the bcc structure are obtained from the experimental values [45]. Then, to obtain the unfolded electronic structure in $cI16$ Li, the natural choice for the reference basis is the bcc lattice as shown in the right of Fig. 3.3. In this study, we use opacity in the three-dimensional reciprocal space to depict the

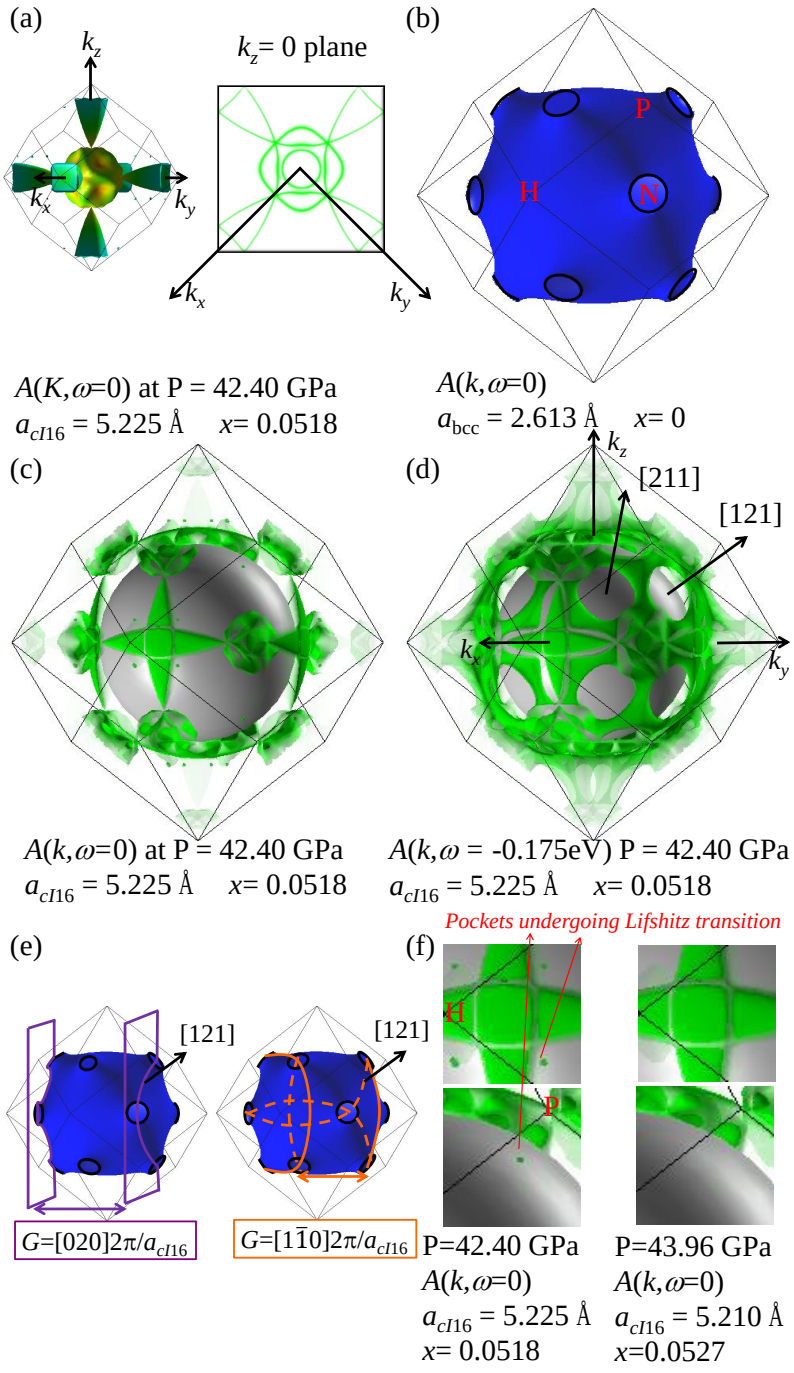

Figure 3.5: Fermi surfaces of (a) $cI16$ Li at 42.40 GPa and (b) its reference CDW-free bcc Li. (c) Unfolded $cI16$ Fermi surface and (d) energy isosurface at -0.175 eV. The opacity at each k point represents the spectral weight with the most/least transparent spots corresponding to 0.02/0.88. For the purpose of clarity, the grey balls in (c-d) are utilized to block image from the back side. (e) Fermi surface intersections with the nesting planes spanned by $[020]\frac{2\pi}{a_{cI16}}$ (left) and $[1\bar{1}0]\frac{2\pi}{a_{cI16}}$ (right). (f) Enlargements showing pocket appearance (i.e. Lifshitz transition).

spectral weight magnitude on the unfolded FS and energy isosurfaces.

3.3 Unfolded Fermi Surfaces

The $cI16$ FS in Fig. 3.5(a, left) gives a good example of an overwhelmingly folded FS in the $cI16$ Brillouin zone (BZ) which is eight times smaller than that of the bcc lattice. An additional complication of folding in three dimensions (compared to lower dimensions) is that when FS sheets are intertwined, they block each other. The cross sectional view on the $k_z = 0$ plane in the right of Fig. 3.5(a) shows that the outer FS sheet is blocking two inner FS sheets. In contrast, the unfolded FS in Fig. 3.5(c) recovers the resemblance to Fig. 3.5(b), the FS of the fictitious CDW-free bcc system with $a_{\rm bcc} = a_{cI16}/2$. For example the necks at the high symmetry points N resembling the FS of copper [35, 46] are still clearly recognizable in the unfolded FS. The grey balls in Fig. 3.5(c)(d)(f) are used to block the image from the back side for the better visualization and do not containing any visible weight inside.

The effect of the CDW is clearly demonstrated in Fig. 3.5(c). The comparison between Fig. 3.5(b) and (c) shows that the CDW-induced gaps substantially deplete the DOS around the Fermi energy for energy gain. Moreover these gaps offer the opportunity to change the FS topology. In the bcc reference basis, the CDW couples each k point to eight $k+G$ points by the potential $V^G_{\rm CDW}$, where G represents the eight reciprocal lattice vectors of $cI16$ unit cell that lie in the bcc BZ. In the presence of substantial hybridization, spectral weight is re-distributed between the eight coupled k points and appears as transparent sheets of Fermi surface. The opacity of these sheets reflects the strength of $V^G_{\rm CDW}$. Therefore, the unfolded FS provides a systematic way to detail its coupling with the order parameter of the broken translational symmetry.

Due to the serious FS depletion, the identification of the relevant CDW wave vector G's is made easier if we focus on the unfolded energy isosurface of 0.175 eV below the Fermi energy in Fig. 3(d). The effects of $V^G_{\rm CDW}$ can be understood from considering the intersections of the nesting planes $\pm\frac{1}{2}G$ with the FS of the fictitious CDW-free bcc system as shown in Fig. 3.5(e). The Bloch states at these intersections are degenerate and therefore will be

gapped out most strongly. For example, the left of Fig. 3.5(e) shows the degenerate Bloch states that are nested by $[020]\frac{2\pi}{a_{cI16}}$ (representing the $G's$ symmetry-related to $[200]\frac{2\pi}{a_{cI16}}$) and explains the cut traces connecting any two neighboring N points in Fig. 3.5(d). Another CDW component is illustrated by the pair of solid/dashed orange planes spanned by $G = [1\bar{1}0]\frac{2\pi}{a_{cI16}}$ (representing the $G's$ symmetry-related to $[110]\ \frac{2\pi}{a_{cI16}}$) in the right of Fig. 3.5(e). If we collect multiple symmetry-related cut marks, $V_{\mathrm{CDW}}^{[110]}$ is concluded to be responsible for the *cross-like* mark on every H point in Fig. 3(d).

The most prominent FS depletion takes place on the 24 large holes along the [211] direction had been previously been assigned to the $G = [211]\frac{2\pi}{a_{cI16}}$ nesting vector [46]. Indeed V_{CDW}^{211} partially contributes to those substantial gaps. However, both V_{CDW}^{200} and V_{CDW}^{110} also conspire to cause DOS depletion because their cut marks pass those holes too, as exemplified with the arrows in the [121] direction in Fig. 3.5(e). Contrary to low-dimensional physics, the FS nesting importance is diluted by the consideration of the phase space, which takes into account all relevant V_{CDW}^{G}'s. Fig. 3(d) indicates that the phase space affected by V_{CDW}^{200} and V_{CDW}^{110} is at least comparable with the previously emphasized V_{CDW}^{211}, and so is the energy gain.

3.4 Lifshitz Transition and Superconductivity

Next we investigate the FS evolution of $cI16$ Li near the anomalous pressure in the phase diagram shown in Fig. 3.3. Interestingly, we find the emergence of new FS pockets around the N and P at the pressure between 42.40 and 43.96 GPa in Fig. 3.5(f). This topological change of FS is termed Lifshitz transition [28]. Although they are seemingly small pockets, the LT is known to cause a dramatic change in physical observables within a small pressure window [49]. It also has been proven to induce non-analytic behavior on the Fermi surface density of states (DOS) [28] and conventional superconductivity [49, 50]. Recently, LTs have been applied to engineer the topological order in topological insulators $Bi_{1-x}Sb_x$ [51]. Also, doping-induced LTs have been proposed to explain the diverging cyclotron mass in high T_c cuprates [52] and the vanishing transport anisotropy in the novel Fe-based superconductors [53].

The LT in $cI16$ Li gives rise to an anomalous contribution in the DOS,

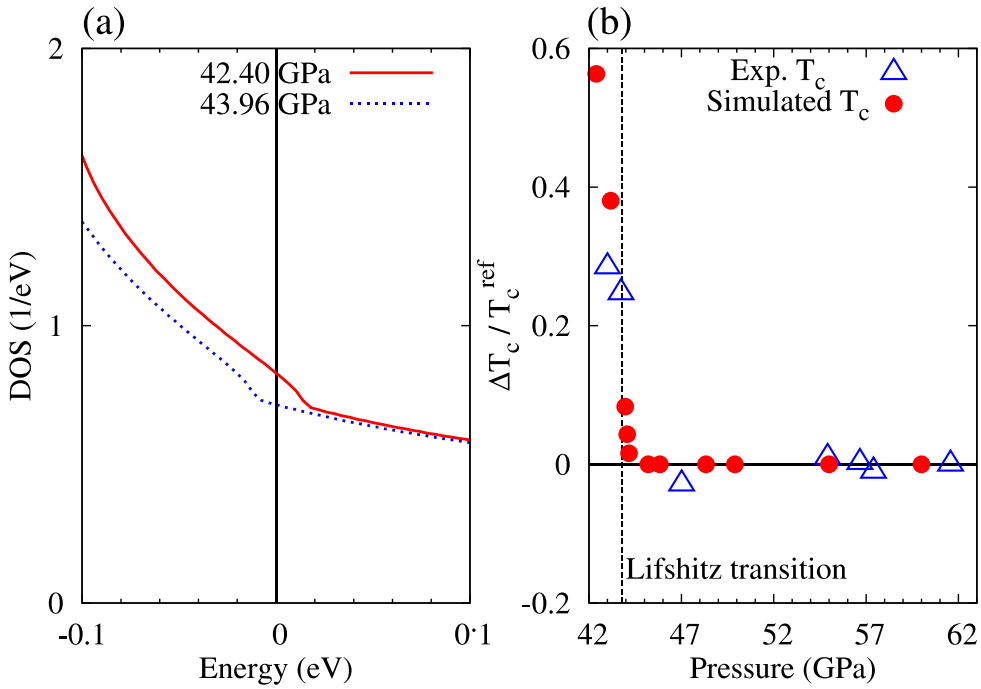

Figure 3.6: (a) DOS at 42.40 and 43.96 GPa. (b) Experimental [44] and simulated $\Delta T_c/T_c^{ref}$ versus pressure for $cI16$ Li.

$\delta g(\omega) \propto \sqrt{E_c - \omega}$ as $\omega \to E_c$ [28], originating from the extra pockets. Here the pressure-dependent E_c is the critical energy at which the pockets disappear. The result in Fig. 3.6(a) not only confirms the correct square root behavior but also is consistent with the observation in Fig. 3.5(f) that the Fermi energy E_F is located above (below) E_c at 43.96 (42.40) GPa. It is important to stress that the occurrence of the LT is confined to an infinitesimally small part of the k space. Therefore to capture the singular behavior of the DOS numerically a $400 \times 400 \times 400$ k mesh has been employed. Such an extremely fine k-mesh is only possible by the use of Wannier interpolation and is otherwise inaccessible in standard first-principles calculations.

In absence of any symmetry breaking, this LT is the natural explanation of the anomalous onset (between 44 and 47 GPa) toward lower pressures. Below this pressure the T_c displays a sharp upturn followed by a continuous enhancement (c.f. Fig. 3.3) due to the extra available DOS at the Fermi energy. Makarov and Baryakhtar have shown that in the weak coupling Bardeen-Cooper-Schrieffer (BCS) theory the anomalous part of the DOS, $\delta g(\omega)$, leads

to an asymmetric variation of the T_c. [50] This physical picture can be applied to $cI16$ Li. At pressures as high as 60 GPa, E_c is far below E_F and has absolutely no effect on superconductivity. But at a critical pressure above the LT, E_F will fall right below $E_c+\omega_D$ with ω_D the Debye frequency. At this pressure T_c will suddenly start to surge because the extra DOS $\delta g(\omega)$ impacts the T_c exponentially. As the pressure is further lowered, the small pockets grow and contribute to the T_c enhancement in a continuous manner.

The physical picture described above can be formulated into a quantitative agreement in the superconductivity enhancement between the experimental data and our simulation. For the purpose of demonstration, we tentatively separate the $\delta g(\omega)$ correction on the superconductivity as ΔT_c from the other smooth pressure-dependent part T_c^{ref}. For the experimental part the smoothly varying T_c^{ref} is attributed to the solid red curve in Fig. 3.3, and ΔT_c is defined as its difference from the total T_c. For the theoretical part we can simulate T_c and T_c^{ref} by numerically solving the BCS gap equation with and without the non-analytic contribution $\delta g(\omega)$ respectively and obtain ΔT_c as their difference. In order to simulate the DOS in more pressure conditions, the lattice constant and atomic displacement are refined by linear fitting with respect to the experimental pressures in Ref. [45]. The effective pairing potential V_{ee} in the gap equation ($1 = V_{ee}\sum_{\omega=E_F-\omega_D}^{E_F+\omega_D}\frac{g(\omega)}{2\omega}\tanh\frac{\omega}{2T_c}$) is fixed to be 345 meV to obtain $T_c \sim 9$ K at the LT. The Debye frequency $\omega_D = 21.5$ meV is chosen to match the characteristic phonon frequency in Ref. [37]. The resulting $\Delta T_c/T_c^{ref}$ ratio demonstrates excellent agreement in Fig. 3.6(b) as the sudden rise right below the LT pressure is well matched. Therefore, the puzzling strong enhancement of superconductivity below the anomalous pressure can now be understood as a consequence of the LT.

3.5 Conclusion

In summary, we identify a Lifshitz transition at ∼43 GPa in $cI16$ Li to be responsible for the experimentally observed onset pressure, below which the superconductivity is highly enhanced. This is achieved via the unfolding method, which significantly facilitates the Fermi surface visualization. The implementation of three-dimensional Fermi surface unfolding shows the capability to

decode the Fermi surface topology of $cI16$ Li. Furthermore it allows to identify V_{CDW}^{200} and V_{CDW}^{110} in addition to the previously reported V_{CDW}^{211} as the important CDW components that stabilize $cI16$ Li. The three-dimensional unfolding of Fermi surfaces is expected to expedite a wide range of studies about topological evolution and structural stability of materials with broken translational symmetry in general.

Chapter 4

Case 2: Dirac Cones in Two-Dimensional Dispersion via Periodic Modulation of On-site Energy

The work presented in this chapter is part of the study in the preprint [54].

4.1 Introduction

Realization of a conically linear dispersion (termed Dirac cone as in Fig. 4.1(a)) has recently opened up exciting opportunities for high-performance devices that make use of the peculiar transport properties [55–60] of the massless carriers. A good example of current fashion is heavily studied graphene, a single atomic layered graphite. It not only offers a prototype of Dirac physics in the field of condensed matter [61], but also provides a playground of various exotic phenomena [62–66]. In the meantime, numerous routes have been attempted to search for the next "graphene" [51, 67–72]. Despite these efforts, to date there is still no simple guideline to predict and engineer such massless particles in materials.

In this study, we explain a generic feature of photoemission measurements in graphene by the first-principles unfolding method introduced in Chapter 2. Based on that, we formulate an alternative understanding of the formation of

Dirac cones. In this new perspective, the conical dispersion in graphene is a consequence of a translational symmetry breaking from a triangular lattice to a honeycomb lattice via ordered vacancies. The key to preserve the accidental degeneracy at Dirac points is a special potential derived from a on-site energy modulation. Under certain conditions, we show that this on-site energy modulation can lead to the existence of Dirac cones in a general two-dimensional dispersion. Two examples are given in a square lattice to exemplify the validity of this scenario and demonstrate additional flexibility to control the quantity as well as anisotropy of the resulting Dirac cones.

4.2 Dirac Cone in Graphene

Let us start from an interesting feature of graphene Dirac cones [73] in angle-resolved photoemission spectroscopy (ARPES) [74–76]. Figure 4.1(b) shows an representative ARPES observation. Intriguingly, the observed cone appears incomplete even though a standard theory would indicate a complete Dirac cone, for example given by the intense red bands in Fig. 4.1(d)[1]. This vanishing intensity is typically considered as the "matrix element effect" of the measurement, and indicates perfect destructive quantum mechanical interference [77] between the two carbon atoms in the unit cell of the honeycomb lattice shown in Fig. 4.1(c).

An alternative and more straightforward perspective is to consider the honeycomb lattice as a triangular lattice with periodic vacancies, as shown in Fig. 4.1(e). If we follow the unfolding method in Chapter 2, we can project one-particle spectral functions of graphene onto the eigenspace of a reference triangular lattice. Since there is only one (or sometimes zero) atom in this unit cell in Fig. 4.1(e), the remaining matrix element is just a simple atomic form factor. Because one-particle spectral function in this reference basis absorbs the interference between the two carbon atoms, the feature of vanishing intensity is thus explicitly incorporated in it. We use thickness and colors in

[1]To simulate quasi-two-dimensional properties of graphene of honeycomb lattice, a unit cell, containing two atoms, is chosen with 1.42 Å inter-carbon distance and 10 Å inter-layer distance vertically. This forms a crystal structure of P6/mmm space group. All input settings follow the default values as $R_{mt}K_{max} = 7$ and $l_{max} = 10$. The k point mesh of $21 \times 21 \times 4$ to reach convergent ground state density.

Fig. 4.1(f-h) to represent the magnitude and orbital characters of the spectral function. The resulting "unfolded" spectral function [47] with an "incomplete" Dirac cone of red p_z orbitals have vanishing spectral weight in the lower part of the cone along the $\overline{\mathrm{K_sM_n}}$ path and in the upper part along the $\overline{\Gamma\mathrm{K_s}}$ path. This is in agreement with the experimental ARPES observation.

On the other hand, the high-energy part ($\sim$5 eV lower or higher than the Fermi energy) in Fig. 4.1(e-f) is dominated by p_x and p_y orbitals in green. A significant amount of shadow bands indicate that ordered vacancies provide a strong translational symmetry breaking potential. For example, the shadow weight in the lowest band on the $\overline{\mathrm{M_nK_nK_s}}$ path appears as a clear weaker replica of the original band on the $\overline{\mathrm{M_s\Gamma K_s}}$. It is also noted that p_x are p_y orbitals are fully decoupled from p_z due to the mirror symmetry with respect to the graphene plane. Because we are more interested in low-energy physics and Dirac cones, we will only consider p_z orbitals in the following discussion.

This alternative "one-carbon" picture offers an interesting new way to understand the electronic structure of graphene, particularly the formation of the Dirac cones. Fig. 4.2 illustrates this with a reduced Hamiltonian, for clarity, that covers only carbon p_z orbitals that defines the relevant red band in Fig. 4.1. Starting with a triangular lattice with the same nearest inter-atomic hopping t as in graphene, the corresponding band structure consists of a simple dispersion [Fig. 4.2(a)] and an almost circular Fermi surface [Fig. 4.2(d)] when the orbital is half-filled. The resulting dispersion is

$$E_{tri}(k_x, k_y) = 2t\big[\cos k_x a + \cos\left(k_x a/2 + \sqrt{3}k_y a/2\right) + \cos\left(k_x a/2 - \sqrt{3}k_y a/2\right)\big], \tag{4.1}$$

where a is the inter-carbon distance.

Upon raising the *on-site energy* of ordered vacancy sites by ε, the system is driven into a charge density wave (CDW) state, with most part of the Fermi surfaces (b)&(c) gapped out. Only six Dirac points, the tips of the Dirac cones, are left in the original one-carbon Brillouin zone (BZ) [denoted by solid black boundary lines in (d)(e)&(f)]. As ε grows, the effects are further enhanced and the cone becomes more and more symmetric as from (j) to (k). Finally, the perfectly symmetric cone of graphene is reproduced as the vacancy sites become forbidden, $\varepsilon \to \infty$.

Deeper physical and mathematical insights can be obtained by investigat-

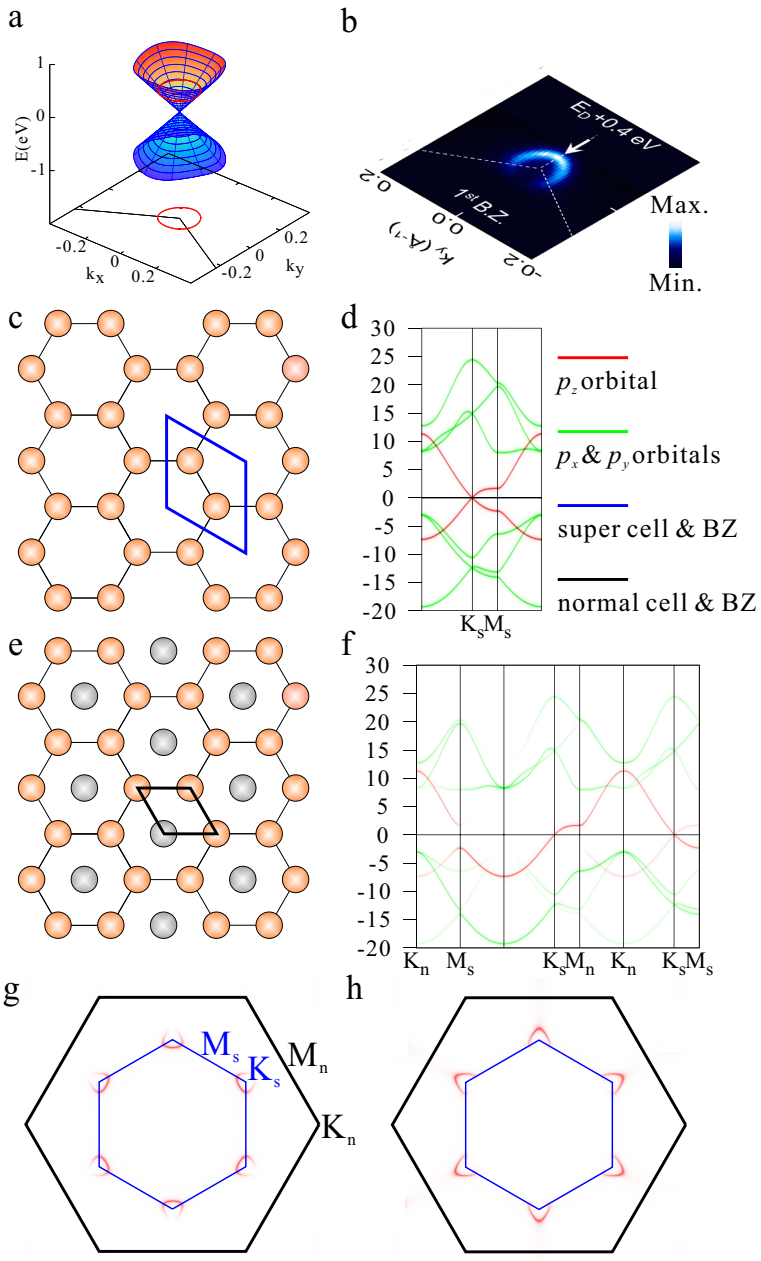

Figure 4.1: (a) Schematic diagram of Dirac cone dispersion. On the base, the red circle represents the energy contour to be compared with (b) ARPES data from Ref. [76] at 0.4 eV above Dirac point. (c) The graphene honeycomb lattice of the blue unit cell (as the super cell). (d) The first-principle band structure with color coded for various orbitals. (e) A reference triangular lattice of the black unit cell (as the normal cell) with the imaginary gray carbon, located at the hexagon center and treated as an vacancy. (f) The first-principle unfolded band structure in the normal cell basis with thickness representing spectral function magnitude. The subscript s (n) is for the high symmetry points of super (normal) cell. (g) and (h) are unfolded energy iso-surfaces at energy $= \pm 1$ eV.

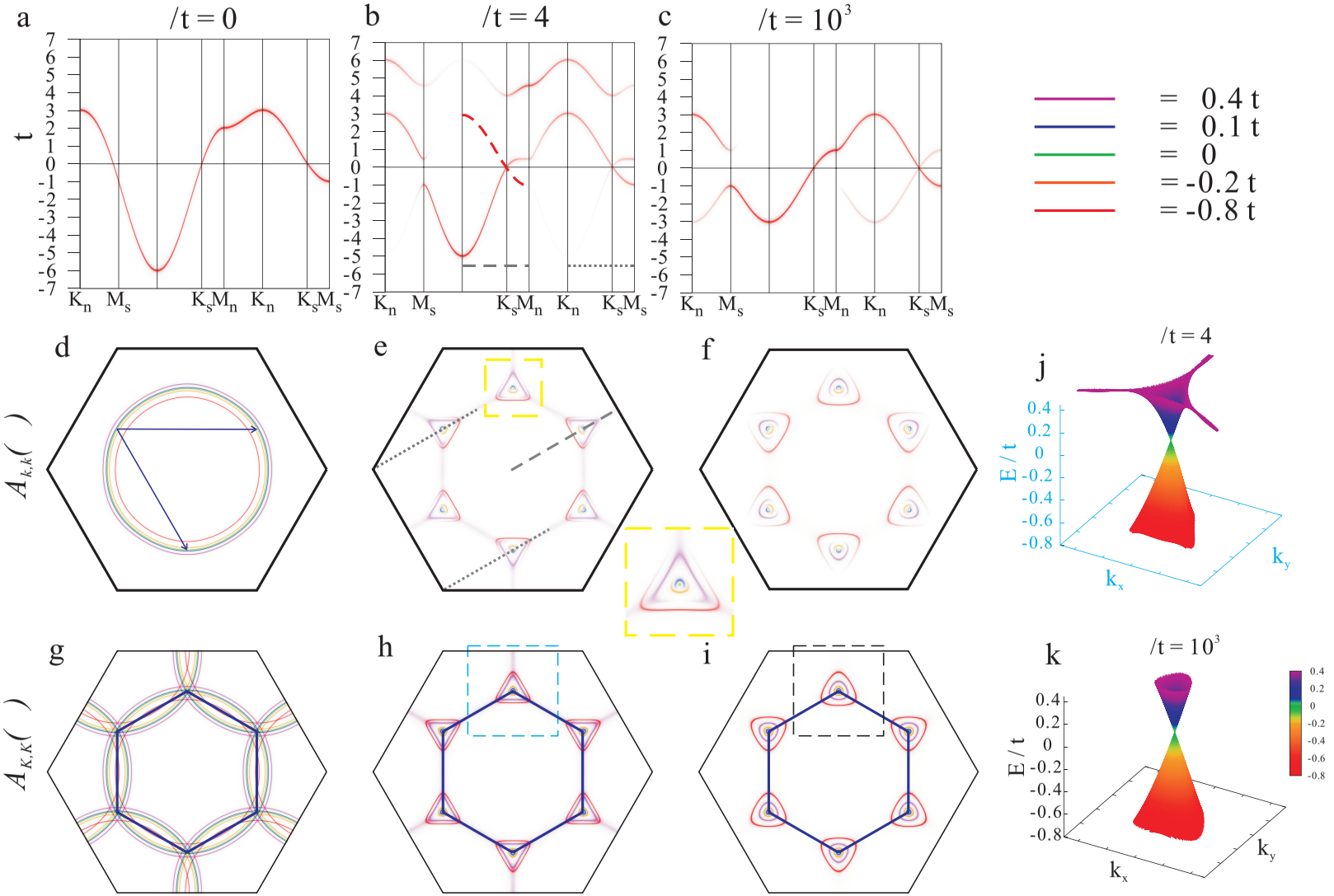

Figure 4.2: (a)-(c), unfolded band structure for $\varepsilon/t = 0,\ 4,\ 10^3$. (d) - (f) represent energy isosurfaces in the normal cell basis, namely $A_{k,k}(\omega)$, for three different ε/t. Color denotes different energy cuts. The yellow dashed square region in (e) is enlarged into an inset between the second and third row for details of non-uniform spectral weight distribution. (g) - (i) are the energy iso-surfaces plotted in super cell basis. To visualize Dirac cones, (j) and (k) are the energy dispersion of the cyan and black dashed squares in (h) and (i) respectively. The very flat band on the top cone in (j) is responsible for the hexagonal shape of the spectral function in (e) and (h).

ing the analytic structure of the full Hamiltonian including the hoppings in triangular lattice H_0 and the CDW potential $V_{k,k+q}$. All of them can be represented in the momentum space of a *reference triangular lattice*. Then H_0 is simply diagonal as $E_{tri}(k)$; the potential part becomes

$$V_{k,k+q} \propto \sum_{rr'} V_{rr'} e^{ik(r'-r)} e^{iqr'}, \tag{4.2}$$

where r and r' denotes the atomic sites, k the crystal momentum and q the CDW wave vector. For example in our current case, q's correspond to the two blue arrows in Fig. 4.2(d) and $q = 0$ so $V_{k,k+q}$ forms a 3×3 matrix. With only a local energy increase at the vacancy sites $V_{r,r'} = \varepsilon \delta_{r,r'}$, $V_{k,k+q}$ displays a very specific form within the subspace of the coupled three states:

$$V_{k,k+q} = \frac{\varepsilon}{3} \begin{pmatrix} 1 & 1 & 1 \\ 1 & 1 & 1 \\ 1 & 1 & 1 \end{pmatrix}. \tag{4.3}$$

Applying such a coupling to the three states in Fig. 4.2(d) that happen to be degenerate, one can find the E_{tri} is just a constant. The resulting eigenenergies are found by diagonalizing $V_{k,k+q}$ to be

$$\begin{pmatrix} 0 & 0 & 0 \\ 0 & 0 & 0 \\ 0 & 0 & \varepsilon \end{pmatrix}. \tag{4.4}$$

A two-fold degeneracy remains in the resulting eigenvalues, which form the Dirac points. Furthermore, with a slight deviation δk from these k points, E_{tri} of the three coupled states in (a) differs by small amounts δE_1 and δE_2, both proportional to δk. The total Hamiltonian becomes

$$\frac{\varepsilon}{3} \begin{pmatrix} 1 + 3\frac{\delta E_1}{\varepsilon} & 1 & 1 \\ 1 & 1 + 3\frac{\delta E_2}{\varepsilon} & 1 \\ 1 & 1 & 1 \end{pmatrix} + constant. \tag{4.5}$$

Taking $|\delta E_1| < |\delta E_2| \ll \varepsilon$ for convenience, one finds that linear dispersion develops around the Dirac point as two eigenenergies are found to be

$\frac{\varepsilon}{3}\{\frac{\delta E_1}{2\varepsilon}+2\frac{\delta E_2}{\varepsilon}, 3\frac{\delta E_1}{\varepsilon}-\frac{3}{8}\frac{\delta E_1^2}{\delta E_2 \varepsilon}\}$. Within such a one-carbon picture, we have demonstrated the formation of Dirac cones through an induced CDW of specifically structured CDW potential. The above analysis also locates the Dirac cones in momentum space from the reference CDW-free system, once the CDW q vectors to be applied are given.

The vanishing spectral intensity in Fig. 4.1 is also easily understood with a similar analysis. Along the k path on which two of the three coupled states remain degenerate ($\delta E_1 = 0$), for example two k-points on the $\overline{\mathrm{K_n K_s M_s}}$ path [gray dotted lines in Fig. 4.2(b)(e)] coupled to the third on the $\overline{\Gamma \mathrm{K_s M_n}}$ path [gray dashed line in Fig. 4.2(b)(e)], one of the resulting eigenvalues remains unchanged (zero): $\{3+\frac{\delta E_2}{\varepsilon}, 2\frac{\delta E_2}{\varepsilon}, 0\}$, and the corresponding eigenvector consists of anti-bonding superposition of *only* the two originally degenerate states. Against naive expectation, this band will not be folded to the third k point on the gray dashed line, where the corresponding spectral intensity must then vanish in Fig.4.1(g)&(h). The absence of folding intensity may be more clearly visualized in Fig. 4.2(b), where the band of missing weight is sketched in red dashed curve. In essence, within this one-carbon picture, the vanishing spectral intensity is intimately tied to the formation of the Dirac cones.

4.3 Dirac Cones in Two-dimensional Lattice with Enlarged Unit Cells

If we can periodically and locally increase the on-site energy by ε in a two-dimensional lattice, a new periodicity shows up to accommodate an enlarged unit cell. If the new unit cell is at least three times larger than its original one, we can keep the special format of $V_{k,k+q}$ like Eq. 4.3 and build Dirac cones in the new dispersion. With such a broken translational symmetry, $V_{k,k+q}$ has a size of $M \times M$ ($M \geq 3$) and is

$$\frac{\varepsilon}{M}\begin{pmatrix} 1 & 1 & \cdots & 1 \\ 1 & 1 & \cdots & 1 \\ \vdots & \vdots & \ddots & \vdots \\ 1 & 1 & \cdots & 1 \end{pmatrix}_{M\times M} . \tag{4.6}$$

Out of the M k points coupled by CDW wave vectors, geometrically it is *always* possible to couple at least three degenerate states within a regular two-dimensional dispersion.[2] Then $V_{k,k+q}$ leads to the appearance of Dirac cones around the M k-points of these degenerate states.[3] In principles there can be multiple sets of such coupled k-points, in which case the number of Dirac cones would multiply. Although the locations and energies of Dirac points depend on the details of the original dispersion, their existence is guaranteed.

To demonstrate the validity of this scenario, let us consider a two-dimensional one-band system with a square lattice and periodically introduce ε on 1/3 of the atoms as in Fig. 4.3(a). Fig. 4.3 demonstrates the creation of six anisotropic Dirac cones in the original BZ (two in the new reduced BZ). In the case with weaker potential ε (Fig. 4.3(c)&(f)), three regular "electron pockets" remain at the chemical potential. In general, the contribution to transport properties from the normal massive carriers on these pockets should be overwhelmed by those of the massless Dirac carriers, and thus does not cause any serious concern. These normal carriers can often be removed by gapping out the pockets with a stronger potential ($\varepsilon \longrightarrow \infty$ as vacancies), as shown in Fig. 4.3(d)&(g). Obviously, the closer the reduced BZ is to the original Fermi surface, the more effectively the potential can gap out these Fermi pockets.

Fig 4.4 shows that introducing ε on 1/4 of the atoms in Fig. 4.4(a) can indeed create six Dirac cones in the original BZ that resemble those in graphene very much. Out of four coupled k points, only three of them are degenerate, as indicated in Fig. 4.4(b). The state at the fourth k-point has a much higher energy and thus does not affect the other three in any significant manner.

4.4 Conclusion

In conclusion, we study the effect of raising on-site energy periodically in two-dimensional lattice in general. If the resulting super cell unit cell is at least

[2]If we consider three coupled k points, they can form a triangle with edges equal to three CDW wave vectors. Each vertex represents one k point. In a regular two-dimensional dispersion, we can arbitrarily fix two vertices at the same energy first, the last vertex is located at either higher or low energy. In a dispersion contour, we can smoothly fine-tune the orientation of this triangle and eventually find a set of three k points with the same energy.

[3]Please see Appendix A for mathematical derivations.

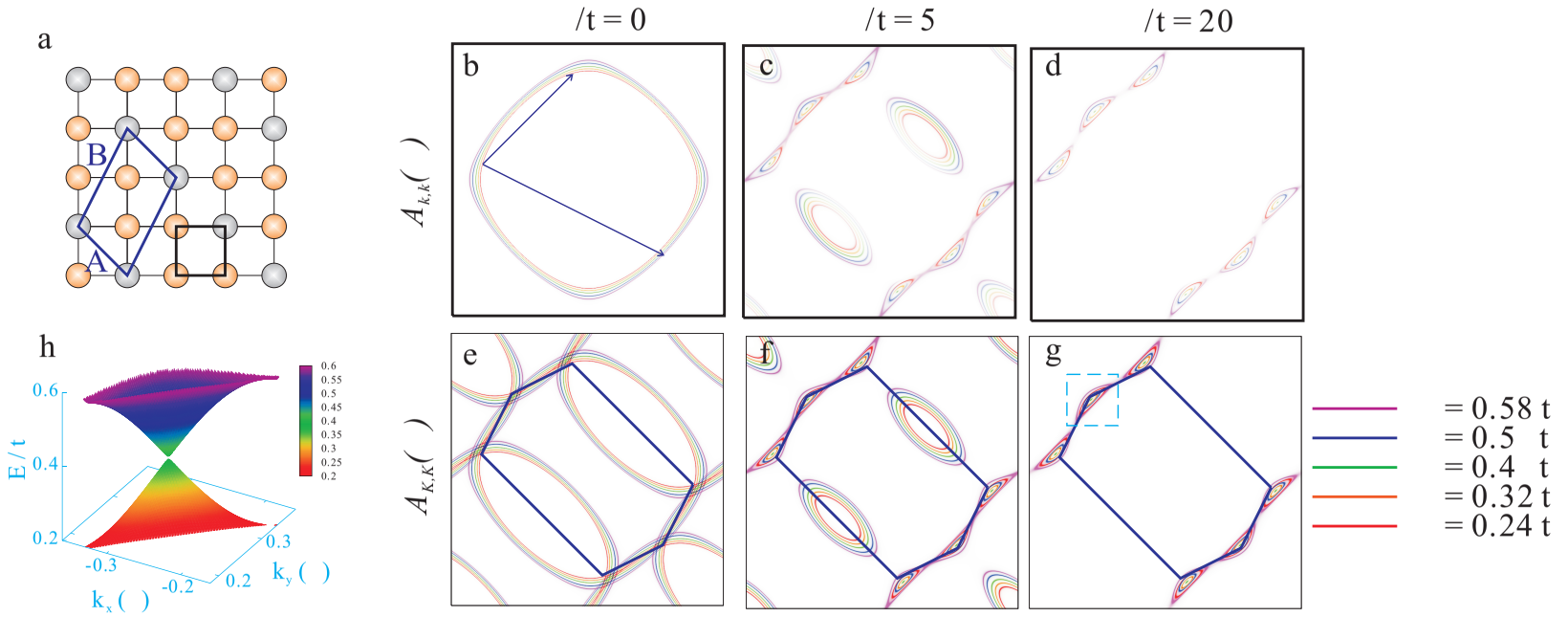

Figure 4.3: Dirac cones on square lattice with $\frac{1}{3}$ affected atoms(M=3). (a) The original square lattice of black normal cell and the blue super cell of $\{A = (1, \bar{1}), B = (1, 2)\}$. The zero energy and next nearest hopping are chosen as the on-site energy of the unperturbed orange atoms and 0.4 t respectively. The on-site energy of the gray atom is lifted to ε. (b) - (d) are the unfolded energy isosurfaces plotted in normal cell basis for ε/t =0, 5, 20. Color represents different energy cuts. (e) - (g) are energy isosurface in the super cell basis. (h) Energy dispersion in cyan dashed square of (g).

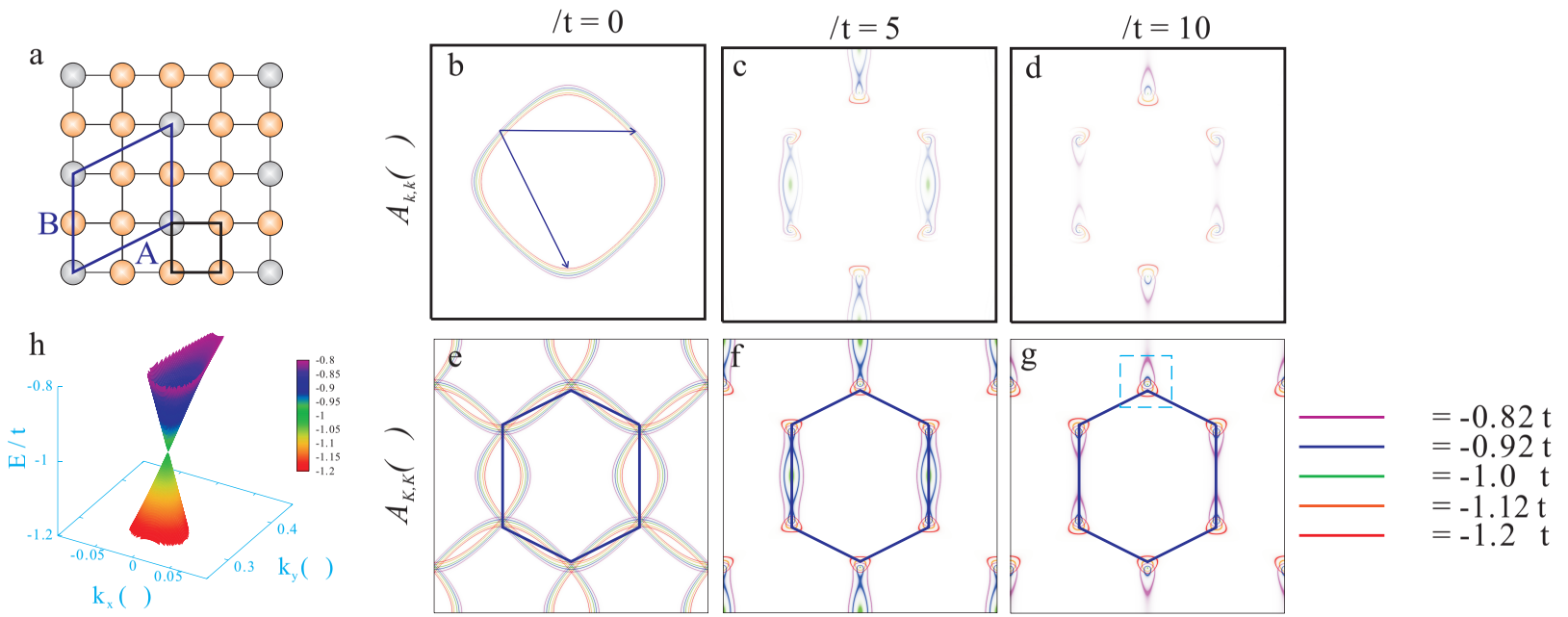

Figure 4.4: Dirac cones on square lattice with $\frac{1}{4}$ affected atoms (M=4). (a) The supercell of $\{A = (2, 1), B = (0, 2)\}$. The graph convention follows Fig. 4.3. (b) - (d) are the energy isosurfaces plotted in the normal cell basis for ε/t =0, 5, 20. Color represents different energy cuts. (e) - (g) are energy isosurfaces in the super cell basis. (h) Energy dispersion in cyan dashed square of (g).

three times larger than the original unit cell, the linear dispersion of Dirac cones can be built in the new dispersion. Graphene can be regarded as a special case in a triangular lattice. In the two examples in a square lattice, we successfully test the validity of our scenario. The resulting Dirac cones show specific anisotropy of the effective velocity and the orientation. It may provide a possible route to incorporate Dirac cones in future material design.

Chapter 5

Case 3: One-Fe versus Two-Fe Brillouin Zone of Fe-Based Superconductors

The work presented in this chapter has been published [78]. Based this work, the subsequent collaborative projects with other ARPES experimental groups are provided in Appendix B.

5.1 Introduction

One confusing/puzzling aspect of the new iron-based high-temperature superconductors is the dilemma of one-Fe vs. two-Fe description, concerning the translational symmetry of the system. The generic crystal structure of these materials consists of two inequivalent Fe atoms, distinguished by the alternating tetrahedral coordination of the pnictogen or chalcogen anions (c.f.: Fig. 5.1a). Since this coordination is known to impose dramatic impacts on the hopping integrals of Fe d orbitals [79], the associated broken translational symmetry (from the 1-Fe perspective) is expected to be physically significant and should be fully incorporated via the use of the unit cell that contains explicitly two Fe atoms. Yet, the observed neutron scattering intensity [80–83] shows little (if any) indication of such broken symmetry; it appears to follow simply the 1-Fe Brillouin zone (BZ) of a simple square lattice of Fe atoms (Fig. 5.1b). Furthermore, out of convenience, most theoretical studies

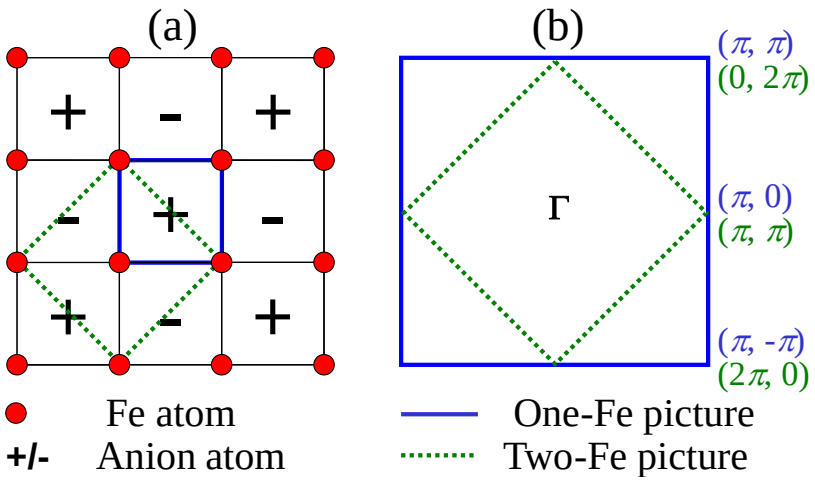

Figure 5.1: Illustration of (a) one-Fe and two-Fe unit cells with $+(-)$ anions located above (below) the Fe plane, and (b) the corresponding first Brillouin zones.

of superconductivity to date do not account fully for this broken translational symmetry, disregarding the rigorous symmetry constraint. It is thus important and timely to clarify quantitatively various aspects of the effects from this broken symmetry (its relevance/irrelevance), and to settle, once for all, the confusing status of the field on the 1-Fe vs. 2-Fe perspective.

In this study, three striking effects of the translational symmetry breaking potential (TSBP) are revealed by unfolding the *ab initio* electronic band structures (EBSs) and Fermi surfaces (FSs) of representative parent compounds back to the 1-Fe BZ: i) The folded Fe bands ("shadow" bands) possess overall weak spectral weight, explaining the 1-Fe perspective advocated by the neutron measurements, and indicating the necessity of the larger 1-Fe BZ in angle resolved photoemission spectroscopy (ARPES) as well. ii) The folding of the bands induces an unusual parity switching in their orbital characters, suggesting a change of photon polarization in ARPES. iii) Most strikingly, the widely discussed electron Fermi pockets around $(\pi, 0)$ and $(0, \pi)$ for supporting superconductivity would not have existed without the TSBP. This advocates strongly the full inclusion of TSBP (the two-Fe perspective) in theoretical understanding of superconductivity in these materials, and suggests a critical re-examination of the debated nodal structure of the superconducting order parameter [84–92] on the electron pockets.

Table 5.1: Lattice information of first-principles calculation in Fe-based superconductors.

	LaFeAsO	$BaFe_2As_2$	LiFeAs	FeTe	$K_{0.8}Fe_{1.6}Se_2$
a=b (Bohr)	7.615732	7.488039	7.127100	7.221591	16.47577
c (Bohr)	16.51017	24.59819	12.01380	11.84764	26.61737
anion height	0.1326061	0.354500	0.265000	0.249600	0.282740
k mesh	16x16x7	13x13x13	14x14x8	17x17x10	11x11x11

5.2 Method

Our theoretical analysis is based on unfolded first-principles EBSs and FSs of the normal state in 1-Fe perspective, which reveals explicitly various aspects of the TSBP effects. Standard density functional theory (DFT) calculations were conducted with local density approximation as implemented in the WIEN2k package [12] in the multiple-Fe unit cell (8 Fe for $K_{0.8}Fe_{1.6}Se_2$ and 2 Fe for the rest).[1] The essential lattice and computational parameters used in the calculation are summarized in Table 5.1. Based on the DFT results, symmetry-respecting Wannier functions [48] with Fe d and anion p characters were constructed to capture the low energy Hilbert space within [-6, 3] eV, from which the low energy effective tight-binding Hamiltonians were calculated. Finally, unfolded EBSs and FSs were obtained via the recently developed first-principles unfolding method [26].

The basic idea of our unfolding method [26] is to simply change the representation of the energy-, ω-, dependent one-particle spectral functions of the real system (two-Fe zone), $A_{KJ,KJ}(\omega)$, from the basis of original crystal momentum K and band index J to the basis of crystal momentum k and orbital index n of a more symmetric reference system (1-Fe zone): $A_{kn,kn}(\omega) = \sum_{KJ} |\langle kn|KJ\rangle|^2 A_{KJ,KJ}(\omega)$. This change of basis is made simple with the use of first-principles Wannier functions. As demonstrated below, the unfolded EBSs and FSs provide explicit and detailed information on each band's coupling to the TSBP in an orbital specific manner. Additionally, it has been shown [26] that the unfolded spectral function corresponds directly to the

[1] For each parent compound, the lattice constants and atomic positions were obtained from the experimental data of the high temperature nonmagnetic state of LaFeAsO [93], $BaFe_2As_2$ [94], LiFeAs [95], FeTe [96], and $K_{0.8}Fe_{1.6}Se_2$ [97]. We followed the default settings of version 10.1 with $R_{mt}K_{max} = 7$ and $l_{max} = 10$ to reach convergence of the ground state density.

intensity of ARPES, as it includes the main matrix element effects of the measurement (expect the remaining atomic dipole matrix element to be determined based on the chosen photon polarization). This use of "regular" momentum distinguishes our method from the glide symmetry-based unfolding employed by, for example, Anderson and Boeri [98], in which the twisted geometry does not have direct correspondence to the ARPES. Similarly, the use of regular momentum is essential in the widely applied spin fluctuation studies [84, 85, 87] of superconductivity via magnetic susceptibility, $\chi(q, \omega)$, since the momentum transfer q concerns the *difference* of two k points.

5.3 Unfolded Band Structure and Fermi Surfaces

Our resulting unfolded EBSs and FSs of the representative families in the nonmagnetic state are shown in Fig. 5.2, colored to emphasize the essential Fe d orbitals. A few generic features of unfolding can be clearly observed, for example, in Fig. 5.2c. The most obvious one is the appearance of the shadow bands, generated from band "folding" via the TSBP. Since here the TSBP is of momentum $q^{TSBP} = (\pi, \pi, 0)$ in the 1-Fe BZ unit (except for $BaFe_2As_2$ and $K_{0.8}Fe_{1.6}Se_2$, whose double layer structure gives $q^{TSBP} = (\pi, \pi, \pi)$ instead) each band is folded from k to $k + q^{TSBP}$, as illustrated by the arrows in the lower panel. Note that the conservation of spectral weight dictates a weaker spectral weight for those "main" bands that develop stronger shadow bands. Also associated with the shadow band formation are the additional gap openings occurring at the 2-Fe BZ boundaries, indicated by an ellipse in Fig. 5.2c as an example. Obviously, the intensity of the shadow bands and gap opening size reflect (although not necessarily represent fully) the bands' coupling to the broken symmetry.

Fig. 5.2 shows clearly that the anion bands within [-6, -2] eV develop very strong shadows bands, of comparable intensity to the main bands. This reflects their strong coupling to the TSBP, as it is the alternating positioning of the anion that breaks the translational symmetry. Given that one can hardly distinguish the main bands from the shadow bands, it is obviously more convenient to consider these anion bands in the 2-Fe BZ.

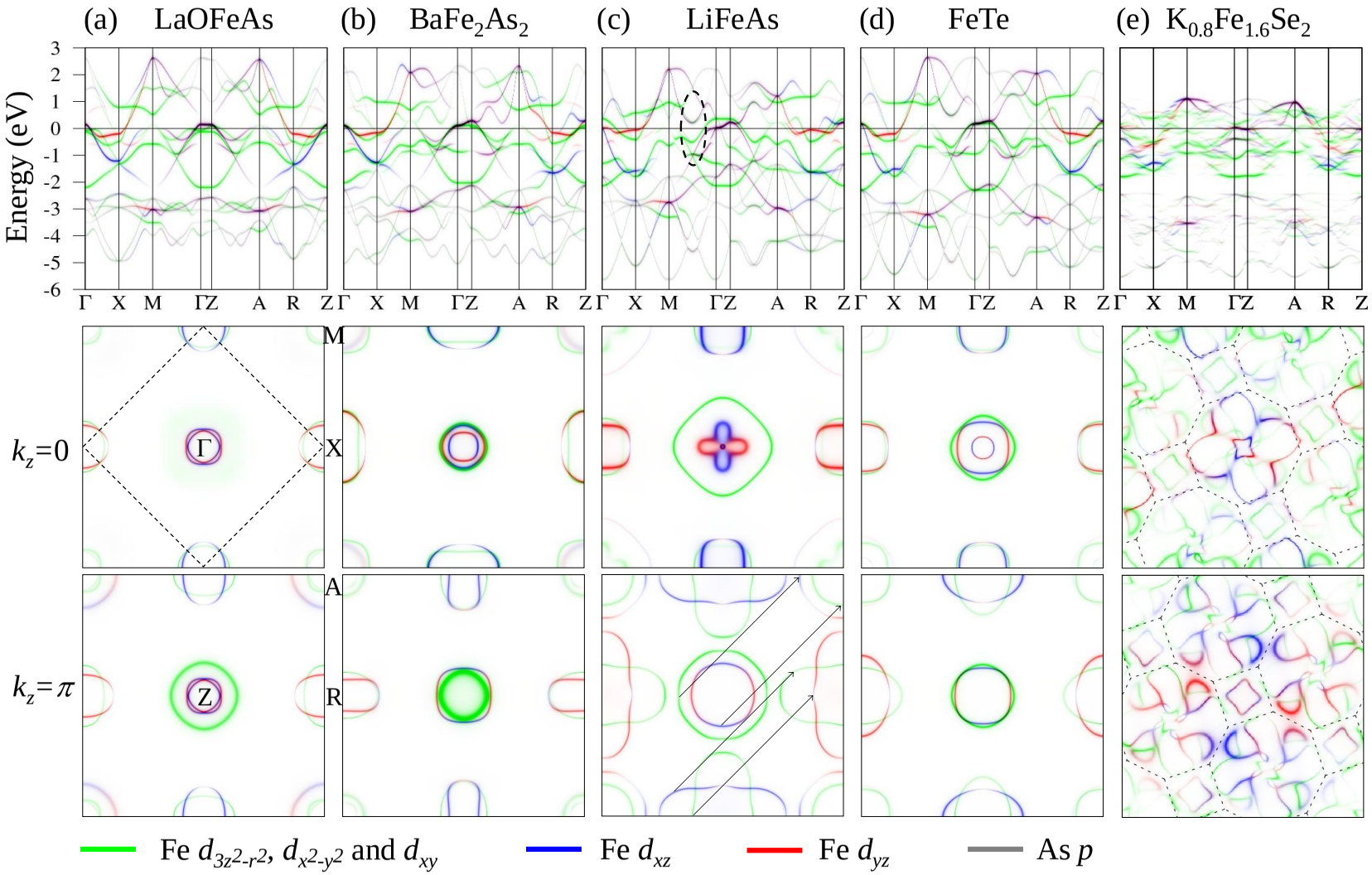

Figure 5.2: Unfolded EBSs (top panel) and FSs at $k_z = 0$ (middle panel) and $k_z = \pi$ (bottom panel) in 1-Fe BZ of (a) LaFeAsO, (b) $BaFe_2As_2$, (c) LiFeAs, (d) FeTe, and (e) $K_{0.8}Fe_{1.6}Se_2$ with spectral intensity colored by green (Fe $d_{3z^2-r^2}$, $d_{x^2-y^2}$, and d_{xy}), blue (Fe d_{xz}), red (Fe d_{yz}) and grey (anion p). The dashed lines marks the strict BZ boundaries. The arrows illustrate the folding of bands, and dashed ellipse in (c) points to an example of gap openings.

In great contrast, the Fe bands near the Fermi level have rather weak shadow bands. In fact, if it weren't for the gap openings (some of which are quite large), the Fe bands would have looked just like those from a simple 5-band system. The overall weak intensity of shadow bands explains why neutron spectra appear to respect the 1-Fe BZ: Even though the real symmetry of the system dictates the 2-Fe BZ, the folding of the spectrum is just not strong enough for a clear experimental identification. In fact, the lack of folded bands was also reported in a recent ARPES experiment. [1] Consequently, a larger 1-Fe BZ is *necessary* in future ARPES measurements, since only about half of the EBSs are clearly observable in the 2-Fe BZ, where most ARPES to date were conducted.

5.4 Discussion

Fig. 5.2 also reveals an interesting orbital-parity switching of the band folding, obvious from the change of color of the Fe-bands. Consider the FSs, for example. The blue (d_{xz}) and red (d_{yz}) bands of odd parity w.r.t. the Fe plane always have green ($d_{3z^2-r^2}$, $d_{x^2-y^2}$, and d_{xy}) shadow bands of even parity, and *vice versa*. This can be understood from the structure of TSBP in these systems. Table 5.2 gives the nearest neighbor hopping integrals for the low-energy Fe d bands in $BaFe_2As_2$ by integrating out As p orbitals. One sees that the alternating positioning of the anion (c.f. Fig. 5.1a) leads to an alternating sign of all $t_{even,odd}$, and thus breaks the translational symmetry. Consequently, these terms form the main body of the TSBP, and dictate a switching of parity in the band character upon band folding. This novel behavior is quite distinct from the common cases of ARPES, in which the replica of bands beyond the first BZ retain the orbital character. Here, the weak replica always possess a different character across the BZ boundaries and thus require a different photon polarization to clearly observe, similar to the recent reports on $Bi_2Sr_2CaCu_2O_{8+\delta}$ [99].

The most significant feature revealed in Fig. 5.2 is the *incompleteness* of the unfolded electron pockets around the X (and R) points. Taking $BaFe_2As_2$ in Fig. 5.2b as an example, near the X=$(\pi, 0, 0)$ point, the intensity of the strong red pocket vanishes dramatically near the Γ-X path. Consequently, only the

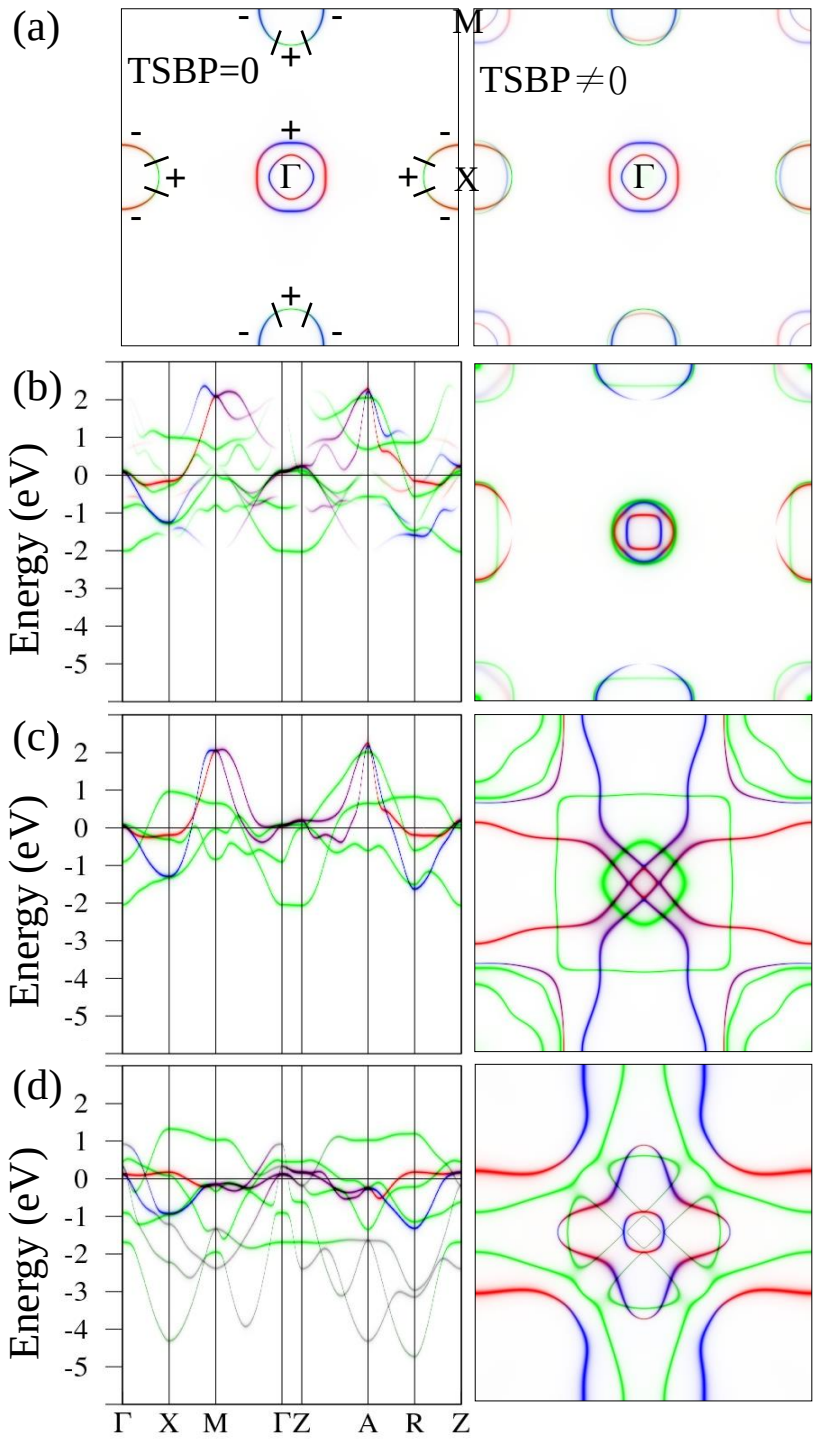

Figure 5.3: (a) Folding of complete electron pockets (from Ref. [84]) and illustration of currently proposed nodal structure of the superconducting order parameter. (b) First-principles results showing *incomplete* electron pockets instead ($BaFe_2As_2$ as the example). (c)(d) Demonstration of loss of electron pockets by dropping TSBP in both 5- and 8-band VCA descriptions.

Table 5.2: Nearest-neighbor hopping integrals (in eV) along the x-direction $\langle r\prime+(100), n|H|r\prime, n\prime\rangle$ among Fe d Wannier orbitals for nonmagnetic $BaFe_2As_2$. The option in sign corresponds to two inequivalent Fe sites. Bold font highlights orbitals with odd parity.

	$3z^2-r^2$	x^2-y^2	xy	**xz**	**yz**
$3z^2-r^2$	0.03	0.31	0	0	$\mp$0.12
x^2-y^2	0.31	$-$0.34	0	0	$\pm$0.34
xy	0	0	$-$0.12	$\mp$0.22	0
xz	0	0	$\mp$0.22	$-$0.06	0
yz	$\mp$0.12	$\pm$0.34	0	0	$-$0.32

green shadow pocket of d_{xy} character, folded from the blue pocket around R=$(0,\pi,\pi)$ (c.f. bottom panel of Fig. 5.2b), is visible here, in agreement with recent ARPES measurement [100]. In fact, none of the unfolded pockets near X and R points are complete in Fig. 5.2, contrary to the common assumption that each X/R point has one strong *complete* pocket and obtains a weaker shadow pocket via band folding (c.f. Fig. 5.3a). All the electron pockets here are instead formed by *combining* main bands near X and R points via the TSBP. In other words, without breaking the 1-Fe translational symmetry, the essential electron pockets would have *never existed* in these systems.

To better illustrate this important finding, let us construct a translational symmetric Hamiltonian (in 1-Fe unit) via the virtual crystal approximation (VCA) to the above effective Fe d-band Hamiltonian[2]:

$$H^{VCA}_{r,n;0,n\prime} = \sum_{r\prime} H_{r\prime+r,n;r\prime,n\prime} / \sum_{r\prime} 1.$$

This zeros out all TSBP (including the above $t_{even,odd}$ terms), and keeps all translational symmetric terms intact. The resulting EBS and FSs at $k_z = 0$ are given in Fig. 5.3c. Even though the overall EBS still follows the original structure in Fig. 5.3b (minus the shadow bands and gap opening obviously), the topology of the FSs is drastically modified. In particular, there are no electron pockets around the X point anymore. The same is found in the VCA of our original Hamiltonian containing Fe d and As p orbitals (Fig. 5.3d). Evidently, the TSBP is instrumental in creating the electron pockets, and thus should be fully included in future theoretical modeling of magnetism and

[2]See Appendix C for more details.

superconductivity.

Our findings have direct and significant implications on the heatedly debated issue of nodal structures of the superconducting order parameter on the electron pockets. Current spin fluctuation theories [84–86] suggest accidental nodes in the s_{+-} order parameter [101, 102] on the electron pockets (see Fig. 5.3(a), due to strong inter-electron-pocket scattering. While the existence of nodes appears to be supported by the interpretations of the penetration length and several other measurements [88–90], it contradicts with the nodeless and almost isotropic gaps observed in ARPES [91, 92]. We find that precisely near the region of the nodes, ARPES would have negligible intensity, and thus can easily miss the nodal structure. On the other hand, the above mentioned theories did not incorporated appropriately the essential TSBP, and consequently are based on FSs of *qualitatively* different spectral intensity and orbital structures. Specifically, one would expect that the above incompleteness of the electron pockets, the mismatch in the orbital characters, and the addition of non-diagonal coupling between the pockets, can all affect quite strongly the inter-pocket scattering and alter the position or even the existence of the calculated accidental nodes on the electron pockets. Thus, a careful re-examination of the theoretical prediction would be of great interest and importance.

5.5 Vacancies Ordered $K_{0.8}Fe_{1.6}Se_2$

Finally, let's consider the second TSBP introduced by ordered 20% Fe vacancies in $K_{0.8}Fe_{1.6}Se_2$ [103]. The long period of the vacancy ordering, corresponding to a small $q^{TSBP} = \pm(\frac{3\pi}{5}, \frac{\pi}{5}, \pi)$ and $\pm(\frac{-\pi}{5}, \frac{3\pi}{5}, \pi)$, leads to a tiny BZ, making it difficult to compare standard DFT results [104] with the experiments. Our unfolded EBS and FSs thus offer a direct comparison with experimental spectra, and provide a few theoretical insights. Contrary to the above discussions, the Fe-vacancy induced TSBP causes a strong coherent scattering of the Fe bands, producing a larger number of shadow bands and strong gap openings all over the 1-Fe BZ. Consequently, the overall band width of the Fe bands reduces by about 1/4, much more than the anion bands. Not surprisingly, the resulting FSs are seriously reconstructed, showing little re-

semblance to the generic FSs of other cases, particularly lacking the nesting of the Fermi pockets. This disagrees drastically with recent ARPES experiment, which reported well-defined Fermi pockets [105]. Thus, the Fe-vacancy must order only weakly (or locally) in the measured samples, as observed recently by electron microscopy [106]. Similarly, now it seems more obvious that the recent experimental finding of enhanced superconductivity by promoting disorder of Fe-vacancies [107] is mostly through the recovery of approximately nested Fermi pockets.

5.6 Conclusion

In conclusion, our first-principles unfolded EBSs and FSs reveals three key features of the translational symmetry breaking due to alternating anion positioning, in all families of the Fe-based superconductors. First, the folded shadow bands have rather weak spectral weight. This explains the apparent respect to the 1-Fe BZ in neutron measurements, and highlights the necessity of covering the larger 1-Fe BZ in future ARPES experiments. Second, TSBP induced band folding changes the orbital character to those with opposite parity w.r.t. the Fe plane. This unusual phenomenon suggests a change of photon polarization in ARPES experiment. Finally and most significantly, the electron pockets, critical to most theories of magnetism and superconductivity of these materials, only form via the TSBP. Thus, full inclusion of the broken translational symmetry (e.g. using 2-Fe unit cell) is essential in future theories, particularly on the debated issue of nodal structure of the superconducting order parameter on the electron pockets.

Chapter 6

Case 4: Orbital-Parity Selective Superconducting Pairing Structures of Fe-based Superconductors under Glide Symmetry

The work presented in this chapter is the extended study from Chapter 5 and unpublished. More discussions will be focused on the superconducting structures.

6.1 Introduction

One of the highly debated questions in high-temperature Fe-based superconductors (FeSC) [108] is the superconducting pairing symmetry. After the first proposal of a global s-wave symmetry with the opposite signs on the electron and hole pockets by Mazin *et al.* [101], numerous follow-up microscopic modelings have shown the existence of the BCS instability mediated by fluctuations in both spin [84, 86, 87, 109] and orbital [110] degrees of freedom. However, different competing pairing symmetries are close in energy [86] so the leading term can vary from so-called nodal/nodeless $s_{\pm}$ [111, 112], s_{++} [113] to $d_{x^2-y^2}$ symmetry [114] depending on the compound types, dopings, and interaction

conditions. From the experimental side, although mounting evidence in angle resolved photoemission spectroscopy (ARPES) measurements have revealed full superconducting gaps of either negligible or weak anisotropy [92, 115–119], there is a strong contradiction with the nodal gap signatures revealed in bulk measurements, such as London penetration depth [88, 90, 120], specific heat [121], and nuclear magnetic resonance [89]. Despite the lack of decisive experiments with both phase sensitivity and the momentum resolution, all of these discrepancies remain to be conclusively answered.

One unique property hindering the theoretical development in FeSC is the in-plane broken translational symmetry. The staggered positions of the anions generate a non-perturbable band folding potential [78, 122, 123] and turn the in-plane translation into a glide translation. Because the glide symmetry involves a mirror reflection followed by the translation on the Fe layer, the parity of Fe d orbitals (with respect to the Fe plane) not only characterizes a orbital-parity switching in kinetic energy [78] but also helps formulate pairing symmetries in quantum Monte Carlo studies [124]. One of the indirect evidences is recent laser ARPES data in $Ba_xK_{1-x}Fe_2As_2$ [125, 126], indicating that the angular modulation of the superconducting gap significantly differs across the Γ hole pockets. Therefore, it is relevant to examine the impact on the electronic structure imposed by the glide symmetry in the orbital-parity selective manner.

In this study, we identify the orbital-parity selectivity by studying the Hamiltonian with glide symmetry in the generic Fe-based superconductors. We show that every quasiparticle, defined in the one-particle spectral function, is only allowed to carry one orbital parity and always has its degenerate counterpart with opposite parity upon a momentum $Q = (\pi, \pi, 0)$ shift. The intra-orbital-parity Cooper pairs must have the total zero-momentum and distinct gap structures across orbital parities. The Cooper pairs formed by one odd and one even quasiparticles possess the characteristic of the finite momentum Q, the *spatial* odd parity and the time-reversal symmetry breaking.

6.2 Hamiltonian with Glide Symmetry

In FeSC of $P4/nmm$ space group, the generic non-interacting Hamiltonian of Fe $3d$ orbitals can be formulated as in-plane $H_0^{\parallel}$ and out-of-plane $H_0^{\perp}$:

$$H_0^{\parallel} = \sum_{ii'(i_z=i'_z)nn'} (p_n p_{n'})^{\theta_i+\theta_{i'}} t_{ii'}^{nn'} a_{in}^{\dagger} a_{i'n'}. \tag{6.1}$$

$$H_0^{\perp} = \sum_{II'(i_z\neq i'_z)nn'} (p_n p_{n'})^{\theta_i+\theta_{i'}} t_{II'}^{nn'} a_{In}^{\dagger} a_{I'n'}. \tag{6.2}$$

The five Fe d orbitals n's are categorized into even orbital parity $(d_{z^2}, d_{x^2-y^2}, d_{xy})$ with $p_e = +1$ and odd (d_{xz}, d_{yz}) with $p_o = -1$. The Fe lattice site is labeled by either $i = (i_x, i_y, i_z)$ or $I = (i_x, i_y, (-1)^{\theta_i} i_z)$, where $\theta_i = i_x + i_y$ distinguishes two sub-lattices. In this notation, the hopping integrals $t_{ii'}^{nn'}$ as well as $t_{II'}^{nn'}$ only depend on the relative distance $(i - i')$. The presence of sign change factors $(p_n p_{n'})^{\theta_i+\theta_{i'}}$ and $(-1)^{\theta_i+\theta_{i'}}$ are required by the glide symmetry.

The dominant term of translational symmetry breaking in FeSC originates from the sign $(p_n p_{n'})^{\theta_i+\theta_{i'}}$ in $H_0^{\parallel}$. This sign distinguishes two sublattices by constantly changing the sign on the inter-orbital-parity hoppings from one sublattice to another. Instead of being a small correction, the band folding from the one-Fe Brillouin zone (BZ) to two-Fe BZ involves a non-perturbative potential with the same order of magnitude as the regular hopping terms. As depicted by the orbital-dependent one-particle spectral function represented in the one-Fe BZ basis in Fig 6.1(a), a_{kn} are strongly hybridized with $a_{k+Qn'}$ only when $p_n p_{n'} = -1$. For example, the three hole pockets surrounding Γ are folded to the replica at zone corner M, and the orbital changes from d_{yz}/d_{xz} (red/blue) to d_{xy} (green) and vice versa. This is so-called orbital-parity switching folding [78] we have discuss in Chapter 5 and indicates a strong umklapp process in a orbital-parity selective manner within the one-Fe BZ. Therefore, the traditional picture based on the unbroken in-plane translational symmetry will be no longer applicable here.

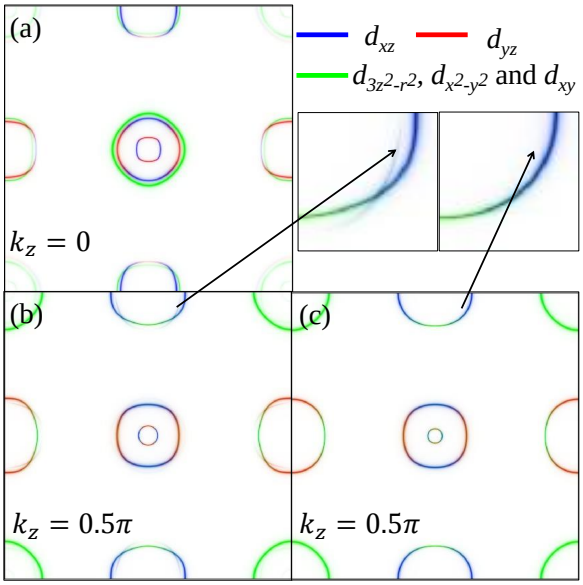

Figure 6.1: (a) The unfolded one-particle spectral function $A_n(k, \omega = 0)$ at Fermi energy calculated from first-principles FeTe Wannier orbitals (see Ref. [78] for details). The spectral function in local gauge space $\tilde{A}_n(\tilde{k}, \omega = 0)$ (b) with and (c) without $H_0^{\perp}$ terms. The enlargements show the folded spectral weights from H_0^{out} are hardly visible in (b) and vanished in (c).

6.3 Local Gauge and Physical Momentum Spaces

Thanks to glide symmetry, we are able to avoid the complex umklapp process by defining a local gauge transformation as $c_{in} \equiv (-p_n)^{\theta_i} a_{in}$ [98, 122, 123] so that

$$H_0^{\parallel} = \sum_{ii'(i_z=i'_z)nn'} t_{ii'}^{nn'} c_{in}^{\dagger} c_{i'n'}, \tag{6.3}$$

$$H_0^{\perp} = \sum_{II'(i_z \neq i'_z)nn'} t_{II'}^{nn'} c_{In}^{\dagger} c_{I'n'}. \tag{6.4}$$

The Fourier space of c_{in} now is labeled by $(\tilde{k}_x, \tilde{k}_y, k_z)$, where the *tilde* refers to pseudo-momentum and quantities in local gauge space. Although the one-Fe periodicity in $H_0^{\parallel}$ is recovered through the local gauge transformation, the translational symmetry still remains broken by $H_0^{\perp}$. In fact, the glide translation in a realistic three-dimensional system never commutes with the out-of-plane translation so no eigenstates in a one-Fe BZ can simultaneously have the

well-defined momenta along three directions in Cartesian coordinates. However, the importance of the remaining coupling is diluted by factor in-plane and out-of-plane hopping ratio $|t_\perp/t_\parallel| \ll 1$. In Fig 6.1(b) and its inset, the first-principle results of FeTe compounds verify that the folded spectral weights are negligibly weak. If $H_0^\perp$ is assumed to be zero, Fig 6.1(c) and its inset show no obvious change in either dispersion nor wavefunction except for the disappearance of the weak spectral weights. The local gauge space is capable of providing the exact and approximate eigenstates of recovering one-Fe periodicity in two and three dimensions, respectively. Thus, the previous studies built in local gauge space that we shall mainly consider hereafter should be qualitatively correct in capturing essential physics.

6.4 Orbital-Parity Selective Quasiparticles

The existence of such a local gauge space makes it easy to decode the obscure spectral function in Fig. 1(a) and reveal the orbital-parity selective quasiparticles. With the transformation between the physical momentum and the pseudo-momentum bases, $a_{k,o} = c_{\tilde{k},o}$ and $a_{k,e} = c_{\tilde{k}+Q,e}$, the spectral function can be transformed accordingly [123]:

$$A_o(k,\omega) = \tilde{A}_o(\tilde{k},\omega), \tag{6.5}$$

$$A_e(k+Q,\omega) = \tilde{A}_e(\tilde{k},\omega). \tag{6.6}$$

In other words, every quasi-particle can only carry one orbital parity at the physical momentum k and its degenerate counterpart of opposite parity at $k+Q$. This is because they originate from one single eigenstate in $\tilde{A}_n(\tilde{k},\omega)$. This unique selectivity has been observed in recent ARPES data from $BaFe_{1-x}Co_xAs_2$ [1] as well as $FeTe_{1-x}Se_x$ [2] and expected to facilitate the orbital characterization of the ARPES experiments.

6.5 Orbital-Parity Selective Superconducting Pairings

The orbital-parity selectivity implies an unusual superconducting state consisting of three kinds of coexisting Cooper pairs: two intra- and one inter-orbital-parity pairing structures. Since the Fermi surface plays a dominant role in stabilizing superconductivity, one leading pairing symmetry survives in local gauge space that has been heavily investigated by various theoretical works [84, 86, 87, 101, 109, 110]. For the sake of simplicity, we assume that a zero-frequency anomalous Green's function is pre-determined in the local gauge space and projected to orbital basis as $\tilde{F}_{mn}(\tilde{k}) = \langle c_{-\tilde{k}m} c_{\tilde{k}n} \rangle \propto \tilde{\Delta}(\tilde{k})\tilde{\phi}_m(-\tilde{k})\tilde{\phi}_n(\tilde{k})$, where $\tilde{\Delta}(\tilde{k})$ and $\tilde{\phi}_n(\tilde{k})$ are the gap function and the wavefunction projected to orbital n at the Fermi surface, respectively. After the same transformation to physical momentum basis, a Cooper pair of two odd quasiparticles at $\pm k$ implies the existence of the counterpart even pair at $\pm(k+Q)$. In addition, a $-k$ odd quasiparticle is also allowed to be paired with another $k+Q$ even one, and this interestingly forms a Cooper pair carrying total momentum Q. Instead of one pairing symmetry, glide symmetry in FeSC naturally leads to a condensate consisting of the three distinct pairing structures.

One significant implication from our finings is that the orbital-parity selectivity influences the gap nodes on the electron pocket, a finding that still requires conclusive confirmation by experiments. We start with the anomalous Green's function and focus on the leading intra-orbital pairing,

$$F_o(k) \propto \tilde{\Delta}(\tilde{k})|\tilde{\phi}_o(\tilde{k})|^2, \tag{6.7}$$

$$F_e(k) \propto \tilde{\Delta}(\tilde{k}+Q)|\tilde{\phi}_e(\tilde{k}+Q)|^2. \tag{6.8}$$

The odd orbitals inherit gap symmetry from $\tilde{\Delta}(\tilde{k})$, but the even orbitals have a Q-shifted gap function $\tilde{\Delta}(\tilde{k}+Q)$. Among the four commonly discussed symmetries in FeSC: $\tilde{\Delta}_s$, $\tilde{\Delta}_{s_\pm}\cos\tilde{k_x}\cos\tilde{k_y}$, $\tilde{\Delta}_{s_{++}}(\cos\tilde{k}_x+\cos\tilde{k}_y)$ and $\tilde{\Delta}_{d_{x^2-y^2}}(\cos\tilde{k}_x-\cos\tilde{k}_y)$ [1], the Q shift only affects the last two by adding an

[1] We adopt the convention for pairing in real space, so $\tilde{\Delta}_s$ and $\tilde{\Delta}_{s_{++}}$ represent the on-site and the nearest neighbor pairing, respectively. Both $\tilde{\Delta}_{s_{++}}$ and $\tilde{\Delta}_{d_{x^2-y^2}}$ involve the next-nearest neighbors.

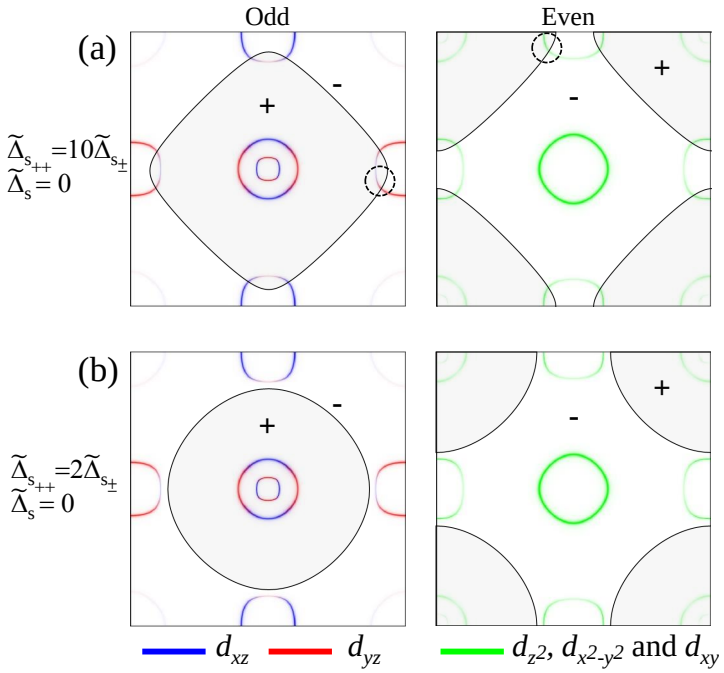

Figure 6.2: Schematic diagrams of orbital-parity selective pairing structures in the intra-orbital Cooper channel as shown in Eq.(6.9). The black curves and the shaded/unshaded regions represent the nodal line and the sign structure, respectively.

extra minus sign across the orbital parities. To show the relevance of the minus sign, we consider the mixture of the three s-wave superconducting order parameters,

$$\Delta_{o/e}(k) = \tilde{\Delta}_s + \tilde{\Delta}_{s_\pm} \cos k_x \cos k_y \pm \tilde{\Delta}_{s_{++}} (\cos k_x + \cos k_y). \tag{6.9}$$

In Fig. 6.2(a), we present the case $\tilde{\Delta}_{s_{++}} \gg \tilde{\Delta}_{s_\pm}$ and $\tilde{\Delta}_s = 0$. The structures of the order parameters are plotted for odd (a, left) and even (a, right) with the one-particle spectral function as the background. Note that at Γ point the red-and-blue hole pockets in (a, left) carry the opposite sign of the gap with respect to the green hole pocket in (a, right). Moreover, the intersection of the electron pockets and the nodal lines depicts the widely discussed gap nodes due to interaction between the electron pockets. The locations of gap nodes on d_{xz}/d_{yz} and d_{xy} quasiparticles can not coincide, but are related by a Q shift. Since the diminished spectral weight around the node in (a, left) makes the ARPES detection harder, we suggest that probing the node on d_{xy} shown in (a, right) could be much easier.

As an alternative to directly detect the phase of the order parameter, our finding reveals the nature of the orbital-party selectivity in gap anisotropy may help to determine the gap symmetry. In the case of $\tilde{\Delta}_{s++} \sim 2\tilde{\Delta}_{s\pm}$, the nodal line of $\Delta_o(k)$ becomes circular as shown in Fig. 6.2(b, left) and induces negligible gap anisotropy at the circular hole pockets (red/blue). In contrast, $\Delta_e(k)$ forms the four pieces of nodal arcs, and then creates the potentially strong gap anisotropy for the green hole pocket at Γ point as shown in (b, right). This anisotropy is further enhanced either by the presence of a positive $\tilde{\Delta}_s$ or the growth of hole pockets with hole doping. Both ways would push the nodal arcs and the green hole pockets in (b, right) closer and possibly in touch. Therefore, it is expected that the gap directly observed by ARPES measurements would show strong angular modulation in one parity and nearly absent in the other.

The scenario of the strong orbital-parity-selective gap anisotropy is supported in the recent laser ARPES experiments in $Ba_xK_{1-x}Fe_2As_2$ with only large hole pockets at Γ point [125, 126]. As shown in Fig. 6.3(a) (the digitalized data obtained from the two largest pockets in Fig 3 of Ref. [126]), the outer pocket (black dots and mostly d_{xy}) has stronger angular modulation

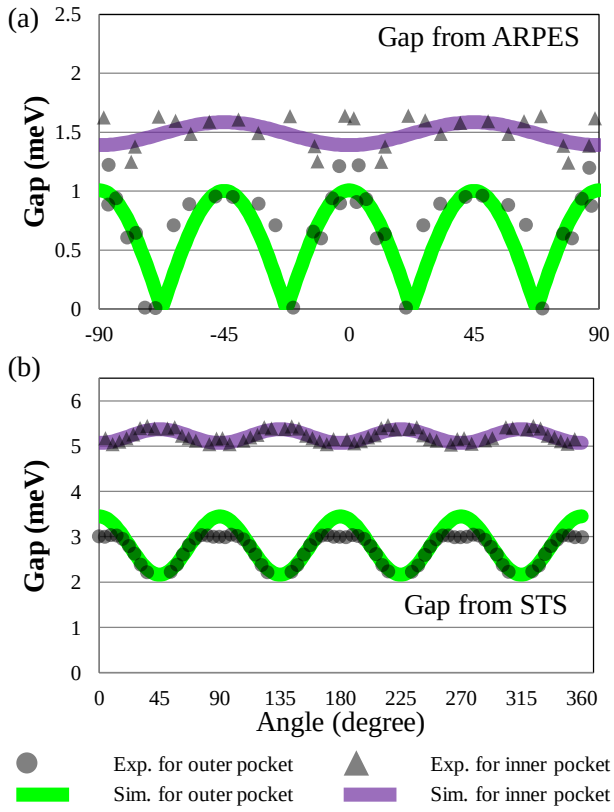

Figure 6.3: The digitalized gap structure of the compounds (a) $Ba_{0.12}K_{0.88}Fe_2As_2$ using ARPES [126] and (b) LiFeAs using STS [128]. The orbital-parity-selective gap modulation shown in purple and green curves is provided by our simulations according to Eq.(6.9). [3]

accompanied by nodes, but the anisotropy in the inner pockets (black triangle and mostly d_{xz}/d_{yz}) is rather weak. To our limited knowledge, the current explanation relies on the strong competition between various intra-pocket interactions [127]. However, the orbital-parity-selective gap anisotropy provides a more natural explanation. To explicitly demonstrate this scenario, we can also approximate the gap near the hole pockets:

$$\Delta_{o/e}(k) \approx \frac{k_F^4}{48}(-\tilde{\Delta}_{s\pm} \pm \frac{\tilde{\Delta}_{s_{++}}}{2})\cos 4\phi + (\tilde{\Delta}_{s\pm} \pm 2\tilde{\Delta}_{s_{++}} + \tilde{\Delta}_s), \tag{6.10}$$

where k_F is the Fermi wave vector. The plus (minus) in the amplitude of 4ϕ

[3] For ARPES, $(\Delta_{s_\pm}, \Delta_{s_{++}}, \Delta_s) = (-1.8, -0.5, 2.5)$ and $(-8, 6, -4.9)$ for inner and outer pockets. For STS, $(\Delta_{s_\pm}, \Delta_{s_{++}}, \Delta_s) = (-5, 4, 1.8)$ and $(-5, -4, -3.1)$ for inner and outer pockets. The unit is in meV. We present a physically meaningful set of numbers but are unable to fix the parameters in this over-determined problem.

modulation indeed shows the weaker (stronger) anisotropy in odd (eve) orbital parity. The large oscillation and small constant term for the even orbitals in Eq.(6.10) can easily induce the nodes of the outer pocket in Fig.6.3(a). If $\tilde{\Delta}_{s++} = 2\tilde{\Delta}_{s\pm}$, the 4ϕ angular modulation on odd parity will be totally quenched. Our results based on the simulations using Eq.(6.9) are tentatively provided in the green and purple curves in Fig. 6.3(a) and in reasonable agreement the experimental data.

The orbital-parity selective gap structure is also supported by the recent experiment using scanning tunneling spectroscopy (STS) in LiFeAs [128]. In Fig. 6.3(b), the experimental results show that the outer (black dots and mostly d_{xy}) and inner (black triangle and mostly d_{xz}/d_{yz}) hole pockets display out-of-phase angular modulation. Since these two pockets are close in momentum space, the scenario of only one pairing symmetry is definitely not consistent. However, if $\tilde{\Delta}_{s_{++}}$ becomes dominant in Eq.(6.10), the minus sign across two orbital parities can explain the out-of-phase 4ϕ oscillation. Again, our simulations shown in Fig. 6.3(b) result in fair agreement with the experimental data.

6.6 Finite-Momentum Pairing

In the inter-orbital parity channel, the glide symmetry in FeSC also dictates the existence of $\eta-$pairing with finite momentum Q [129]. Namely, $\langle a_{-k-Qe} a_{ko} \rangle = \langle c_{-\tilde{k},e} c_{\tilde{k},o} \rangle \propto \tilde{\Delta}(\tilde{k})\tilde{\Phi}(\tilde{k})$, where $\tilde{\Phi}(\tilde{k}) \equiv \tilde{\phi}_e(-\tilde{k})\tilde{\phi}_o(\tilde{k}) = -\tilde{\Phi}(-\tilde{k})$ and purely imaginary [122]. Hence, this pairing possesses spin singlet and breaks time reversal symmetry [130], and also has an odd parity form factor in both reciprocal and real spaces [130, 131]. A decisive difference between our finding and the previous proposals [131] is that the η-pairing in FeSC is fully forbidden in intra-orbital pairing and naturally coexists with all normal pairing channels without competition. Also, the stabilization of the η-pairing can choose neither to rely on the extremely strong antiferromagnetic correlation [130] nor the strong coupling picture [131]. The weights of η-pairing $|\tilde{\Phi}(\tilde{k})|$ are mostly relevant on the electron pockets because the strong $d_{xz}(d_{yz})$-d_{xy} hybridization. In Fig. 6.4, we show the weight of anomalous Green's function on electron pockets at X points in Fig. 6.1(c). In comparison with d_{yz} or d_{xy}

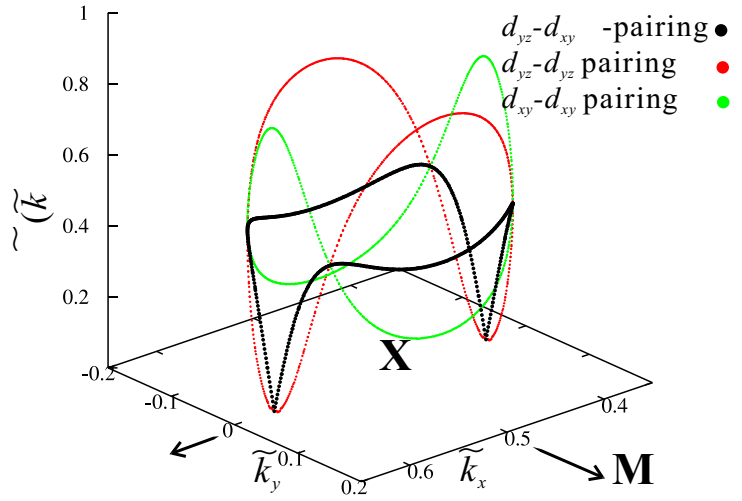

Figure 6.4: The weight of anomalous Green's function on the electron pockets in Fig. 6.1(c).

intra-orbital normal pairing, there exists a reasonable amount of $d_{yz} - d_{xy}$ η-pairing, and particularly maximal along XM direction. Further experiments in FeSC are needed to verify the Cooper pair breaking time-reversal symmetry as we predict.

6.7 Conclusion

In conclusion, the glide symmetry dictates that the orbital-parity physics is of prime importance for FeSC. The orbitals with different parities do not share the same quasi-particles nor superconducting pairing structures. Opposite parities have different sign structures of the superconducting order parameters involving two sublattices, such as s_{++} and $d_{x^2-y^2}$. The consequence uniquely leads to the orbital-parity-selective nodal structure and angular gap modulation. The latter is supported by the recent experiments using ARPES in $Ba_xK_{1-x}Fe_2As_2$ and STS in LiFeAs. There also exists an $\eta-$pairing involving two opposite orbital-parity quasiparticles. The $\eta-$pairing has its own peculiarity in *spatial oddness* as well as time reversal symmetry breaking, and thus needs the confirmation from future experiments.

Chapter 7

Conclusion

In this thesis, I study various physical consequences from the translational symmetry breaking on the electronic structure. We used the first-principles band structure and Wannier orbitals to obtain the one-particle spectral function in the normal cell BZ basis. This method is applied to various realistic materials.

In the first study, the Fermi surface topology of $cI16$ Li at high pressures is studied by unfolding method. We find the occurrence of a Lifshitz transition at $\sim$43 GPa, which explains the experimentally observed anomalous onset of the superconductivity enhancement toward lowered pressure. Furthermore we identify, in comparison with previous reports, additional nesting vectors that contribute to the $cI16$ structural stability. Our study highlights the importance of three-dimensional unfolding analyses for first-principles studies of Fermi surface topologies and instabilities in general.

In the second study, we provide an alternative understanding of the Dirac cone formation in graphene. This understanding is extended to a simple scenario to theoretically build Dirac cones in a general one-band 2D lattice.

In the third case, we investigate the physical effects of translational symmetry breaking in Fe-based high-temperature superconductors due to alternating anion positions. In the representative parent compounds, including the newly discovered Fe-vacancy-ordered $K_{0.8}Fe_{1.6}Se_2$, an unusual change of orbital character is found across the one-Fe Brillouin zone upon unfolding the first-principles band structure and Fermi surfaces, suggesting that covering a larger one-Fe Brillouin zone is necessary in experiments. Most significantly,

the electron pockets (critical to the magnetism and superconductivity) are found only created with the broken symmetry, advocating strongly its full inclusion in future studies, particularly on the debated nodal structures of the superconducting order parameter.

In the last study, we focus on the glide translation, which is the remaining symmetry after the translation is broken, in Fe-based superconductors. This glide symmetry leads to the orbital-parity selective quasiparticles. We show that the superconductivity consists of zero and finite momentum $(\pi, \pi, 0)$ Cooper pairs in intra- and inter-orbital-parity channels, respectively. The former develops the distinct gap structures for each orbital parity, and the latter is characteristic of spin singlet, spatial oddness and time reversal symmetry breaking. Such novel pairing structures explain the unusual gap angular modulation on the hole pockets in recent ARPES and STS experiments.

Bibliography

[1] B. Mansart, E. Papalazarou, M. F. Jensen, V. Brouet, L. Petaccia, L. de' Medici, G. Sangiovanni, F. Rullier-Albenque, A. Forget, D. Colson, et al., Phys. Rev. B **85**, 144508 (2012).

[2] L. Moreschini, P.-H. Lin, C.-H. Lin, W. Ku, V. Brouet, A. Bostwick, E. Rotenberg, and M. Grioni, Unpublished (2013).

[3] M. Tinkham, *Introduction to Superconductivity* (Mcgraw-Hil, New York, 1996).

[4] R. M. Hazen, *The Diamond Makers* (Cambridge University, 1999).

[5] C. Kittel, *Quantum Theory of Solids* (Wiley, 1987).

[6] N. W. Ashcroft and N. D. Mermin, *Solid State Physics* (Cengage Learning, 1976).

[7] F. Duan and J. Guojin, *Introduction to Condensed Matter Physics: Volume 1* (World Scientific Publishing Company, New York, 2005).

[8] G. Grüner, Rev. Mod. Phys. **60**, 1129 (1988).

[9] P. Anderson, P. Lee, and M. Saitoh, Solid State Communications **13**, 595 (1973).

[10] W. L. McMillan, Phys. Rev. B **12**, 1187 (1975).

[11] W. Kohn, Rev. Mod. Phys. **71**, 1253 (1999).

[12] K. Schwarz, P. Blaha, and G. K. H. Madsen, Computer Physics Communications **147**, 71 (2002).

[13] P. Hohenberg and W. Kohn, Phys. Rev. **136**, 864 (1964).

[14] E. Fermi, Atti Accad. Naz. Lincei, Cl. Sci. Fis. Mat. Nat. Rend. **6**, 602 (1927).

[15] L. H. Thomas, Proc. Cambridge Philos. Soc. **23**, 542 (1927).

[16] M. Levy, J. P. Perdew, and V. Sahni, Phys. Rev. A **30**, 2745 (1984).

[17] W. Kohn and L. J. Sham, Phys. Rev. **140**, 1133 (1965).

[18] C. Fiolhais, F. Nogueira, and M. M. (Eds.), *A Primer in Density Functional Theory* (Springer, Berlin, 2003).

[19] D. M. Ceperley and B. J. Alder, Phys. Rev. Lett. **45**, 566 (1980).

[20] R. O. Jones and O. Gunnarsson, Rev. Mod. Phys. **61**, 689 (1989).

[21] D. Singh and L. Nordström, *Planewaves, Pseudopotentials and the LAPW method* (Springer, New York, 2006), 2nd ed.

[22] G. H. Wannier, Phys. Rev. **52**, 191 (1937).

[23] N. Marzari, A. A. Mostofi, J. R. Yates, I. Souza, and D. Vanderbilt, Rev. Mod. Phys. **84**, 1419 (2012).

[24] A. L. Fetter and J. D. Walecka, *Quantum Theory of Many-Particle Systems* (Dover Publications, 2003).

[25] D. Andrea, Physica Scripta **2004**, 61 (2004).

[26] W. Ku, T. Berlijn, and C.-C. Lee, Phys. Rev. Lett. **104**, 216401 (2010).

[27] T. B. Chia-Hui Lin and W. Ku, arXiv:1311.4005 (2013).

[28] I. M. Lifshitz, Sov. Phys. JETP **11**, 1130 (1960).

[29] H. K. Onnes, Phys. Lab. Univ. Leiden **120**, 122 (1911).

[30] J. Tuoriniemi, K. Juntunen-Nurmilaukas, J. Uusvuori, E. Pentti, A. Salmela, and A. Sebedash, Nature **447**, 187 (2007).

[31] C. L. Guillaume, E. Gregoryanz, O. Degtyareva, M. I. McMahon, M. Hanfland, S. Evans, M. Guthrie, S. V. Sinogeikin, and H. K. Mao, Nat. Phys. **7**, 211 (2011).

[32] N. E. Christensen and D. L. Novikov, Phys. Rev. Lett. **86**, 1861 (2001).

[33] K. Iyakutti and C. N. Louis, Phys. Rev. B **70**, 132504 (2004).

[34] S. U. Maheswari, H. Nagara, K. Kusakabe, and N. Suzuki, Journal of the Physical Society of Japan **74**, 3227 (2005).

[35] D. Kasinathan, J. Kune, A. Lazicki, H. Rosner, C. S. Yoo, R. T. Scalettar, and W. E. Pickett, Phys. Rev. Lett. **96**, 047004 (2006).

[36] L. Shi and D. A. Papaconstantopoulos, Phys. Rev. B **73**, 184516 (2006).

[37] Y. Yao, J. S. Tse, K. Tanaka, F. Marsiglio, and Y. Ma, Phys. Rev. B **79**, 054524 (2009).

[38] T. Bazhirov, J. Noffsinger, and M. L. Cohen, Phys. Rev. B **82**, 184509 (2010).

[39] T. Bazhirov, J. Noffsinger, and M. L. Cohen, Phys. Rev. B **84**, 125122 (2011).

[40] G. Profeta, C. Franchini, N. N. Lathiotakis, A. Floris, A. Sanna, M. A. L. Marques, M. Lders, S. Massidda, E. K. U. Gross, and A. Continenza, Phys. Rev. Lett. **96**, 047003 (2006).

[41] R. Akashi and R. Arita, Phys. Rev. Lett. **111**, 057006 (2013).

[42] K. Shimizu, H. Ishikawa, D. Takao, T. Yagi, and K. Amaya, Nature **419**, 597 (2002).

[43] V. V. Struzhkin, M. I. Eremets, W. Gan, H.-k. Mao, and R. J. Hemley, Science **298**, 1213 (2002).

[44] S. Deemyad and J. S. Schilling, Phys. Rev. Lett. **91**, 167001 (2003).

[45] M. Hanfland, K. Syassen, N. E. Christensen, and D. L. Novikov, Nature **408**, 174 (2000).

[46] A. Rodriguez-Prieto, V. M. Silkin, and A. Bergara, Journal of the Physical Society of Japan **76SA**, 21 (2007).

[47] W. Ku, T. Berlijn, and C.-C. Lee, Phys. Rev. Lett. **104**, 216401 (2010).

[48] W. Ku, H. Rosner, W. E. Pickett, and R. T. Scalettar, Phys. Rev. Lett. **89**, 167204 (2002).

[49] C. W. Chu, T. F. Smith, and W. E. Gardner, Phys. Rev. B **1**, 214 (1970).

[50] V. I. Makarov and V. G. Baryakhtar, Sov. Phys. JETP **21**, 1151 (1965).

[51] M. Z. Hasan and C. L. Kane, Rev. Mod. Phys. **82**, 3045 (2010).

[52] M. R. Norman, J. Lin, and A. J. Millis, Phys. Rev. B **81**, 180513 (2010).

[53] M. Yi, D. H. Lu, J. G. Analytis, J. H. Chu, S. K. Mo, R. H. He, M. Hashimoto, R. G. Moore, I. I. Mazin, D. J. Singh, et al., Phys. Rev. B **80**, 174510 (2009).

[54] C.-H. Lin and W. Ku, arXiv:1303.4822 (2013).

[55] K. S. Novoselov, A. K. Geim, S. V. Morozov, D. Jiang, Y. Zhang, S. V. Dubonos, I. V. Grigorieva, and A. A. Firsov, Science **306**, 666 (2004).

[56] M. I. Katsnelson, K. S. Novoselov, and A. K. Geim, Nat. Phys. **2**, 620 (2006).

[57] K. S. Novoselov, Z. Jiang, Y. Zhang, S. V. Morozov, H. L. Stormer, U. Zeitler, J. C. Maan, G. S. Boebinger, P. Kim, and A. K. Geim, Science **315**, 1379 (2007).

[58] X. Du, I. Skachko, A. Barker, and E. Y. Andrei, Nat. Nano **3**, 491 (2008).

[59] A. F. Young and P. Kim, Nat. Phys. **5**, 222 (2009).

[60] N. M. Gabor, J. C. W. Song, Q. Ma, N. L. Nair, T. Taychatanapat, K. Watanabe, T. Taniguchi, L. S. Levitov, and P. Jarillo-Herrero, Science **334**, 648 (2011).

[61] K. S. Novoselov, A. K. Geim, S. V. Morozov, D. Jiang, M. I. Katsnelson, I. V. Grigorieva, S. V. Dubonos, and A. A. Firsov, Nature **438**, 197 (2005).

[62] Y. Zhang, Y.-W. Tan, H. L. Stormer, and P. Kim, Nature **438**, 201 (2005).

[63] K. I. Bolotin, F. Ghahari, M. D. Shulman, H. L. Stormer, and P. Kim, Nature **462**, 196 (2009).

[64] X. Du, I. Skachko, F. Duerr, A. Luican, and E. Y. Andrei, Nature **462**, 192 (2009).

[65] F. Guinea, M. I. Katsnelson, and A. K. Geim, Nat. Phys. **6**, 30 (2010).

[66] N. Levy, S. A. Burke, K. L. Meaker, M. Panlasigui, A. Zettl, F. Guinea, A. H. C. Neto, and M. F. Crommie, Science **329**, 544 (2010).

[67] C.-H. Park and S. G. Louie, Nano Letters **9**, 1793 (2009).

[68] K. Asano and C. Hotta, Phys. Rev. B **83**, 245125 (2011).

[69] A. Kobayashi, S. Katayama, Y. Suzumura, and H. Fukuyama, Journal of the Physical Society of Japan **76**, 034711 (2007).

[70] T. Mori, Journal of the Physical Society of Japan **79**, 014703 (2010).

[71] Y. Ran, F. Wang, H. Zhai, A. Vishwanath, and D.-H. Lee, Phys. Rev. B **79**, 014505 (2009).

[72] P. Richard, K. Nakayama, T. Sato, M. Neupane, Y. M. Xu, J. H. Bowen, G. F. Chen, J. L. Luo, N. L. Wang, X. Dai, et al., Phys. Rev. Lett. **104**, 137001 (2010).

[73] P. R. Wallace, Phys. Rev. **71**, 622 (1947).

[74] S. Y. Zhou, G. H. Gweon, J. Graf, A. V. Fedorov, C. D. Spataru, R. D. Diehl, Y. Kopelevich, D. H. Lee, S. G. Louie, and A. Lanzara, Nat. Phys. **2**, 595 (2006).

[75] A. Bostwick, T. Ohta, T. Seyller, K. Horn, and E. Rotenberg, Nat. Phys. **3**, 36 (2007).

[76] C. Hwang, C.-H. Park, D. A. Siegel, A. V. Fedorov, S. G. Louie, and A. Lanzara, Phys. Rev. B **84**, 125422 (2011).

[77] E. L. Shirley, L. J. Terminello, A. Santoni, and F. J. Himpsel, Phys. Rev. B **51**, 13614 (1995).

[78] C.-H. Lin, T. Berlijn, L. Wang, C.-C. Lee, W.-G. Yin, and W. Ku, Phys. Rev. Lett. **107**, 257001 (2011).

[79] C.-C. Lee, W.-G. Yin, and W. Ku, Phys. Rev. Lett. **103**, 267001 (2009).

[80] M. D. Lumsden, A. D. Christianson, E. A. Goremychkin, S. E. Nagler, H. A. Mook, M. B. Stone, D. L. Abernathy, T. Guidi, G. J. MacDougall, C. de la Cruz, et al., Nat. Phys. **6**, 182 (2010).

[81] Z. Xu, J. Wen, G. Xu, Q. Jie, Z. Lin, Q. Li, S. Chi, D. K. Singh, G. Gu, and J. M. Tranquada, Phys. Rev. B **82**, 104525 (2010).

[82] J. T. Park, D. S. Inosov, A. Yaresko, S. Graser, D. L. Sun, P. Bourges, Y. Sidis, Y. Li, J.-H. Kim, D. Haug, et al., Phys. Rev. B **82**, 134503 (2010).

[83] H.-F. Li, C. Broholm, D. Vaknin, R. M. Fernandes, D. L. Abernathy, M. B. Stone, D. K. Pratt, W. Tian, Y. Qiu, N. Ni, et al., Phys. Rev. B **82**, 140503 (2010).

[84] S. Graser, T. A. Maier, P. J. Hirschfeld, and D. J. Scalapino, New Journal of Physics **11**, 025016 (2009).

[85] K. Kuroki, H. Usui, S. Onari, R. Arita, and H. Aoki, Phys. Rev. B **79**, 224511 (2009).

[86] R. Thomale, C. Platt, W. Hanke, and B. A. Bernevig, Phys. Rev. Lett. **106**, 187003 (2011).

[87] A. V. Chubukov, D. V. Efremov, and I. Eremin, Phys. Rev. B **78**, 134512 (2008).

[88] R. T. Gordon, C. Martin, H. Kim, N. Ni, M. A. Tanatar, J. Schmalian, I. I. Mazin, S. L. Bud'ko, P. C. Canfield, and R. Prozorov, Phys. Rev. B **79**, 100506 (2009).

[89] Y. Nakai, T. Iye, S. Kitagawa, K. Ishida, S. Kasahara, T. Shibauchi, Y. Matsuda, and T. Terashima, Phys. Rev. B **81**, 020503 (2010).

[90] K. Hashimoto, M. Yamashita, S. Kasahara, Y. Senshu, N. Nakata, S. Tonegawa, K. Ikada, A. Serafin, A. Carrington, T. Terashima, et al., Phys. Rev. B **81**, 220501 (2010).

[91] H. Ding, P. Richard, K. Nakayama, K. Sugawara, T. Arakane, Y. Sekiba, A. Takayama, S. Souma, T. Sato, T. Takahashi, et al., Europhysics Letters **83**, 47001 (2008).

[92] K. Nakayama, T. Sato, P. Richard, T. Kawahara, Y. Sekiba, T. Qian, G. F. Chen, J. L. Luo, N. L. Wang, H. Ding, et al., Phys. Rev. Lett. **105**, 197001 (2010).

[93] C. de la Cruz, Q. Huang, J. W. Lynn, J. Li, W. R. Ii, J. L. Zarestky, H. A. Mook, G. F. Chen, J. L. Luo, N. L. Wang, et al., Nature **453**, 899 (2008).

[94] M. Rotter, M. Tegel, D. Johrendt, I. Schellenberg, W. Hermes, and R. Pttgen, Phys. Rev. B **78**, 020503 (2008).

[95] X. C. Wang, Q. Q. Liu, Y. X. Lv, W. B. Gao, L. X. Yang, R. C. Yu, F. Y. Li, and C. Q. Jin, Solid State Communications **148**, 538 (2008).

[96] A. Subedi, L. Zhang, D. J. Singh, and M. H. Du, Phys. Rev. B **78**, 134514 (2008).

[97] P. Zavalij, W. Bao, X. F. Wang, J. J. Ying, X. H. Chen, D. M. Wang, J. B. He, X. Q. Wang, G. F. Chen, P. Y. Hsieh, et al., Phys. Rev. B **83**, 132509 (2011).

[98] O. Andersen and L. Boeri, Annalen der Physik **523**, 8 (2011).

[99] A. Mans, I. Santoso, Y. Huang, W. K. Siu, S. Tavaddod, V. Arpiainen, M. Lindroos, H. Berger, V. N. Strocov, M. Shi, et al., Phys. Rev. Lett. **96**, 107007 (2006).

[100] H. Ding (private communication).

[101] I. I. Mazin, D. J. Singh, M. D. Johannes, and M. H. Du, Phys. Rev. Lett. **101**, 057003 (2008).

[102] V. Cvetkovic and Z. Tesanovic, Europhysics Letters **85**, 37002 (2009).

[103] P. Zavalij, W. Bao, X. F. Wang, J. J. Ying, X. H. Chen, D. M. Wang, J. B. He, X. Q. Wang, G. F. Chen, P.-Y. Hsieh, et al., Phys. Rev. B **83**, 132509 (2011).

[104] C. Cao and J. Dai, Phys. Rev. Lett. **107**, 056401 (2011).

[105] Y. Zhang, L. X. Yang, M. Xu, Z. R. Ye, F. Chen, C. He, H. C. Xu, J. Jiang, B. P. Xie, J. J. Ying, et al., Nat. Mater. **10**, 273 (2011).

[106] Z. Wang, Y. J. Song, H. L. Shi, Z. W. Wang, Z. Chen, H. F. Tian, G. F. Chen, J. G. Guo, H. X. Yang, and J. Q. Li, Phys. Rev. B **83**, 140505 (2011).

[107] F. Han, H. Yang, B. Shen, Z.-Y. Wang, C.-H. Li, and H.-H. Wen, Philosophical Magazine **92**, 2553 (2012).

[108] G. R. Stewart, Rev. Mod. Phys. **83**, 1589 (2011).

[109] K. Kuroki, H. Usui, S. Onari, R. Arita, and H. Aoki, Phys. Rev. B **79**, 224511 (2009).

[110] S. Onari and H. Kontani, Phys. Rev. Lett. **109**, 137001 (2012).

[111] P. J. Hirschfeld, M. M. Korshunov, and I. I. Mazin, Reports on Progress in Physics **74**, 124508 (2011).

[112] C. Fang, Y.-L. Wu, R. Thomale, B. A. Bernevig, and J. Hu, Phys. Rev. X **1**, 011009 (2011).

[113] S. Onari and H. Kontani, Phys. Rev. Lett. **103**, 177001 (2009).

[114] T. A. Maier, S. Graser, P. J. Hirschfeld, and D. J. Scalapino, Phys. Rev. B **83**, 100515 (2011).

[115] H. Ding, P. Richard, K. Nakayama, K. Sugawara, T. Arakane, Y. Sekiba, A. Takayama, S. Souma, T. Sato, T. Takahashi, et al., Europhysics Letters **83**, 47001 (2008).

[116] L. Zhao, H.-Y. Liu, W.-T. Zhang, J.-Q. Meng, X.-W. Jia, G.-D. Liu, X.-L. Dong, G.-F. Chen, J.-L. Luo, N.-L. Wang, et al., Chinese Physics Letters **25**, 4402 (2008).

[117] Z. H. Liu, P. Richard, K. Nakayama, G. F. Chen, S. Dong, J. B. He, D. M. Wang, T. L. Xia, K. Umezawa, T. Kawahara, et al., Phys. Rev. B **84**, 064519 (2011).

[118] S. V. Borisenko, V. B. Zabolotnyy, D. V. Evtushinsky, T. K. Kim, I. V. Morozov, A. N. Yaresko, A. A. Kordyuk, G. Behr, A. Vasiliev, R. Follath, et al., Phys. Rev. Lett. **105**, 067002 (2010).

[119] T. Kondo, A. F. Santander-Syro, O. Copie, C. Liu, M. E. Tillman, E. D. Mun, J. Schmalian, S. L. Budko, M. A. Tanatar, P. C. Canfield, et al., Phys. Rev. Lett. **101**, 147003 (2008).

[120] J. D. Fletcher, A. Serafin, L. Malone, J. G. Analytis, J. H. Chu, A. S. Erickson, I. R. Fisher, and A. Carrington, Phys. Rev. Lett. **102**, 147001 (2009).

[121] J. Dong-Jin, A. B. Vorontsov, I. Vekhter, K. Gofryk, Z. Yang, S. Ju, J. B. Hong, J. H. Han, Y. S. Kwon, F. Ronning, et al., New Journal of Physics **13**, 023036 (2011).

[122] P. A. Lee and X.-G. Wen, Phys. Rev. B **78**, 144517 (2008).

[123] W. Lv and P. Phillips, Phys. Rev. B **84**, 174512 (2011).

[124] M. Casula and S. Sorella, Phys. Rev. B **88**, 155125 (2013).

[125] T. Shimojima, F. Sakaguchi, K. Ishizaka, Y. Ishida, T. Kiss, M. Okawa, T. Togashi, C.-T. Chen, S. Watanabe, M. Arita, et al., Science **332**, 564 (2011).

[126] Y. Ota, K. Okazaki, Y. Kotani, T. Shimojima, W. Malaeb, S. Watanabe, C.-T. Chen, K. Kihou, C. H. Lee, A. Iyo, et al. (2013).

[127] S. Maiti, M. M. Korshunov, and A. V. Chubukov, Phys. Rev. B **85**, 014511 (2012).

[128] M. P. Allan, A. W. Rost, A. P. Mackenzie, Y. Xie, J. C. Davis, K. Kihou, C. H. Lee, A. Iyo, H. Eisaki, and T.-M. Chuang, Science **336**, 563 (2012).

[129] C. N. Yang, Phys. Rev. Lett. **63**, 2144 (1989).

[130] R. T. Scalettar, R. R. P. Singh, and S. Zhang, Phys. Rev. Lett. **67**, 370 (1991).

[131] J. Hu and N. Hao, Phys. Rev. X **2**, 021009 (2012).

Appendix A

Mathematical Formalism of Dirac Cone Generation

In this appendix, I provide more detailed derivation about the Dirac cone formation in Chapter 4. First we need to design a supercell with size M ($M \geq 3$) times larger than the original unit cell. In momentum space of the reference system with smaller unit cells, M k points connected by supercell reciprocal lattice vectors are coupled. Second, the on-site energy variation leads to a uniform potential in this momentum space. In this subspace, Hamiltonian to describe the M coupled k points is

$$H_{sub} = \begin{pmatrix} E_1 & 0 & \cdots & 0 \\ 0 & E_2 & \cdots & 0 \\ \vdots & \vdots & \ddots & \vdots \\ 0 & 0 & \cdots & E_M \end{pmatrix}_{M\times M} + \frac{\varepsilon}{M} \begin{pmatrix} 1 & 1 & \cdots & 1 \\ 1 & 1 & \cdots & 1 \\ \vdots & \vdots & \ddots & \vdots \\ 1 & 1 & \cdots & 1 \end{pmatrix}_{M\times M} , \qquad \text{(A.1)}$$

where E_i refers to the eigenenergy in the original dispersion. Third, geometrically, in a CDW-free two-dimensional dispersion, it is always true that at least three coupled k points can be found degenerate in somewhere of the dispersion. Thus, we assume there is $N-$fold degeneracy ($M \geq N \geq 3$) out of the

M coupled k's. The Hamiltonian can be reduced to

$$H_{sub} = \left(\begin{array}{cccc|c} e_1 & 0 & \cdots & 0 & \\ 0 & e_2 & \cdots & 0 & 0 \\ \vdots & \vdots & \ddots & \vdots & \\ 0 & 0 & \cdots & e_L & \\ \hline & & & & \\ & & 0 & & 0 \\ & & & & \end{array}\right)_{M\times M} + \frac{\varepsilon}{M}\Omega_{M\times M} \qquad \text{(A.2)}$$

subject to a trivial overall constant. We denote the matrix of ones by Ω. $L = M - N$ and e_i denotes the energy deviation from the $N-$fold degenerate energy for the non-degenerate k_i.

I will introduce two basic theorems and proceed to claim the resulting linear dispersion of Eq. A.2.

Theorem 4 *The eigenvalues of an M-by-M matrix of ones $\Omega_{M\times M}$,*

$$\begin{pmatrix} 1 & 1 & \cdots & 1 \\ 1 & 1 & \cdots & 1 \\ \vdots & \vdots & \ddots & \vdots \\ 1 & 1 & \cdots & 1 \end{pmatrix}_{M\times M},$$

contain one M and $(M-1)$ zeroes.

Simple case example: Consider a 4-by-4 matrix of ones, the eigenvalue equation requires eigenvalues λ to satisfy

$$\begin{vmatrix} 1-\lambda & 1 & 1 & 1 \\ 1 & 1-\lambda & 1 & 1 \\ 1 & 1 & 1-\lambda & 1 \\ 1 & 1 & 1 & 1-\lambda \end{vmatrix} = 0.$$

We can perform the row operations to subtract the first row from any other

rows to obtain

$$\begin{vmatrix} 1-\lambda & 1 & 1 & 1 \\ \lambda & -\lambda & 0 & 0 \\ \lambda & 0 & -\lambda & 0 \\ \lambda & 0 & 0 & -\lambda \end{vmatrix} = 0.$$

Then, we follow the column operations to add the second, third and fourth columns to the first.

$$\begin{vmatrix} 4-\lambda & 1 & 1 & 1 \\ 0 & -\lambda & 0 & 0 \\ 0 & 0 & -\lambda & 0 \\ 0 & 0 & 0 & -\lambda \end{vmatrix} = 0.$$

In the cofactor expansion along the first row, only the first term is non-zero so the resulting equation is

$$(4-\lambda)(-\lambda)^3 = 0.$$

Therefore, the eigenvalues are $\{4, 0, 0, 0\}$.

Proof: *We need to solve eigenvalue λ from this equation.*

$$\begin{vmatrix} 1-\lambda & 1 & \cdots & 1 \\ 1 & 1-\lambda & \cdots & 1 \\ \vdots & \vdots & \ddots & \vdots \\ 1 & 1 & \cdots & 1-\lambda \end{vmatrix}_{M\times M} = 0.$$

Perform the row operations to subtract the first row from any other rows.

$$\begin{vmatrix} 1-\lambda & 1 & \cdots & 0 \\ \lambda & -\lambda & \cdots & 0 \\ \vdots & \vdots & \ddots & \vdots \\ \lambda & 0 & \cdots & -\lambda \end{vmatrix}_{M\times M} = 0.$$

Perform the column operations to add any columns except the first to the first

column.

$$\begin{vmatrix} N-\lambda & 1 & \cdots & 1 \\ 0 & -\lambda & \cdots & 0 \\ \vdots & \vdots & \ddots & \vdots \\ 0 & 0 & \cdots & -\lambda \end{vmatrix}_{M\times M} = 0.$$

After the cofactor expansion along the first row, we have

$$(N-\lambda)(-\lambda)^{N-1} = 0.$$

The eigenvalues are solved as one N and $(N-1)$ zeroes.

Theorem 5 *Consider an M by M matrix as follows*

$$\left(\begin{array}{cccc|c} 1+e_1 & 1 & \cdots & 1 & \\ 1 & 1+e_2 & \cdots & 1 & \Omega_{L\times N} \\ \vdots & \vdots & \ddots & \vdots & \\ 1 & 1 & \cdots & 1+e_L & \\ \hline & & & & \\ & \Omega_{N\times L} & & & \Omega_{N\times N} \\ & & & & \end{array}\right)_{M\times M},$$

where $L = M - N$. Its eigenvalues contain $(N-1)$ zeroes.

Proof: *The secular equation becomes*

$$\left|\begin{array}{cccc|c} 1+e_1-\lambda & 1 & \cdots & 1 & \\ 1 & 1+e_2-\lambda & \cdots & 1 & \Omega_{L\times N} \\ \vdots & \vdots & \ddots & \vdots & \\ 1 & 1 & \cdots & 1+e_L-\lambda & \\ \hline & & & & \\ & \Omega_{N\times L} & & & \Omega_{N\times N}-\lambda \\ & & & & \end{array}\right|_{M\times M} = 0.$$

We follow a similar procedure with the proof in the previous theorem. First, we can perform the row operations to subtract the $(L+1)$-th row from any rows

below it. Then, we add $(L+2)$*-th to* M*-th columns to* $(L+1)$*-th column.*

$$
\left|\begin{array}{cccc|c|ccc}
1+e_1-\lambda & 1 & \cdots & 1 & N & & & \\
1 & 1+e_2-\lambda & \cdots & 1 & N & & \Omega_{L\times(N-1)} & \\
\vdots & \vdots & \ddots & \vdots & \vdots & & & \\
1 & 1 & \cdots & 1+e_L-\lambda & N & & & \\
\hline
1 & 1 & \cdots & 1 & N-\lambda & 1 & \cdots & 1 \\
\hline
 & & & & 0 & & & \\
 & & 0 & & \vdots & & -\lambda & \\
 & & & & 0 & & &
\end{array}\right|_{M\times M} = 0
$$

By cofactor expansions from the lower right corner, we can extract an equation $\lambda^{N-1}=0$*. Therefore, eigenvalues must contain* $(N-1)$ *zeroes.*

Applying Theorem 5 to Eq. A.2, there are $(N-1)$-fold remaining degenerate without any energy renormalization. They form an $(N-1)$-dimensional subspace on their own. This remains correct regardless of the strength of symmetry breaking potential so they become the candidates for Dirac points in a new dispersion. Any k points surrounding them are subject to CDW effects and have modified eigenenergy. If we consider an infinitesimal momentum deviation $(\delta k_x, \delta k_y)$, the degeneracy is slightly broken. We can estimate the energy deviation as $\delta E_i = \nabla_k E \cdot \delta k$. There exists new terms of δE_i added to the diagonal elements of the Hamiltonian in Eq. A.2. If we perform first-order energy perturbation, the resulting energy correction must be proportion to $\nabla_k E \cdot \delta k$. Thus, in a infinitesimal momentum deviation region, electronic structure linearly disperses from those Dirac points and finalizes a conical shape.

Appendix B

Comparison between Theoretical and Experimental ARPES Spectral Functions

In this appendix, I will present two collaborative projects that I participated in between 2012 to 2013, and that demonstrate good comparison with the spectral function features we present in Chapter 5. Since this part involves some explanation of the ARPES experimental details, I decide to collect them together in this appendix as the experimental support to our simulation.

In Chapter 5, we present the unfolded one-particle spectral function carrying the momentum-resolved density of states of the electrons. In principle, the measured intensity

$$I(k = K, \omega) \propto \sum_n |A \cdot \langle \phi_f^k | p | kn \rangle|^2 f(\omega) A_n(k, \omega), \tag{B.1}$$

there is the dipole matrix element $\langle \phi_f^k | p | kn \rangle$ involved. Usually, $|\phi_f^k\rangle$, the final state of the photoelectron, is approximated as a plane wave. As the experimentalists select the particular linear photon polarization, A is aligned in the certain direction. Hence, one specific $|kn\rangle$, which gives rises to the largest dipole moment, would lead to the dominant signal. In other words, ARPES can have orbital selectivity by tuning the polarizing to favor particular Wannier function $|kn\rangle$, which can develop a large value of $\langle \phi_f^k | p | kn \rangle$.

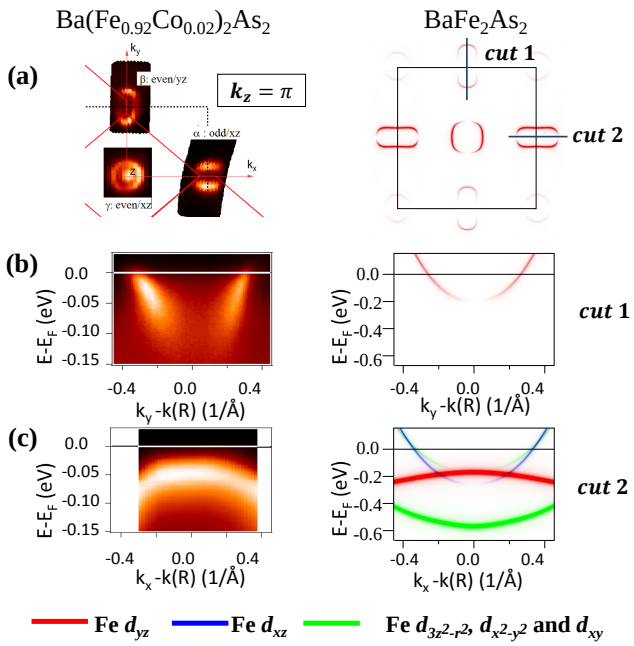

Figure B.1: $Ba(Fe_{0.92}Co_{0.02})_2As_2$ ARPES versus first-principles $BaFe_2As_2$ spectral function. (a) Fermi surface measured in ARPES with polarization along k_y in the left panel and the corresponding first-principles spectral function in the right. The comparison on the dispersion along the two marked cuts in (a, left) are given in (b) and (c)

B.1 $Ba(Fe_{0.92}Co_{0.02})_2As_2$

In the collaborative study of $Ba(Fe_{0.92}Co_{0.02})_2As_2$ in Ref. [1], the setup uses the photon with polarization along k_y. Thus, the dominant dipole matrix element would naturally come from d_{yz} orbital. As shown in Fig. B.1, we keep the experimental intensity on the left and put our simulated spectral function with the orbital characters on the right for direct comparison. First in (a), ARPES Fermi surface has the stronger intensity around $(\pi, 0, \pi)$ but the diminished one around $(0, \pi, \pi)$. This is perfectly reproduced in its right panel. In (b) of cut 1, the weight is weakened toward the band bottom and also matched well in the simulation of the right panel. In (c) of cut 2, we again reproduce the dispersion with correct shape and relative strength in the red d_{yz}. Thus, except a band width renormalization factor, our simulation reaches s good agreement with his experiment.

B.2 $Fe_{1.03}Te_{0.74}Se_{0.26}$

In the other study of $Fe_{1.03}Te_{0.74}As_{0.26}$ in Ref. [2], this is the first measurement, which can probe the wide range of momentum space beyond the first Brillouin zone with persistent quality resolution. There are two main features in Fig. B.2 (indicated by the red arrows) we will focus on: the elongated ellipse around Γ and the four-fold petal shape around M $(\pi, \pi, 0)$. From the comparison with Fig. B.2(a,right) of our simulation, we know the polarization setup seems to promote d_{xz} around Γ and $d_{3z^2-r^2}$ around M points. Around Γ, the selected s polarization has electric field oscillation lying in the x-z scattering plane so this favors d_{xz} by its large dipole moment. About the four-fold petal shape around M, its $d_{3z^2-r^2}$ character is confirmed by the identical signal after rotating the sample by 45°. This unchanged intensity rules out d_{xz} and d_{yz} first. Also, the $d_{x^2-y^2}$ and d_{xy} is usually suppressed due to the small tilting angle in ARPES experiment. Besides, in Fig. B.2(b) and (c), the $d_{3z^2-r^2}$ spectral weight along $\Gamma M \Gamma$ and XMX is well matched by our simulation.

In Fig. B.3, we explore the different energy slice on the M pockets. The evolution of the four-fold petal on the Fermi energy to the *spoke* shape at the -50 meV is well reproduced by our simulation in the low panel. Thus, except the band width renormalization, our unfolded spectral functions readily serve an unbiased tool to explain the orbital dependent ARPES weight. Most importantly, this agreement leads to the confirmation that the M $d_{3z^2-r^2}$ weight is folded from Γ d_{xz} pocket. Therefore, it experimentally verifies the our statement of orbital-parity switching band folding discussed in Chapter 5.

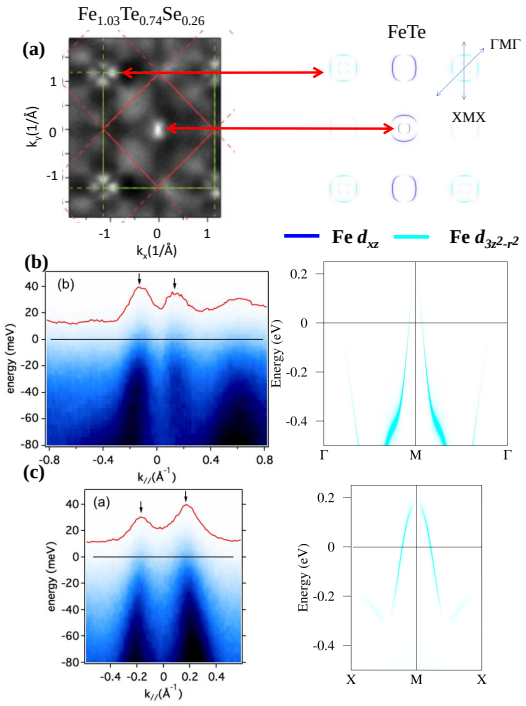

Figure B.2: $Fe_{1.03}Te_{0.74}As_{0.26}$ ARPES versus first-principles FeTe spectral function. (a) Fermi surface measured in ARPES with p polarization in the left panel and the corresponding first-principles spectral function in the right. The comparison on the dispersion along the two marked cuts in (a, left) are given in (b) and (c)

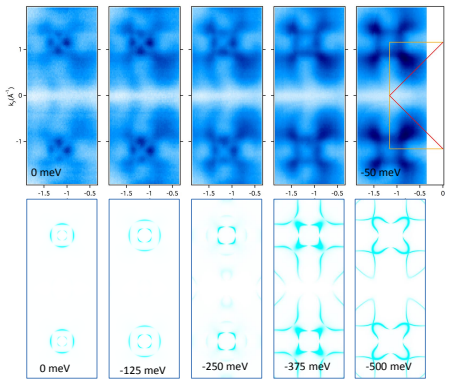

Figure B.3: $Fe_{1.03}Te_{0.74}As_{0.26}$ ARPES (upper row) versus first-principles FeTe (lower row) spectral function on the M pockets at different energies.

Appendix C

Virtual Crystal Approximation

In this appendix, we will discussion the virtual crystal approximation used in Chapter 5 in more details. In the presence symmetry breaking potential, a translationally symmetric Hamiltonian can be constructed via the virtual crystal approximation (VCA):

$$H^{VCA}_{r,n;0,n\prime} = \sum_{r\prime} H_{r\prime+r,n;r\prime,n\prime} / \sum_{r\prime} 1, \tag{C.1}$$

where $H_{r\prime+r,n;r\prime,n\prime}$ and $H^{VCA}_{r,n;0,n\prime}$ are Hamiltonians with broken translational symmetry in the basis of Wannier orbitals n located at normal cell index r. The summation of $r\prime$ is over inequivalent normal cell lattice vectors in a single supercell (namely the positions of two or more inequivalent Fe sites). Thus, the symmetry breaking terms of the original Hamiltonian would be averaged out, but the symmetry respecting terms would be kept.

In the Fe-based superconductors, one can choose whether to integrate the As p orbitals into Fe d Wannier orbitals or not, during the construction of the Wannier orbitals. If As p orbitals are integrated out, we will effectively obtain the five-band VCA Hamiltonian from Eq. C.1. If not, the eight-band VCA Hamiltonian (5 Fe d and 3 As p) will be obtained. Fig. 3 in the latter shows clearly that VCA has a larger impacts in the 8-band case. This is easily understood from the following consideration. In the 8-band case, the symmetry breaking terms are mostly those hopping terms involving Fe d and As p orbitals, since As p orbitals are located in different locations. Upon integrating out these terms, they effectively renormalize the remaining hopping terms

between Fe d orbitals, both the symmetry breaking and symmetry respecting ones. By throwing out the symmetry breaking terms at the eight-band level via VCA, one also removes the renormalization to the symmetry respecting hopping between Fe d orbitals as well. In either case, however, the qualitative effect of losing the electron pockets persists, since it is mostly dictated by the symmetry property of the system and is thus more robust against detailed changes of the Hamiltonian.

Appendix D

List of Acronyms

ARPES	Angle resolved photoemission spectroscopy
BCS	Bardeen-Cooper-Schrieffer
BZ	Brillouin zone
CDW	Charge density wave
DC	Dirac cone
DFT	Density functional theory
DOS	Density of states
EBS	Electronic band structure
FeSC	Fe-based superconductor
FS	Fermi surface
KS	Kohn-Sham
LAPW	Linearized augmented plane wave
LDA	Local density approximation
LT	Lifshitz transition
TSBP	Translational symmetry breaking potential
VCA	Virtual crystal approximation